ON-CHIP SEPARATION AND DETECTION OF BIOLOGICAL PARTICLES USING DIELECTROPHORESIS AND RESISTIVE PULSE SENSING

By

YUEJUN KANG

Dissertation

Submitted to the Faculty of the

Graduate School of Vanderbilt University

in partial fulfillment of the requirements for

the degree of

DOCTOR OF PHILOSOPHY

in

Mechanical Engineering

December, 2008

Nashville, Tennessee

Approved:

Professor Dongqing Li

Professor Deyu Li

Professor Robert W. Pitz

Professor Taylor G. Wang

Professor John P. Wikswo

To Rikkie and Ranran

for endless love beyond the years

ACKNOWLEDGMENTS

1pm Nov. 07, 2008, I was walking to Mrs. Liz Leis's office in Kirkland Hall to ask her to check my dissertation format. As I was stepping on the carpet of mixed maple and oak leaves, and watching the campus turning into fire and gold in the sunshine of late autumn after a light shower in the early morning, I suddenly noticed that it is the time. The road to become a member of engineering faculty is long and hard. After another four years since my last graduate degree, I am really close at this time. The big picture is much clearer in front of me. Everything happened in this campus and this city, both highs and lows, makes my life in here memorable forever.

I would like to thank my advisor, Dr. Dongqing Li, for his vision and the comprehensive academic training offered to me. His diligent and hard-working life style is so contagious that I cannot be shielded by my immune system. I would also thank Dr. Deyu Li for his stimulating and thought provoking conversations. The completion of this work is also owed to my colleagues and friends, Dr. Kwan Hyoung Kang, Dr. Xiangchun Xuan, Dr. Guoqing Hu, Dr. Yao-Nan Wang, Dr. Xudong Wu, Mr. Barbaros Cetin, Mr. Zhemin Wu, Dr. Dongyan Xu, Ms. Jiashu Sun, Dr. Manoj Sridhar, and our collaborators, Dr. Josiane E. Eid, Dr. Spyros A. Kalams, Dr. Jie Wei, Dr. Scott van Compernolle, and Mrs. Louise Barnett. I have learned a lot from these excellent people and enjoyed the pleasure of collaborative team-work.

My sincere gratitude should also be extended to the other professors in my committee, Dr. Robert W. Pitz, Dr. Taylor G. Wang, Dr. John P. Wikswo for their precious time examining my dissertation. My former advisors from Singapore, Dr.

Charles Chun Yang and Dr. Xiaoyang Huang, keep providing the never-ending support on my career building. The superior administrative and managerial services by Ms. Suzanne Weiss and Mrs. Myrtle Daniels have made my graduate life much easier and happier.

Finally I want to thank the financial support from the school of engineering and H. Fort Flowers foundation through a research assistantship, without which I would not have a chance to work with so many wonderful people.

VITA

Yuejun Kang was born on March 24, 1977 in Xiangfan, Hubei, People's Republic of China. He obtained Bachelor of Engineering degree in July 2000 from University of Science and Technology of China, Hefei, Anhui, China. From June 2000 to May 2001, he worked as a Product Specialist in Acer Communication & Multimedia Co. Ltd., Suzhou, China. From June 2001 to June 2004, he was a graduate student in Nanyang Technological University in Singapore, from where he earned a PhD degree in Mechanical and Aerospace Engineering. In August 2004 he joined University of Toronto as a PhD student and transferred to Vanderbilt University in September 2005. He has been working as a graduate research assistant since then.

LIST OF PUBLICATIONS IN REFEREED JOURNALS

1. Kang Y, Li D. "Electrokinetic Motion of Particles and Cells in Microchannels" *Microfluid. Nanofluid.* (in preparation, finalizing)
2. Cetin B, Kang Y, Wu Z, Li D. "Continuous Particle Separation By Size via AC-Dielectrophoresis Using a Lab-on-a-chip Device with 3D Electrodes" *Electrophoresis* (Accepted, 2008)
3. Kang Y, Cetin B, Wu Z, Li D. "Continuous Particle Separation with Localized AC-Dielectrophoresis Using Embedded Electrodes and an Insulating Hurdle" *Electrochimica Acta* (in press, 2008)
4. Sun J, Vajandar SK, Xu D, Kang Y, Hu G, Li DQ, Li DY. "Experimental Characterization of Electrical Current Leakage in PDMS Microfluidic Devices" *Microfluid. Nanofluid.* (in press, 2008)
5. Wu X, Chon CH, Wang YN, Kang Y, Li D. "Simultaneous Particle Counting and Detecting on a Chip" *Lab Chip* 8: 1943-1949 (2008)

6. Kang Y, Wu X, Wang YN, Li D. "On-chip Fluorescence-Activated Particle Counting and Sorting System" *Anal. Chim. Acta* 626: 97-103 (2008)
7. Wu X, Kang Y, Wang YN, Xu D, Li DY, Li DQ. "Microfluidic Differential Resistive Pulse Sensors" *Electrophoresis* 29: 2754-2759 (2008)
8. Sridhar M, Xu D, Kang Y, Hmelo AB, Feldman LC, Li DQ, Li DY. "Experimental Characterization of a Metal-oxide-semiconductor Field-effect Transistor-based Coulter Counter" *J. Appl. Phys.* 103: 104701 (2008)
9. Wang YN, Kang Y, Xu D, Chon CH, Barnett L, Kalams SA, Li DY, Li DQ. "On-Chip Counting the Number and the Percentage of CD4+ T Lymphocytes" *Lab Chip* 8: 309-315 (2008)
10. Kang Y, Li D, Kalams SA, Eid JE. "DC-Dielectrophoretic Separation of Biological Cells by Size" *Biomed. Microdevices* 10: 243-249 (2008)
11. Xu D, Kang Y, Sridhar M, Hmelo AB, Feldman LC, Li DQ, Li DY. "Wide-Spectrum, Ultrasensitive Fluidic Sensors with Amplifications from both Fluidic Circuits and MOSFETs" *Appl. Phys. Lett* 91: 013901 (2007)
12. Kang Y, Tan SC, Yang C, Huang X. "Electrokinetic Pumping Using Packed Microcapillary" *Sensor. Actuat A-Phys.* 133: 375-382 (2007)
13. Kang KH, Kang Y, Xuan X, Li D. "Continuous Separation of Microparticles by Size with DC-dielectrophoresis" *Electrophoresis* 27: 694-702 (2006)
14. Kang KH, Xuan X, Kang Y, Li D. "Effects of DC-dielectrophoretic force on particle trajectories in microchannels" *J. Appl. Phys* 99: 064702 (2006)
15. Kang Y, Yang C, Huang X. "Joule Heating Effects of Electroosmotic Flow in Microcapillaries Packed with Microspheres" *Langmuir* 21: 7598-7607 (2005)
16. Kang Y, Yang C, Huang X. "Analysis of Electroosmotic Flow in a Microchannel Packed with Microspheres" *Microfluid. Nanofluid*. 1: 168-176 (2005)
17. Marcos, Kang Y, Ooi KT, Yang C, Wong TN. "Frequency Dependent Velocity and Vorticity Fields of Electroosmotic Flow in a Closed-End Cylindrical Microchannel" *J. Micromech. Microeng.* 15: 301-312 (2005)
18. Kang Y, Yang C, Huang X. "Analysis of Electroosmotic Flow in a Microcapillary Packed with Microspheres" *Int. J. Eng. Sci.* 42: 2011-2027 (2004)
19. Kang Y, Yang C, Huang X. "AC Electroosmosis in Microchannels Packed with a Porous Medium" *J. Micromech. Microeng.* 14: 1249-1257 (2004)
20. Kang Y, Yang C, Huang X. "Modeling of the Capillary Electrochromatography with Application in BioMEMS" *Int. J. Comput. Eng. Sci.* 4: 261-264 (2003)
21. Kang Y, Yang C, Huang X. "Dynamic aspects of electroosmotic flow in a cylindrical microcapillary" *Int. J. Eng. Sci.*, 40: 2203-2221 (2002)
22. Kang Y, Yang C, Huang X. "Electroosmotic Flow in a Capillary Annulus with High Zeta Potentials" *J. Colloid Interface Sci.* 253: 285-294 (2002)

ABSTRACT

Since the biological reagents and particles exist in a fluidic natural environment, microfluidics-based lab-on-a-chip devices render excellent platforms for relevant biomedical manipulations and assays. This emerging field is actively approached by scientists from various disciplines and exploited for a wide range of applications. The lab-on-a-chip systems have competitive advantages over the conventional biomedical instruments because of their portability, minute sample consumption, and slashed manufacturing and operational costs. This dissertation presents an original investigation on microfluidics technology and development of lab-on-a-chip microdevices for critical on-chip manipulations of biological particles, such as separation and detection.

The separation is achieved by field-flow-fractionation employing the non-linear electrokinetic phenomenon, dielectrophoresis (DEP). DEP arises from the interaction of a dielectric particle, such as a cell, and a highly non-uniform electric field which can be generated under an electric field by obstruction or hurdles made of electrically insulating materials. The DEP force acting on a particle is proportional to the particle's volume. Thus the moving particles deviate from the streamlines and the degree of deviation is dependent on the particle size. Finally the particles of different sizes are inducted into different collection wells according to their different degrees of deviation.

The detection is achieved by Coulter-type resistive pulse sensing (RPS) scheme, in which the translocation of a non-conducting particle through an electrolyte-filled small aperture leads to an increase in the resistance of the aperture. The frequency and amplitude of the resulting trans-aperture voltage modulations provide critical information about the number and size of the particles of interest. For cell detection and enumeration,

the developed system integrates optical fluorescence detection with RPS enhanced by a metal oxide semiconductor field effect transistor (MOSFET). Further to improve the sensitivity, symmetric mirror channels are designed with multiple-stage differential amplifications, which significantly reduces the noise and achieves better signal-to-noise ratio. A record low volume ratio of the particle to the micron-sized sensing aperture has been recorded, which is about ten times lower than the lowest volume ratio reported in the literature.

TABLE OF CONTENTS

Page

LIST OF FIGURES

LIST OF TABLES

CHAPTER I

INTRODUCTION

Background and Motivation

The cell is the most basic functional element in living organisms. Cells contain important information for genetic development, metabolism, immunological responses, and all other biological processes. Therefore manipulation of cells is a fundamental technique in biology and medical biotechnology. Because of their small size ranging from hundreds of nanometers to tens of micrometers, and their dense population, one needs more advanced techniques and subtle devices, instead of traditional tweezers and pipettes, in order to physically access the cells. Thanks to the rapid development of lab-on-a-chip technology in the recent decade, researchers can now do cell loading, docking, culturing, sorting, lysis, detection and even single-cell on-chip analysis (Toner & Irimia, 2005; Voldman, 2006; Dittrich et al., 2006; El-Ali et al., 2006). These cellular lab-on-a-chip devices are not simply scaled-down versions of conventional lab apparatus. They are equipped with various micro- and nano-technologies. The future of healthcare may be revolutionized by hand-held analyzers because of their advantages including dramatically reduced consumption of samples and reagents, high speed, integrated functions, automation and portability.

For cell manipulations various principles and methods have been developed in microsystems, such as the optical tweezers (Grier, 2003), electrokinetic methods (Li & Harrison, 1997), magnetophoresis (McCloskey et al., 2003), acoustic means (Hawkes &

Coakley, 2001), and dielectrophoresis (Washizu, 1990; Gascoyne & Vykoukal, 2002). Among the existing techniques for cell manipulations and separation, dielectrophoresis (DEP) may be the most popular method (Gascoyne and Vykoukal, 2002; Hughes, 2002). DEP arises from the interaction of a dielectric particle, such as a cell, and a spatially non-uniform electric field. Because electric fields can be scaled down easily at the microscale, a highly non-uniform electric field at a length scale comparable to cell size can be generated at relatively low voltages. The generated DEP force affects the dynamic behavior of the cells by inducing translational motion or reorientation. Therefore precise manipulation of single particle can be realized by controlling the electric field without mechanical moving parts. The magnitude of the DEP force is determined by the size and dielectric property of the particle. Since the relative dielectric polarization (and hence the dielectric response) of the cells depends on the driving frequency of the applied electric field, an alternating (AC) electric-field is usually applied to generate DEP forces of different magnitudes and directions. Therefore DEP devices may be reconfigured for separating other cell phenotypes by modifying field frequency or amplitude. The micro-structure required for DEP can be fabricated and integrated into the lap-on-a-chip system by conventional photolithographic techniques. All of the advantages have made AC-DEP currently one of the most popular methods for micro scale cell manipulation (Toner & Irimia, 2005).

As a common practice in the AC-DEP, an array of metal electrodes is embedded inside a microchannel network to generate a dynamic non-uniform electric field. Alternatively, the spatially non-uniform electric field can also be created under a DC electric field by specially designed structures, such as obstructions or hurdles using

electrically insulating materials. It was recently reported that the DEP force can be generated by a spatially non-uniform DC electric field for particle trapping and concentration in microsystems. Cummings and Singh (Cummings and Singh, 2000; Cummings and Singh, 2003) developed an insulator-based DEP device consisting of an array of insulating rods in a microchannel, within which the DEP trapping of 200 nm polystyrene particles has been realized. Lapizco-Encinas *et al.* (Lapizco-Encinas et al., 2004a) demonstrated selective trapping of polystyrene particles, live *E. coli*, and dead *E. coli* in arrays of insulating posts using DC electric fields. And they utilized this method for separation and selective concentration of mixtures of two species of live bacteria simultaneously (Lapizco-Encinas et al., 2004b). Austin and his co-workers (Chou et al., 2002; Prinz et al., 2002; Chou and Zenhausern, 2003) showed that DEP force created by insulating hurdles can be used for trapping of *E. coli* chromosomes in a DC electric field, and for concentrating and patterning of both single-strand and double-strand DNA in a low frequency AC field. By employing the same principle, Ying *et al*. (Ying et al., 2004) also investigated the trapping effect of the DNA near the tip of a nanopipette due to the local geometrical field-intensification. The benefits associated with this insulating material based DC-DEP technique are obvious:

1) insulators are less prone to fouling, thus they generally retain their function despite surface changes;

2) there is no embedded metal electrode, which greatly reduces the complexity of fabrication by using simple techniques such as soft lithography;

3) the structure is mechanically robust and chemically inert;

4) gas evolution due to electrolysis around the metal electrodes is avoided inside the channel because the spatially highly non-uniform electric field is generated by concentrating the electric field using the insulators; and

5) DC electric fields can perform both the DEP particle manipulation and the electrokinetic particle transport simultaneously in a microchannel.

Objectives

The major objective of this dissertation work is to theoretically and experimentally investigate the non-linear electrokinetic phenomenon, dielectrophoresis, and its effect on the electrokinetic motion of the particles or biological cells in suspension. As an important extension of this major topic, on-chip detection of the particles and biological cells using microfluidics-based resistive pulse sensing technique will be explored and demonstrated. Overall, microfluidics-based lab-on-a-chip devices will be developed for separation and detection of particles and biological cells using dielectrophoresis and resistive pulse sensing.

Outline of the Dissertation

The complete dissertation comprises the following major sections:

Chapter 1 serves as an introduction to the background and motivation of this work. A brief review of the latest applications and development of microfluidics and lab-on-chip technology are presented. Specifically the methods for particle manipulation using dielectrophoresis are discussed and compared.

Chapter 2 includes a broad literature review of the theories and state-of-the-art applications of the general electrokinetic phenomena, such as electrophoresis,

dielectrophoresis, induced-charge electrokinetics, etc., which occur in microfluidic systems and related to various particle manipulations. Special attention will be focused on a variety of applications with dielectrophoresis.

Chapter 3 presents the fundamental theory of the direct-current dielectrophoresis (DC-DEP) and its effect on the particle motion in the microchannel. A finite-element based numerical model is developed to simulate the particle motion using a Lagrangian tracking method, taking into consideration of the Stokes frictional force, electrophoretic force, and the dielectrophoretic force. As preliminary "proof-of-concept", we studied the DC-DEP effect on the particle trajectory shift after a rectangular block.

Chapter 4 demonstrates the practical applications of the DC-dielectrophoresis for separation of polystyrene particles and biological cells. The locally non-uniform electric field is generated by an insulating block fabricated inside a PDMS microchannel. The particle/cell experiences a negative DEP (accordingly a repulsive force) at the corners of the block where the local electric-field strength is the strongest. Thus the particle deviates from the streamline and the degree of deviation is dependent on the DEP force, which is proportional to the particle's volume. Combined with the electrokinetic flow, mixed polystyrene particles with difference of a few micro meters in diameter can be continuously separated into distinct reservoirs.

Chapter 5 shows a microfluidic system for particle separation combining the alternating current (AC) dielectrophoresis and pressure-driven flow for separation of particle/cell mixtures. The dielectrophoretic separation is achieved by a hybrid design using an insulating PDMS hurdle and a pair of embedded metal electrodes to generate localized non-uniform AC electric field. This design significantly reduces the negative

effects associated with the Joule heating and the exposure to the electric field. Mixtures of polystyrene particles of different sizes and yeast cells with polystyrene particles were successfully separated at AC electric field of 200 kHz.

As an important extension of the major topic of this dissertation, chapter 6 describes an on-chip resistive pulse sensing scheme for detection and enumeration of particles and biological cells. In the first stage for cell detection and enumeration, a system is developed integrating optical fluorescence detection with resistive pulse sensing enhanced by a metal oxide semiconductor field effect transistor (MOSFET). The absolute count of the CD4+ T cells and its percentage to the total lymphocytes can be analyzed quantitatively, which showed comparable accuracy to the results from the commercial flow cytometer. In addition, to improve the sensitivity of the system, symmetric mirror channels are designed with implementation of instrument amplifications, which significantly reduces the noise and achieves better signal-to-noise ratio.

Finally, chapter 7 summarizes the major findings and contribution of this work. Some interesting potential directions for further studies are briefly outlined.

CHAPTER II

LITERATURE REVIEW

Electrokinetics

The electrokinetic motion of the particles and cells refers to the migration of electrically charged cells or particles in liquid solution or suspension in the presence of an applied electric field usually provided by immersed electrodes. This electrokinetic phenomenon originates from the charge separation at the interface between two different phases. Generally, most surfaces will acquire a certain amount of electric charges when they are brought into contact with an aqueous (polar) medium. Some of the charging mechanisms are ionization, ion adsorption, and ion dissolution (Probstein, 1994). The surface charge, in turn, will influence the distribution of nearby ions in the solution. Ions of opposite charge (counter-ions) to that of surface are attracted towards the surface while ions of like charge (co-ions) are repelled from the surface. This electrostatic interaction together with the mixing tendency resulted from the random thermal motion of the ions, leads to the formation of an *electric double layer* (EDL): a compact layer and a diffuse layer (Figure 2-1). The electric double layer is a region close to the charged surface in which there is an excessive of counter-ions over co-ions to neutralize the surface charge, and these ions are distributed in a "diffuse" manner. Evidently there is no charge neutrality within the double layer because the number of counter-ions is greater than the number of co-ions. Upon application of a tangential external electric field, the interaction between the separated charge at the interface and the electric field will cause the relative

motion of either the liquid or the solid phase. For a fixed solid surface, the Coulombic force on the predominant counter-ions in the diffuse layer leads to a net migration of the mobile ions in the EDL. The momentum is transported to the adjacent and bulk liquid by viscosity, resulting in an electroosmotic flow (EOF) or electroosmosis (Figure 2-2). For a closed solid surface, such as a particle, which is freely suspended in an indefinite liquid, the Coulombic force acting on the net surface charge leads to the migration of the particle, i.e., electrophoresis. Together with several other effects, such as the diffusiphoresis, capillary osmosis, streaming potential, sedimentation potential, etc., electroosmosis and electrophoresis constitute the major family of electrokinetic phenomena (Lyklema, 1995; Hunter, 1989).

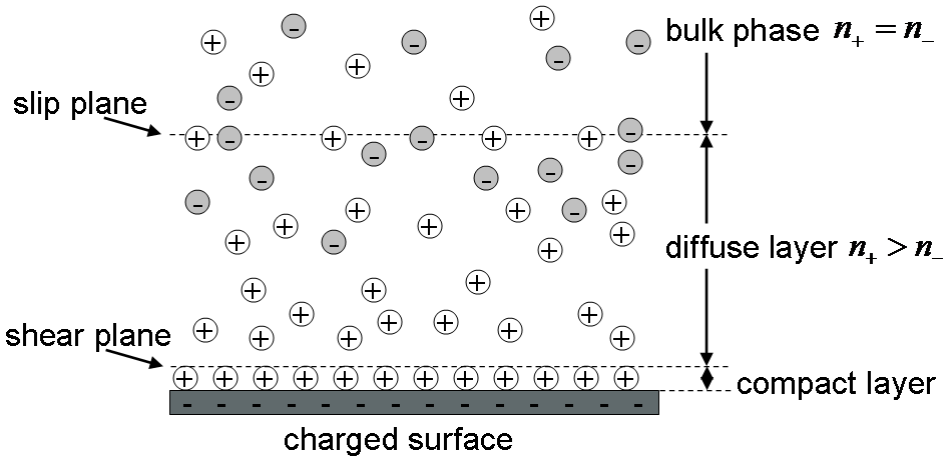

Figure 2-1 The schematic illustration of the electric double layer (EDL) structure.

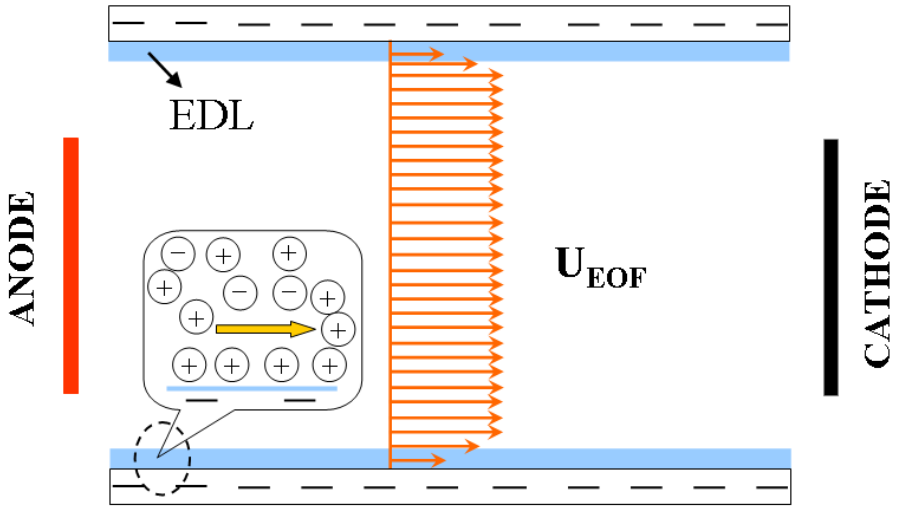

Figure 2-2 Generation of the electroosmotic flow (EOF). The velocity distribution of the EOF shows a characteristic plug-flow profile, which is different from the parabolic profile of the pressure-driven hydrodynamic flow.

Because the electric field can be easily scaled down to microscale, the electrokinetic force acting on a particle can therefore be scaled favorably for particle manipulations (Voldman, 2006). Since the well establishing of the fundamental theory more than three decades ago, scientists from various disciplines have been actively exploiting the electrokinetic phenomena for manipulation of biological particles, such as blood cells, bacteria, and macromolecules. This trend became more popular after late 1990s, when the advances of micro/nano-fabrication technologies gave rise to the microfluidics-based lab-on-a-chip devices. These miniaturized counterparts of the conventional room-sized biomedical equipments render excellent platforms for relevant biomedical manipulations and assays, because the biological reagents and particles exist in fluidic natural environment. The amazingly fast development of lab-on-a-chip

technology in recent decades has had profound impact on the healthcare industry (Stone and Kim, 2001; Mogensen et al, 2002; Wong et al, 2004; Huh et al, 2005; Toner and Irimia, 2005; Dittrich et al, 2006; Radisic et al, 2006; Dittrich and Manz, 2006; Whitesides, 2006; El-Ali et al, 2006; Yager et al, 2006; Chin et al, 2007; Sims et al, 2007; West et al, 2008) or biological defense against bioterrorism and biowarfare (Lim et al, 2005). Some of the competitive advantages of the lab-on-a-chip systems over the conventional biomedical instruments include: 1) their downscaling sizes make them highly portable, which is extremely attractive for on-site diagnosis; 2) the manufacturing and operational costs are significantly reduced making them disposable and affordable in resource-poor settings; 3) the dramatic decrease in sample and reagents consumption makes them work faster and further drive down the cost per unit test.

The electrokinetic motion of microparticles or cells in most lab-on-a-chip devices occurs in a confined space inside the microchannels under an applied electric field. Therefore we will focus this review on several important topics, including electrophoresis, dielectrophoresis, induced-charge electrokinetics, and some field effects on biological cells, which all occur in microchannel networks. However the extensive research works on the conventional electrophoresis and associated particle interactions will not be covered in this literature review. Hydrodynamic flow and EOF are two major methods for particle bulk transport in microsystems. Particle motion with the EOF is usually coupled with other electrokinetic phenomena and thus will not be discussed as an independent topic. Especially, more attention will be put in the extensive review of the non-linear electrokinetic phenomena, dielectrophoresis (DEP), and its various applications. In each section, the basic principle of the specific physical phenomenon will be described in brief.

The interesting and state-of-the-art theoretical and experimental methodologies, as well as their applications, developed in recent decades will be reviewed subsequently.

Electrophoresis

Like other colloidal particles cell have a surface charge that originates from the ionization of surface molecules and of the adsorption of ions from solution. The cell membranes contain numerous proteins, lipid molecules, teichoic acids, and lipopolisaccharides, which give them characteristic charge. Therefore cells undergo electrophoresis in a free solution with their own mobility depending on ionic strength and pH of buffer solution. For a system including a particle and a continuous suspending polar medium, a charge separation occurs at the solid/liquid interface. As shown in Fig. 2-3, the negatively charged particle is surrounded by a diffuse layer which contains excessive number of mobile ions of the opposite charge than that of the like charge. Charged particles move towards the electrodes of opposite electrical polarity under the uniform or homogeneous external electric field. This movement is due to the Coulombic force, generated by the interaction between the net charge on the particle and the applied electric field. The electro-migration of this particle is called electrophoresis.

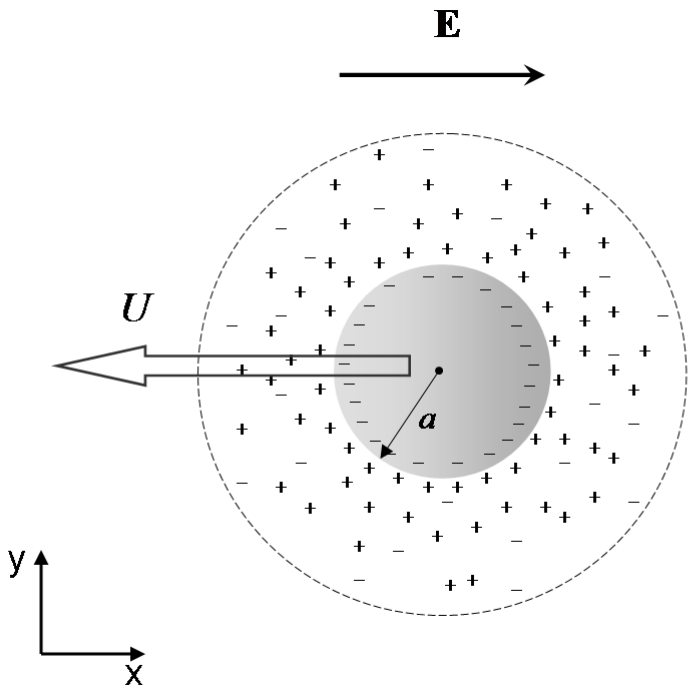

Figure 2-3 Schematic illustration of the electrophoretic motion of a spherical particle. The thickness of the double layer to the size of the particle is not drawn to scale.

The electrophoretic force acting on a particle with a net charge q under electric field strength of **E** is given by

$$\mathbf{F}_{EP} = q\mathbf{E} \tag{2.1}$$

The electrophoretic velocity with which the particle moves with respect to its suspending medium is proportional to the applied electric field strength by a factor called electrophoretic mobility. The electrophoretic mobility (at equilibrium) μ_{EP} is proportional to the magnitude of the net charge on the particle, and is inversely proportional to the size of the particle (Probstein, 1994).

$$\mu_{EP} = \frac{\mathbf{U}_{EP}}{\mathbf{E}} = \frac{q}{f} \tag{2.2}$$

where $\mathbf{U}_{EP}$ is the electrophoretic velocity and $f = 6\pi\mu a$ is the Stokes frictional factor for a spherical particle in a creeping flow. μ is the viscosity of the suspending medium and a is the radius of the spherical particle. Considering a thick diffuse layer, the particle may be treated as a point charge in an unperturbed electric field E_x, the electrophoretic velocity of the particle can be expressed as *Hückel equation* (Probstein, 1994)

$$\mathbf{U}_{EP} = -\frac{2}{3}\frac{\varepsilon_m \zeta_p}{\mu}\mathbf{E} \tag{2.3}$$

where ε_m is the permittivity of the suspending medium and ζ_p is the zeta potential of the particle, which is a measure of the surface charge density. Considering a thin diffuse layer, which is true for high ionic strengths or large particles of micron size, the electrophoretic velocity is given by the *Helmholtz-Smoluchowski equation* (Probstein, 1994)

$$\mathbf{U}_{EP} = -\frac{\varepsilon_m \zeta_p}{\mu}\mathbf{E} \tag{2.4}$$

This equation is similar to the expression of the electroosmotic flow velocity which is given by

$$\mathbf{U}_{EOF} = -\frac{\varepsilon_m \zeta_w}{\mu}\mathbf{E} \tag{2.5}$$

where ζ_w is the zeta potential of the channel wall. Actually the similarity between electrophoresis and EOF originates from the same charge-separation mechanism at the solid-liquid interface. EOF and electrophoresis refer to the relative motion of the liquid phase (close to a fixed solid surface) and solid phase (freely suspended in an infinite liquid domain), respectively.

It should be noted that Eq. (2.4) is derived for a particle in a infinitely large liquid medium, without any boundary effects on the particle's motion. However for the electrokinetic motion of a charged particle inside a microchannel, electrophoresis and EOF are not independent to each other. Neglecting the polarization and the retardation effects under the thin EDL assumption, the electrophoretic force is given by (Probstein, 1994)

$$\mathbf{F}_{EP} = 6\pi\zeta_p\varepsilon_m a\mathbf{E} \tag{2.6}$$

The Stokes frictional force on a charged particle is due to the relative motion of the particle with regard to the EOF is given by

$$\mathbf{F}_{stokes} = -6\pi\mu a(\mathbf{U}_p - \mathbf{U}_{EOF}) \tag{2.7}$$

Performing a force balance between Eqs. (2.6) and (2.7), i.e., $\mathbf{F}_{stokes} + \mathbf{F}_{EP} = 0$, and substituting Eq. (2.5), one can derive the expression for the apparent velocity of the electrokinetic motion of a spherical particle, given by

$$\mathbf{U}_p = -\frac{\varepsilon_m(\zeta_w - \zeta_p)}{\mu}\mathbf{E} \tag{2.8}$$

It can be inferred from Eq. (2.8) that the apparent velocity of the particle comprises two components: electroosmotic velocity and electrophoretic velocity. The directions of the two components are opposite to each other, which implies that the particle always moves in the same direction as the predominant factor. In practice, the zeta potential of the polymer channel wall is usually much greater than the zeta potential of the polystyrene particles and thus the particles demonstrate a net motion in the same direction as the electroosmotic flow. Therefore EOF is usually applied as a popular method for particle transport in microchannels. It should be noted that the assumptions

behind Eq. (2.8) imply that the electric field and flow field around the particle are all symmetric. If the separation distance between the particle and the channel wall is significantly small, due to the density difference between the particles and the suspending liquid, the flow field and electric field near the particle are asymmetric. In this case, the separation distance from the wall, and the relative size of the particle/cell to the channel's diameter play important role in determining the velocity of the particle/cell's electrokinetic motion (Ye et al. 2005; Xuan et al. 2005; Xuan et al. 2006).

Dielectrophoresis

Principle

Dielectrophoresis (DEP) arises from the interaction between a dielectric particle (usually with the dielectric suspending medium) and a non-uniform electric field (Pohl, 1978; Jones, 1995; Morgan and Green, 2002). As shown in Fig. 2-4, a dielectric particle and the suspending medium become polarized when they are subjected to an electric field. Because of the polarization, electric charge separation occurs within the dielectric particle as well as in the liquid side of the solid-liquid interface, giving rise to a dipole moment. The effective dipole moment of a spherical particle is given by (Jones, 1995; Morgan and Green, 2002)

$$\mathbf{p}_{\text{eff}} = 4\pi\varepsilon_m a^3 \cdot \mathbf{K}_{\text{CM}}(\varepsilon, \sigma, \omega) \cdot \mathbf{E} \tag{2.9}$$

where K_{CM} (ε, σ, ω) is the Clausius-Mossotti (CM) factor, which is dependent on the dielectric properties of the particle and the suspending medium, as well as the frequency

of the external electric field. CM factor is a measure of the effective polarizability of the particle in the medium and is given by

$$\mathbf{K}_{\mathrm{CM}} = \frac{\varepsilon_p^* - \varepsilon_m^*}{\varepsilon_p^* + 2\varepsilon_m^*} \tag{2.10}$$

where $\varepsilon_{p,m}^*$ are the complex permittivities of the particle and medium, respectively. For homogeneous particle and medium, the complex dielectric constant is given by

$$\varepsilon_{p,m}^* = \varepsilon_{p,m} + \frac{\sigma_{p,m}}{j\omega} \tag{2.11}$$

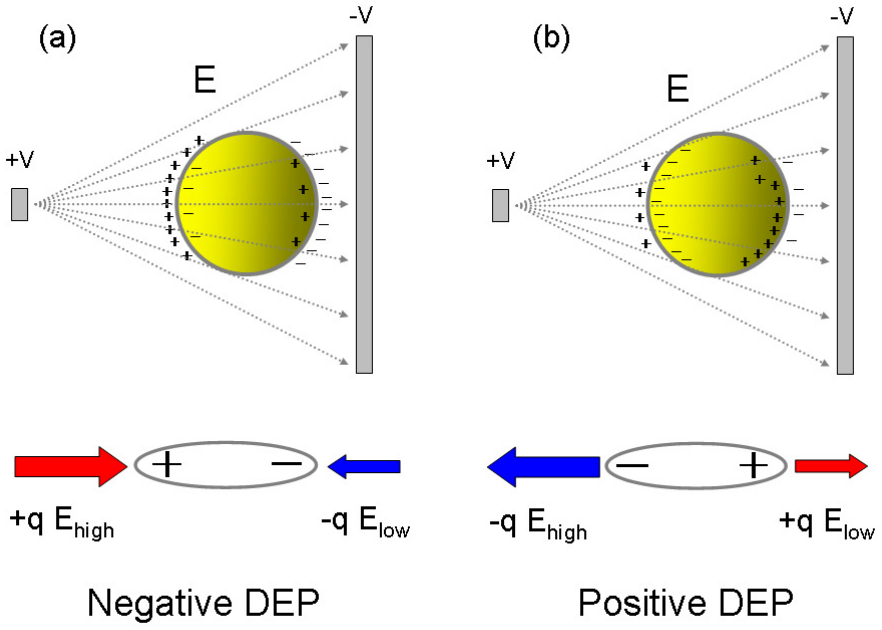

Figure 2-4 Schematic illustration of the dielectrophoretic motion of a spherical particle. (a) In this case the suspending medium is more polarizable than the particle. The induced dipole moment pointed to the electric field maxima. Because the repulsion force on the positive-charged end is greater than the attraction force on the negatively-charged end, the electrophoretic motion of the particle is away from the local electric field maxima, and is called negative DEP. (b) Under similar analysis, for the case when the particle is more polarizable than the suspending medium, the electrophoretic motion of the particle is towards the local electric field maxima, and is called positive DEP. The non-uniformity of the electric field to the size of the particle is not drawn to scale.

Different from the electrophoretic force that is the Coulombic force on the net charge of the particle as in Eq. (2.1), the dielectrophoretic force is actually the net of the unbalanced Coulombic force acting the induced dipole. In terms of the dipole moment, the DEP force is given by (Jones, 1995; Morgan and Green, 2002)

$$\mathbf{F}_{DEP} = \mathbf{p}_{\text{eff}} \cdot \nabla \mathbf{E} = 2\pi\varepsilon_m a^3 \cdot \mathbf{K}_{\text{CM}}(\varepsilon, \sigma, \omega) \cdot \nabla |\mathbf{E}|^2 \tag{2.12}$$

Eq. (12) implies that the strength of the DEP force depends strongly on the dielectric properties of the medium and the particle, particle's shape and size, as well as the frequency, amplitude, and the non-uniformity of the electric field. However, this force does not require the particle to be electrically charged. As long as there is an induced dipole moment, all of the particles exhibit dielectrophoresis in the presence of a non-uniform electric field.

When a charged dielectric particle translocates through a region with non-uniform electric field inside a microchannel, the electrokinetic motion of this particle is the combination effect of EOF, electrophoresis and DEP. The force balance on a particle at steady-state satisfies $\mathbf{F}_{stokes} + \mathbf{F}_{EP} + \mathbf{F}_{DEP} = 0$. Substituting Eqs. (2.5) - (2.7) and (2.12), the apparent electrokinetic velocity of the particle can be derived as

$$\mathbf{U}_p = -\frac{\varepsilon_m(\zeta_w - \zeta_p)}{\mu}\mathbf{E} + \frac{\varepsilon_m a^2 \cdot \mathbf{K}_{\text{CM}}(\varepsilon, \sigma, \omega)}{3\mu} \cdot \nabla |\mathbf{E}|^2 \tag{2.13}$$

The second term in Eq. (2.13) denotes the DEP component in the electrokinetic motion of the particle subjected to a non-uniform electric field in a microchannel.

DEP affects the dynamic behavior of the particles by causing translational motion or re-orientation. Because the electric field can be easily scaled down to microscale, a highly non-uniform electric field at a length scale comparable to the particle size can be

generated at relatively lower voltages. The non-uniform electric fields required for DEP can be generated by various methods, such as the static spatial variation (DC-DEP), the dynamic time variation (AC-DEP), or the variations coupling time and space (electro-rotation, travelling-wave DEP, moving DEP). In this section we will review, by physics, a variety of popular methods for dielectrophoretic manipulations of microparticles or cells.

Alternating current-dielectrophoresis (AC-DEP)

As implied by Eq. (2.12), the strength and the direction of the dielectrophoretic force is strongly dependent on the dielectric properties of the particle and suspending medium, on the particles' shape and size, as well as the frequency of the external electric field. A straightforward method to change the DEP force is to change the driving frequency of the electric field. Over the whole spectrum of the driving frequency, different type of cells or particles exhibit distinct response profile ranges from positive DEP (pDEP) to negative DEP (nDEP), which has been applied successfully in separation of different cell sub-populations. In order to generate non-uniform electric field in the microchannels, the common practice of the conventional AC-DEP includes the fabrication of an array of metal electrodes embedded inside the microchannel networks. According to the various applications, the AC-DEP has been extensively implemented in cell/particle separation, positioning or patterning, focusing, and other applications.

Separation

Cell or particle separation is one of the most important applications and has attracted most of the researchers in this area. According to the particle mobility after separation, the AC DEP can be categorized into FFF (field flow fractionation), in which the separated particles are continuously moving and inducted into specific channels, and non-FFF, in which the separated particles are statically collected in specific locations.

The investigations on non-FFF DEP separation of cells was started as early as 1960s by Pohl (Pohl and Hawk, 1966; Crane and Pohl, 1968) et al and by Mason and Twonsley (1971). It has been found that the DEP properties of viable and non-viable yeast cells are different and they can be separated by positive dielectrophoresis using a simple two-electrode system (Pohl, 1978a, b). However, only poor separation efficiency was obtained in above early studies. It was until early 1990s, with the development of advanced microfabrication techniques, Gascoyne and Pethig et al (Gascoyne et al, 1992; Huang et al, 1992; Pethig et al, 1992; Marks et al, 1994; Becker et al, 1995) reported DEP separation system with interdigitated, castellated microelectrode arrays. Using appropriate driving frequencies, positive and negative DEP force are acted on different groups of cells. Cells under pDEP are collected and held in deep and steep-sided potential energy wells at the electrode edges, whereas cells under nDEP are retained as aggregations in shallow potential energy wells in the void space between adjacent electrodes. After flushing fluid over the electrodes, the cells previously retained between the electrodes are readily and selectively removed, whereas the cells attracted at the electrode edges are not easily dislodged, resulting in very high separation efficiency (Fig. 2-5). Following the same concept, Morgan and Green (Morgan et al, 1999; Green et al,

2000) used similar structure to separate submicron particles and virus. Unlike the larger microparticles such as cells, sub-micrometer particles are strongly influenced by thermal effects such as Brownian motion. However DEP force of sufficient magnitude can overcome the diffusion barrier and realize manipulation of submicron particles or even proteins (Washizu et al, 1994).

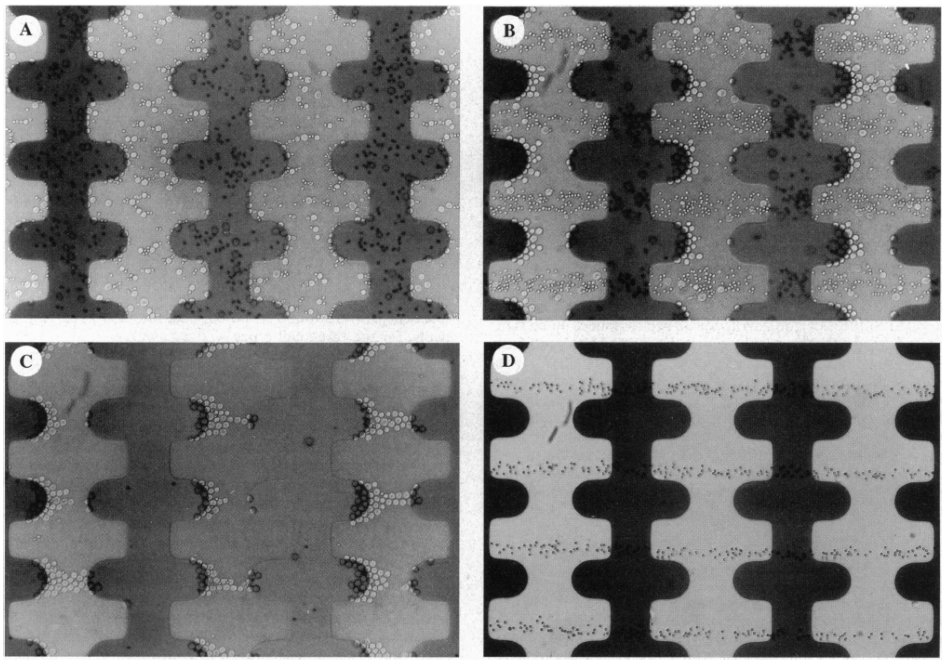

Figure 2-5 Separation of human breast cancer cell (large pale cells) from dilute peripheral blood. (A) During initial collection; (B) During release (flow from left to right); (C) cancer cells remained on the electrode edges after blood cells are flushed downstream; (D) Only blood cells (small dark cells) are collected at downstream (Becker et al, 1995).

In another non-FFF method, slim and planar interdigitated electrode arrays are used for lateral separation of particles or cells (Altomare et al, 2003; Zhou et al, 2005; Borgatti et al, 2005; Vulto et al, 2006; Chen et al, 2007; Fabbri et al, 2008; Zou et al, 2008). Compared with the conventional castellated electrode layout, this design is easier

for fabrication and the separated particle aggregations are more concentrated and potentially easier for collection and detection. The AC DEP force can also be employed in combination with other routines such as gravity (Arnold, 2001), laser trap (Arai et al, 2001), and electrowetting (Fan et al, 2008) for separation of microparticles or cells.

Different from the conventional non-FFF methods, the particles in dielectrophoretic FFF perceive DEP force that are acting at an angle to the fluid flow direction, and are continuously deflected into different streams according to their distinct dielectric properties (Fig. 2-6). The major advantage of DEP FFF lies in its continuous separation without any discrete flushing procedures.

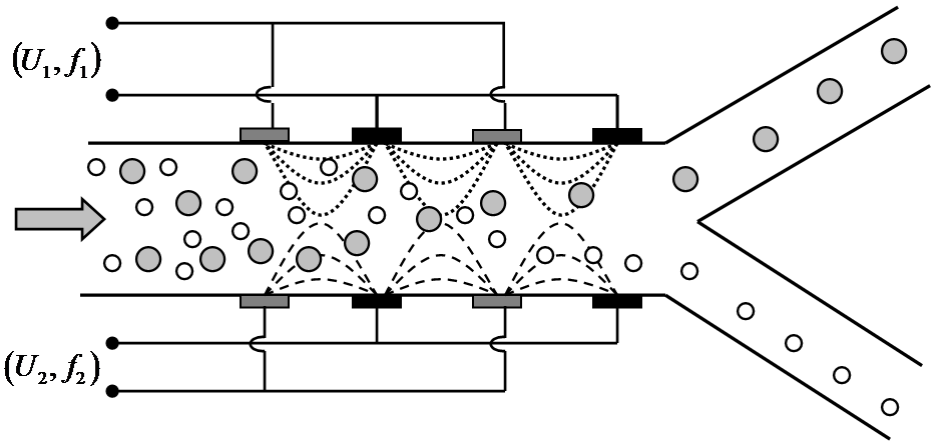

Figure 2-6 Schematic of dielectrophoretic field flow fractionation (Wang et al, 2007).

Using this concept, various on-chip separation function for particles or cells has been achieved with 2-D planar electrodes fabricated at the bottom of the channel, such as global electrodes with different shape and layout (Doh and Cho, 2005; Nieuwenhuis et al,

2005; Bligh et al, 2008), trapezoidal electrode array (Choi and Park, 2005; Lin and Yeow, 2007), and slim interdigitated electrode array (Kralj et al, 2006; Aldaeus et al, 2006; Li et al, 2007; Kim et al, 2007; Vahey and Voldman, 2008; Pommer et al, 2008; Han and Frazier, 2008; Vykoukal et al, 2008). Some other researchers implemented 3-D electrode arrays using more advanced fabrication techniques. Kentsch et al (2003) and Dürr et al (2003) developed microfluidic devices with 3-D micoelectrodes pairs on both top and bottom side of the microchannels as deflector structures to separate the micron and submicron particles according to their size. Holmes et al (2003) presented a pair of interdigitated arrays on top and bottom of the channel for particle focusing using nDEP with another single electrode array for particle separation using pDEP. Similar investigations have been presented by Hu et al (2005), Chen et al (2006), and Urdaneta and Smela (2008) using slanted electrode pair array. Park et al (2005) designed and fabricated wedge-shape 3D-asymmetric microelectrodes on the top wall with corresponding planar electrodes on the bottom wall of the channel for DEP separation of mouse embryonic carcinoma and red blood cells. Compared with the other typical 3D-microelectrode system, their asymmetric electrode system can generate continuously varied electric field and hence can induce DEP forces with more variation. The 3D electrode can also be fabricated on the side wall of the channel, which can generate DEP force in the transverse direction (Wang et al, 2007; Demierre et al, 2007; Demierre et al, 2008; Nascimento et al, 2008; Braschler et al, 2008; Tornay et al, 2008).

Inspired by both non-FFF and FFF separation methods, some researchers proposed hybrid DEP gate or filter-based separation schemes. A group of researchers from Sandia National Lab constructed DEP gates arranged perpendicular to the flow

(Bennett et al, 2003; James et al, 2006). It was found that the flow suspension had a field-induced phase separation and formed a distinct front between regions enriched with and depleted of particles. This controlled gating effect was demonstrated to concentrate and separate biological materials. Wang et al (2006) integrated a selective DEP filter array with two embedded optical waveguides for online monitoring of cell sorting. Two sets of polymer optical elements constitute two microchip flow cytometers, which are located both upstream and downstream of the DEP filter array. By comparing the cell counting rates measured by the two detection windows, the collection efficiency of the DEP filter can be determined. Similarly, Choi et al (2008) found the dielectrophoretic mobility of healthy and unhealthy porcine oocytes are different. They fabricated a castellated electrode array as a DEP filter that could trap the unhealthy oocytes and selectively release healthy ones for *in vitro* fertilization.

Positioning or patterning

It is another challenge in biomedical analysis to isolate and identify certain rare cells with specific biomarkers in blood, plasma and other clinical samples. AC DEP provides a versatile tool for on-chip positioning or patterning the biological particles in a desired location for subsequent detection, manipulation, and analysis. Various electrode layouts can generate DEP traps where the particles of interest are attracted and concentrated. There are a great variety of means of constructing such DEP traps, such as using the classical constellated arrays (Ramadan et al, 2006; Iliescu et al, 2006; Rajaraman et al, 2006), slim interdigitated arrays (Gagnon and Chang, 2005; Lagally et al, 2005; Forry et al, 2006; Yang et al, 2006; Gadish and Voldman, 2006; Suzuki et al, 2007;

Park and Beskok, 2008), quadruple electrodes (Morgan et al, 1999; Green et al, 2000; Bhatt et al, 2005), scattered planar electrodes (Krishnan et al, 2008; Urdaneta and Smela, 2008), 3D electrode post array (Park and Madou, 2005), or other interesting designs (MacQueen et al, 2008). In addition, in some layouts, not all of the electrodes need to be activated. Alternative approaches were reported to generate DEP force by combining active and electrically floating electrodes selectively (Yantzi et al, 2006; Golan et al, 2006; Golan et al, 2008). It is also worth to note that Chou et al (Chou et al, 2002; Chou and Zenhausern, 2003) proposed to construct DEP traps using insulating materials, such as glass, plastics, and polymers, instead of using metallic electrodes. This electrodeless DEP technique renders easier means for particle manipulation because of the simplicity of the device and the lack of metallic electrodes, which usually cause electrochemical reactions involving gas evolution. Moreover electrodeless DEP may be seamlessly integrated with metallic DEP layout and thus increase the flexibility in chip design.

Other than the batch manipulations such as separation or patterning, trapping single cells is an important tool for control of the cellular microenvironment. An appropriate cellular microenvironment is a critical factor in investigations in single-cell cultivation and proliferation, monitoring cellular life cycles, intercellular communications, and cellular functional responses to the external stimuli. By managing the cells' position and environment, parallel manipulations of the individual cells can generate data with higher reliability and statistical significance. Because DEP forces can be easily scaled down to single-cell scale and are sensitive to the change of the intracellular properties and extracellular interaction, DEP arrays provide an excellent platform for the single-cell assay and may reveal complex cellular processes which cannot be achieved by

manipulating mass cell population. Various designs of microarray have been reported to confine a single cell in a specific DEP cage (Fig. 2-7), such as using grid electrode system (Suehiro and Pethig, 1998; Fuchs et al, 2006), electrode rings (Taff and Voldman, 2005; Rosenthal and Voldman, 2005), scattered square or circular electrodes (Manaresi et al, 2003; Prasad et al, 2004), point-lid geometry(Gray et al, 2004), dipolar (Muys et al, 2005; Beck et al, 2008), and planar or extruded quadruple electrodes (Fuhr et al, 1998; Voldman et al, 2001; Voldman et al, 2002; Voldman et al, 2003; Rosenthal et al, 2006; Jaeger et al, 2008). The biological samples handled range from mammalian cells (Fuhr et al, 1998; Gray et al, 2004; Prasad et al, 2004; Muys et al, 2005; Voldman et al, 2005) to yeast (Jaeger et al, 2008) and bacteria spores (Beck et al, 2008). DEP trapping arrays can also be integrated with other techniques such as atomic force microscopy (Muys et al, 2005), fluorescent microscopy (Voldman et al, 2002), for sensing, cytometry, and other critical analysis.

There are other numerous applications related to the immobilization of particles or cells using DEP cage. Lee et al (2007) presented DEP tweezers to characterize the interaction between a particle and the surface. Negative DEP force is used to remove a particle from a surface and the force needed to remove the particle can correlate to the strength of the interaction between the particle and the surface. Borgatti et al (2005) reported a microdevice for programmable binding of microspheres to target cells for applications of drug delivery and diagnosis. They constructed DEP cages in which the microspheres were forced to bind with single tumor cells. Similar DEP electric barriers have been proposed for cell destruction (Menachery and Pethig, 2005), immnosensing

(Yasukawa et al, 2007), and distinguishing cells by measurement of their inherent dielectric properties (Fatoyinbo et al, 2008; Flanagan et al, 2008).

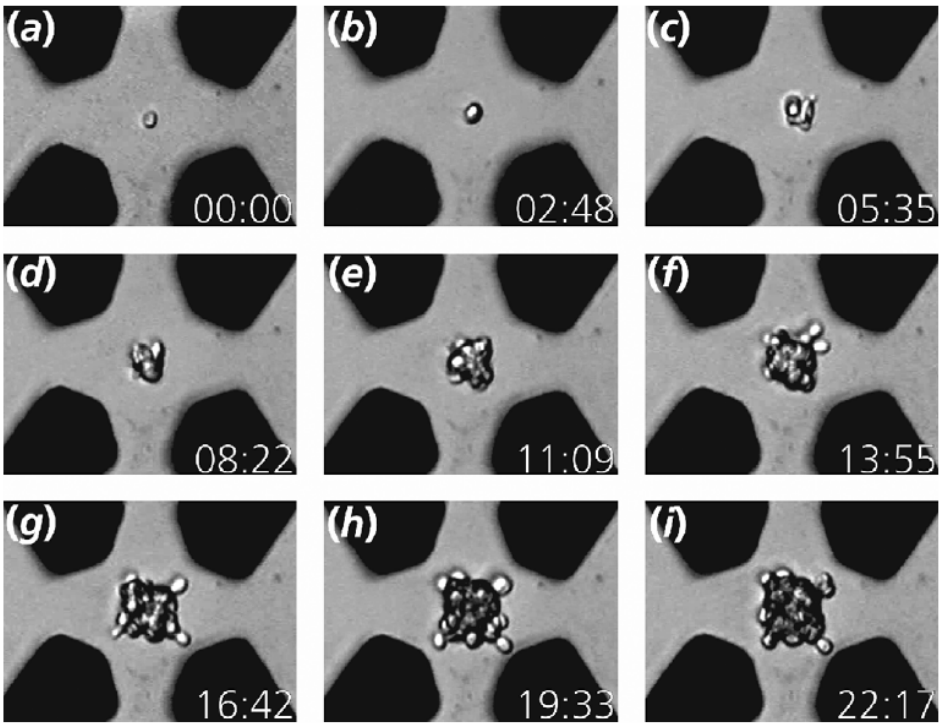

Figure 2-7 Yeast proliferation in an nDEP field cage. The quadruple dark blocks are microelectrodes. The image series shows a single yeast cell trapped and undergoes several divisions, finally resulting in cell agglomerate. (Jaeger et al, 2008)

Focusing

Flow cytometry is an important measurement of various physicochemical characteristics of suspended cells or other bioparticles. This system is typically performed in combination with optical probes to detect the different cell sub-populations with specific fluorescent labels. Before entering the detection window, the suspended cells are required to be focused into a shear stream so that the cells can be detected one by one at a high speed. Among the various hydrodynamic and electrokinetic focusing techniques,

DEP focusing is getting popular because of its design flexibility eliminating the shear flow, easy control by adjusting electric field, and high throughput in combination with hydrodynamic pumping. With other microfluidic techniques emerging in recent years, DEP focusing has contributed significantly in development of on-chip cellular flow cytometry (Huh et al, 2005). In DEP focusing, typically two sets of electrodes are fabricated to generate opposing DEP force which act on the particles and deflect the dispersed particles into a thin stream at the channel center (Fig. 2-8). The specific electrode design can be flexible with various layouts, such as dual convergent planar electrodes (Leu et al, 2005), elliptic electrode array (Yu et al, 2005), 2D or 3D wedge-shaped electrodes (Morgan et al, 2006; Holmes et al, 2006), or opposing liquid electrodes (Demierre et al, 2007).

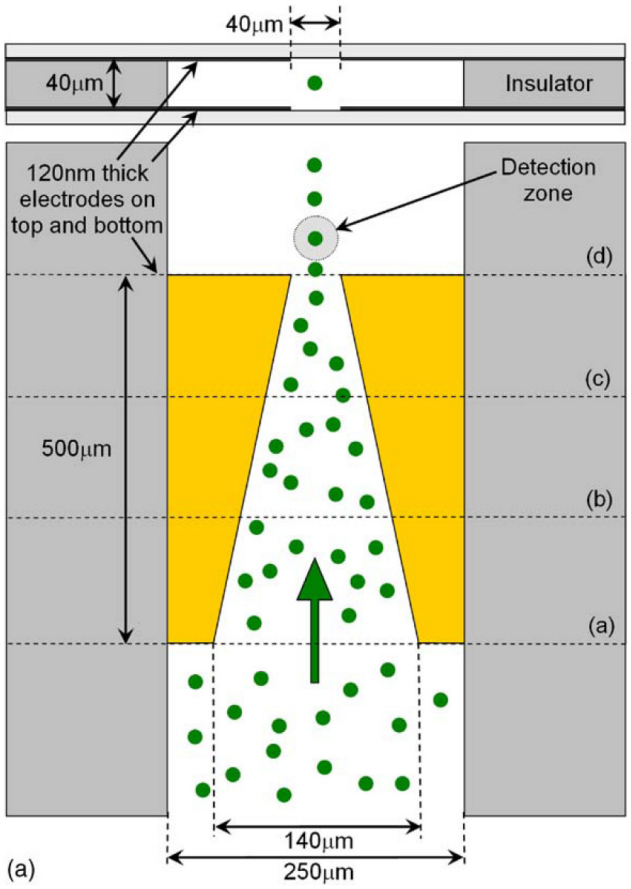

Figure 2-8 Schematic of the DEP focusing in the application of micro flow cytometer (Holmes et al, 2006).

Direct current-dielectrophoresis (DC-DEP)

As implied by the basic principle of dielectrophoresis, DEP force can also be induced by the interaction between a dielectric particle and a static (DC) non-uniform electric field. For fluid flows of electrolyte solution in an insulating microchannel subjected to an externally applied DC electric field, conservation of the electric current density **i** gives

$$\nabla \cdot \mathbf{i} = \nabla \cdot (\sigma_f \nabla \Phi) = -\nabla \cdot (\sigma_f \mathbf{E}) = 0 \tag{2.14}$$

Where σf is the electrical conductivity of the electrolyte solution, Φ is the electric potential, and $\mathbf{E} = -\nabla\Phi$ is the electric field. Neglecting the variation of the electrical conductivity of the electrolyte solution. Eq. (2.14) reduces to a Laplace equation.

$$\nabla^2\Phi = -\nabla \cdot \mathbf{E} = 0 \tag{2.15}$$

An important implication by Eq. (2.15) predicts that the static DC electric field is non-uniform in a microchannel with heterogeneous structures, such as a channel with varying cross-sectional area or constrictions created by hurdles or blocks.

A group of scientists from Sandia National Lab firstly proposed a method to generate spatially non-uniform DC electric field using arrays of insulating posts (made by glass or polymers) fabricated in microchannel systems (Cummings, 2003; Cummings and Singh, 2003; Lapizco-Encinas et al, 2004a, b; Lapizco-Encinas et al, 2005; Mela et al, 2005; Ozuna-Chacón et al, 2008). This novel method was also referred to insulator-based dielectrophoresis (iDEP) or electrodeless DEP. Strongly non-uniform electric field can be created within the constriction region between the adjacent insulating posts, where the dielectrophoretic force dominates over the diffusion, electroosmotic flow, and electrostatic repulsion among the particles and thus particles are trapped and concentrated. This interesting phenomenon has been applied for separation of live and dead bacteria (Fig. 2-9). Following this concept, Pysher and Hayes (2007) developed a device for sequential, spatially resolved DC-DEP separations with a series of progressively stronger electric field. The special pattern of the electric field variation was produced by a special design feature with opposing arrays of PDMS triangular extrusions from the channel wall. The separation distance of the tip pairs decreases along the flow direction, which causes that the local electric field gradient and hence the DEP force acting on the particles

increase. For a particle approaching the series of constrictions, if the negative DEP repulsion is less than the propulsion from the combined electrophoresis and electroosmosis, the particle will pass by this trap until it reaches a trap with a sufficient DEP force. Using this method, particles can be isolated according to their different physical properties, such as charge, polarisability, and deformity.

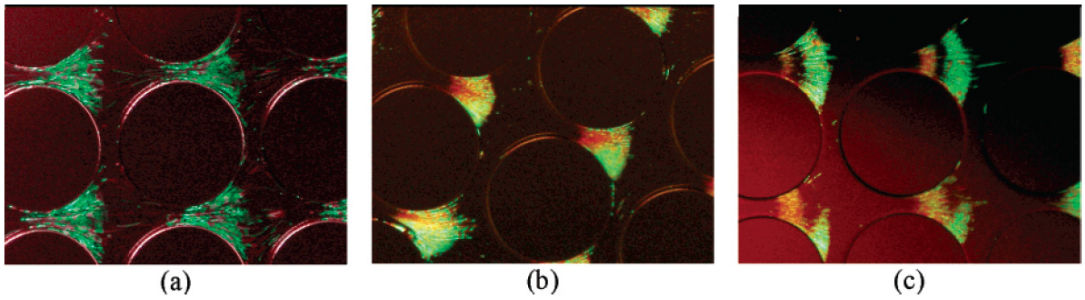

Figure 2-9 Simultaneous concentration and separation of live (green) and dead (red) E. coli: (a) at electric strength 16 V/mm, only live cells are trapped; (b) at 40 V/mm, differential banding on live and dead cells is observed; and (c) at 60 V/mm, differential trapping of live and dead cells is shown by two separate bands of different colors. The band separation is because dead cells exhibit less negative DEP than live cells. (Lapizco-Encinas et al, 2004).

Just as the other immobilization-based separation methods, the above DC-DEP separation needs discrete flushing or washing procedure to remove one component and collect another component subsequently. However, inspired by the early work of above-mentioned researchers, various insulator-based DC-DEP field flow fractionation (FFF) has been developed in recent years. Barrett et al (2005) demonstrated particle filtration and concentration using DC dielectrophoresis with 3D insulating ridges in the microchannel. The 3D insulating ridges were created using a two-level etching process on a glass substrate. Microparticles can be selectively deflected, trapped and concentrated because of the local non-uniform electric field formed near the ridges. As a real

application they used this device for continuously removing *B. subtilis* from a two-component sample mixture. Kang et al (2006a) found the electrokinetic motion trajectory of a particle can be elevated after it passes an insulating hurdle in a microchannel. This is because of the deflection by negative DEP force acting on a particle when it passes the corner of the insulating hurdle (Fig. 2-10). The magnitude of the repulsive DEP force is proportional to the particle size. Therefore a larger particle is subjected to a larger DEP force and tends to be deflected to a stream further away from the corner, in comparison with a smaller particle. By controlling the bulk electrokinetic flow at downstream, particles of different sizes can be inducted and collected in different channels. They have used this structure to achieve continuous separation of particle and biological cells by size (Kang et al, 2006b; Kang et al, 2008). Similarly Parikesit et al (2008) presented a microdevice with sub-micron deep channels for size separation of DNA macromolecules. DNA of various sizes are continuously deflected into different streams and finally collected in different outlets after they pass an insulating corner. Actually the DEP hurdle can also be created by insulating materials other than the polymeric PDMS. Barbulovic-Nad et al (2006) and Thwar et al (2007) reported creating hemispherical insulating hurdles using adjustable oil droplets introduced from side channels. Although it requires more delicate manipulation of the oil input, the shape and size of the oil hurdle can be dynamically adjusted, and so is the electric field and hence the DEP force for various separation parameters.

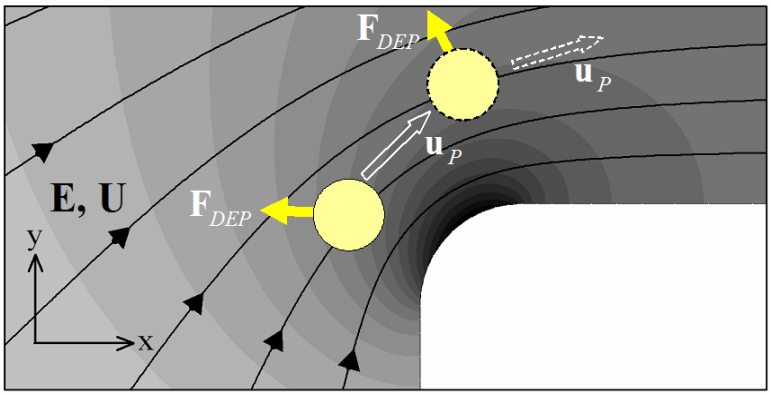

(a)

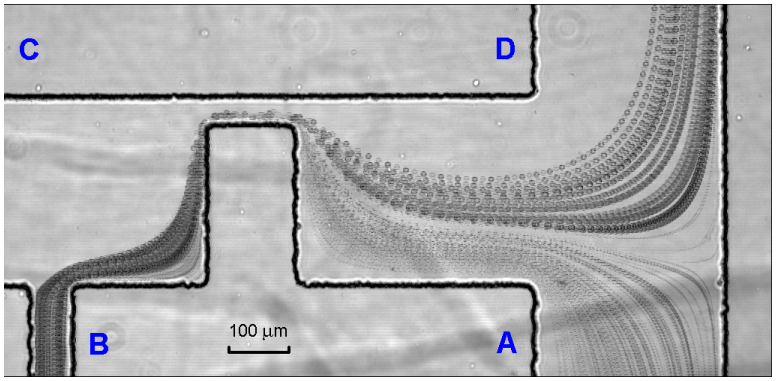

(b)

Figure 2-10 DC-DEP field flow fractionation using an insulating hurdle: (a) The electric field has a local maximum at the corner of the hurdle. Since the nDEP force directs to the local field minimum, the particle experiences a repulsive force when it moves around the corner of the hurdle. The magnitude of the repulsive DEP force is proportional to the particle size. Therefore a larger particle is subjected to a larger DEP force and tends to be deflected to a stream further away from the corner, in comparison with a smaller particle. (b) Separation of white blood cells (large dark dots going to the upper branch) from the other lysis debris (small dots going to the lower branch). Picture presented shows particles trajectories by superposing consecutive images obtained using an optical microscope (Kang et al, 2008).

Compared with the AC-DEP with embedded electrodes as introduced in the previous section, this DC-DEP technique has following major advantages: 1) insulators are less prone to fouling, thus they generally retain their function despite surface changes; 2) no metal components are involved which greatly reduces the complexity of fabrication by using simple techniques such as glass etching, and plastic stamping; 3) the structure is

mechanically robust and chemically inert, and hence is more biologically compatible; and 4) gas evolution due to electrolysis around the metal electrodes is avoided inside the channel. Some researchers have attempted investigating on hybrid systems combining AC-DEP and insulator-based DC-DEP. Hawkins et al (2007) has developed a DEP spectrometer that separates particles with a transverse outlet position specified by linear and nonlinear particle mobilities. Their device is characterized by coherently varying local DEP force with DC-biased, AC electric fields and a 3D constriction in channel depth.

Image DEP

As implied in Eq. (2.12), the DEP force originates from the non-uniformity of the electric field. In order to generate desired DEP force, alternative method has been developed using optically induced non-uniform electric field (Chiou et al, 2005), which is called image DEP (imDEP). In the first imDEP device, the liquid containing the particles is sandwiched between an upper transparent and conductive glass, and a lower photoconductive surface (Fig. 2-11). The two surfaces are biased with an AC voltage. When a dynamic image generated by a digital micromirror device (DMD) is projected onto a photoconductive layer, the impedance of the illuminated area becomes significantly smaller than the other "dark" area, which creates virtual electrodes and non-uniform electric fields for particle manipulation via DEP force. This device was also called optoelectronic tweezers (OET). Compared with the conventional laser optical tweezers, imDEP produces 100,000 times less optical intensity which can significantly reduce the damage on cells. Rather than using DMD projection, later researchers used

liquid crystal display (LCD) projector (Lu et al, 2005; Huang et al, 2006; Lu et al, 2007), len-less direct image transfer from LCD (Choi et al, 2007), and LCD integrated with condenser lens (Hwang et al, 2008). As a major advantage, imDEP offers both high resolution at single-cell scale and high throughput by massively parallel manipulation of a large number of cells traps. Moreover, the image pattern can be dynamically controlled by computer which cannot be realized by the conventional DEP devices with fabricated electrodes.

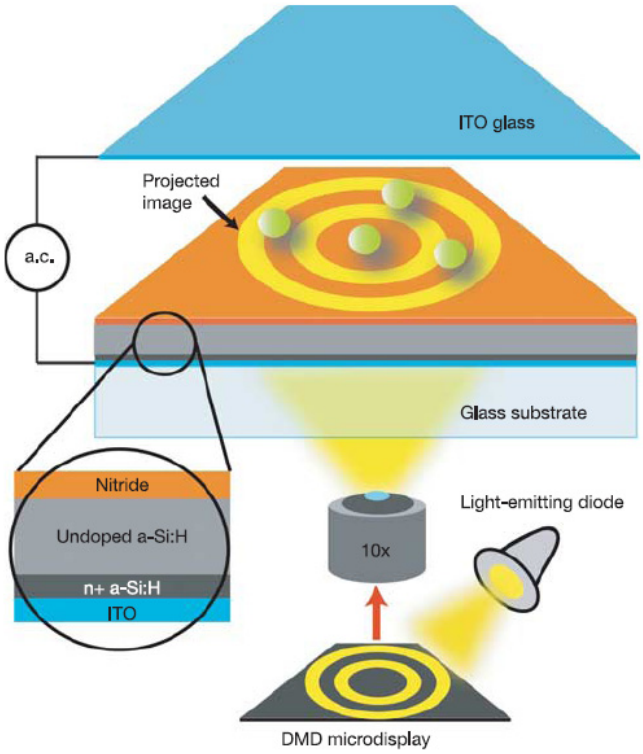

Figure 2-11 Device structure used in image DEP. The particle suspension is sandwiched between a conductive glass (on top) and a photoconductive surface (at bottom), which are biased with an AC voltage. The illumination source is an light-emitting diode. The optical image shown on the digital micromirror display (DMD) are focused on the photoconductive surface, changing the local conductivity and creating non-uniform electric field for DEP manipulation (Chiou et al, 2005).

Travelling wave-DEP (twDEP)

Another type of dielectrophoretic phenomena occurs due to the interaction between a polarizable particle and a travelling electric field generated by an array of electrodes on which the applied potentials have 90° phase variation between the adjacent electrodes. As shown in Fig. 2-12, a dipole moment is induced across the particle. In normal situation, the induced dipole in the particle should move with the travelling field peaks. However, if the travelling field is moving with sufficiently fast, the time taken for the dipole to form (relaxation time of the dipole) becomes significant and therefore the dipole will lag behind the field. The separation between the dipole and the field peak will induce net force acting on the particle resulting in a translational particle motion following the track of electrodes. It has been shown that the travelling wave DEP force exerted on a spherical particle of radius *a*, in a travelling field *E*, is given by (Huang et al, 1993)

$$F_{twDEP} = -\frac{4\pi\varepsilon_m a^3}{\lambda}\mathrm{Im}\left[\mathbf{K}_{\mathrm{CM}}(\varepsilon,\sigma,\omega)\right]\mathbf{E}^2 \tag{2.16}$$

where λ is the wavelength of the travelling field and $\mathrm{Im}\left[\mathbf{K}_{\mathrm{CM}}\right]$ is the imaginary part of the CM factor. Compared with Eq. (2.12), it can be inferred that the real and imaginary parts of the CM factor denote the in-phase and out-of-phase components of the induced dipole moment (as in Eq. (2.9)), which determine the conventional DEP and twDEP, respectively (Wang et al, 1994). Considering the balance between the twDEP force and the viscous drag force in equilibrium state, the translational velocity u of a particle in a travelling field is given by (Huang et al, 1993)

$$u_{twDEP} = -\frac{2\pi\varepsilon_m a^2}{3\lambda\mu}\mathrm{Im}\left[\mathbf{K}_{\mathrm{CM}}(\varepsilon,\sigma,\omega)\right]\mathbf{E}^2 \tag{2.17}$$

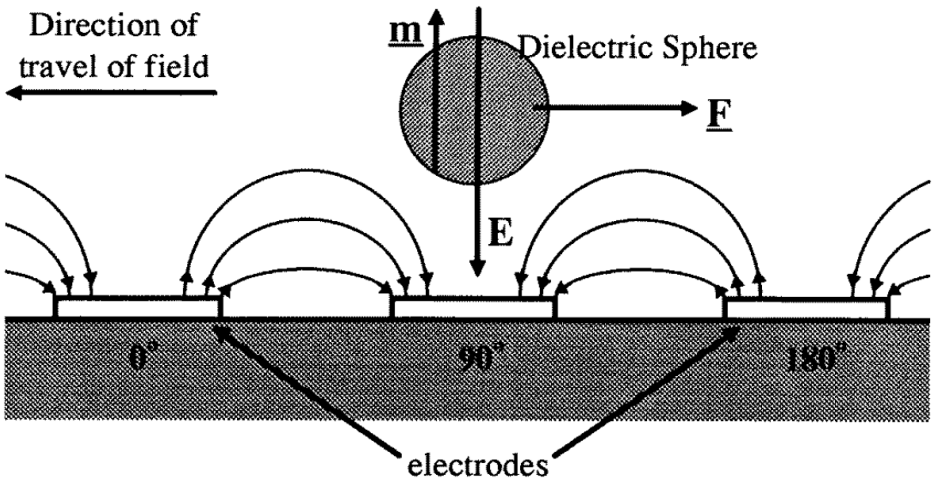

Figure 2-12 Schematic illustration of travelling wave dielectrophoresis (twDEP) of a spherical particle. The particle is levitated above the electrodes by nDEP. The electric field applied on the electrodes has a 90° phase variation between the adjacent electrodes. An induced net force F drives the particle translational motion due to the phase lag between the dipole m and the travelling field (Morgan et al, 1997).

Because the twDEP force and velocity, as in Eqs. (2.16) - (2.17), are determined by the particle size, the driving electric field, and the relative polarizabilities of the particle and suspending medium (through the CM factor), twDEP could be implemented in a variety of applications in particle manipulations. From late 1980s, several groups of scientists from Europe have conducted intensive investigations on twDEP both theoretically by analytical and numerical solutions (Wang et al, 1994; Hughes et al, 1996; Morgan et al, 2001; Green et al, 2002) and experimentally for biological applications (Huang et al, 1993; Wang et al, 1997; Goater et al, 1997; Morgan et al, 1997; De Gasperis et al, 1999; Cui and Morgan, 2000; Gascoyne et al, 2002; Cui et al, 2002; Pethig et al, 2003; Pethig et al, 2004). Subsequent works by more researchers in recent years have been done for modeling and developing more complex twDEP systems and applications (Du et al, 2004; Aubry and Singh, 2006; Nudurupati et al, 2006; Song and

Bennett, 2008; Shklyaev and Straube, 2008; Cen et al, 2004; Huang et al, 2007; Zhao et al, 2007; Felten et al, 2008; Higginbotham and Sweatman, 2008).

Electrorotation

Electrorotation is an analogue of twDEP and they both have the same origin due to the phase lag of the induced dipole with regard to a traveling electric field. However in electrorotation, the electrodes are arranged in a circular layout, usually with four electrodes and 90^{o} phase variation for adjacent electrodes. Therefore the electric field is traveling in circular manner instead of translational motion in twDEP. When a polarizable particle is suspended in the void center surrounded by the electrodes under a fast traveling field, the induced dipole will lag behind the rotation of the field resulting in non-zero angle between the field and the dipole (Fig. 2-13), which induces a torque in the particle and causes it to rotate asynchronously with the field. Generally the time-averaged torque Γ induced in a spherical particle of radius a suspended in a rotating electric field E is given by (Arnold and Zimmermann, 1988)

$$\Gamma = -4\pi\varepsilon_m a^3 \,\mathrm{Im}\left[\mathbf{K}_{\mathrm{CM}}(\varepsilon,\sigma,\omega)\right]\mathbf{E}^2 \tag{2.18}$$

Considering the viscous drag at equilibrium state, the rotation speed can be determined by (Arnold and Zimmermann, 1988)

$$\Omega = -\frac{\varepsilon_m}{2\mu}\,\mathrm{Im}\left[\mathbf{K}_{\mathrm{CM}}(\varepsilon,\sigma,\omega)\right]\mathbf{E}^2 \tag{2.19}$$

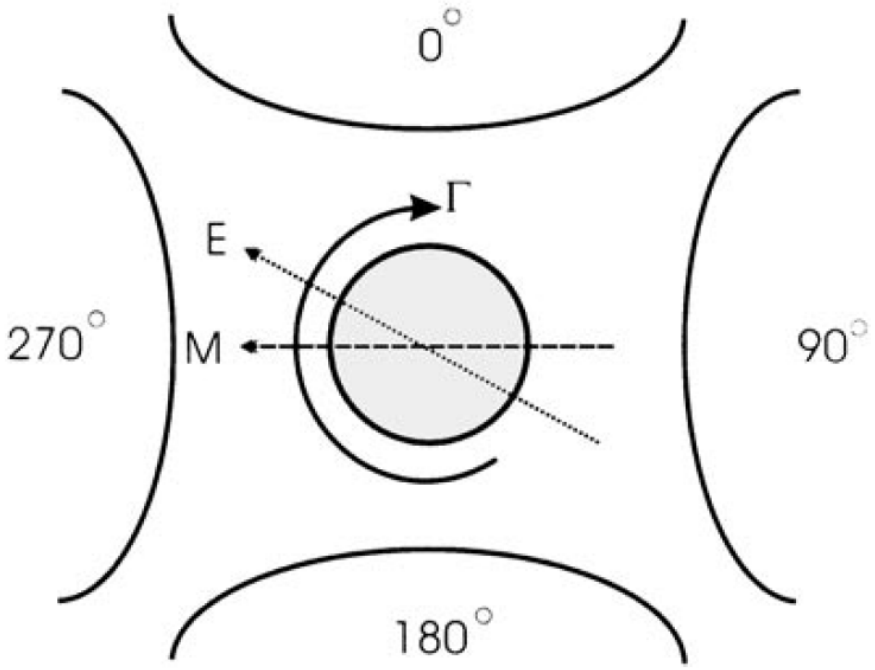

Figure 2-13 Schematic illustration of electrorotation of a particle suspended in a rotating electric field generated by four electrodes with 90° advancing phase (Hughes, 2000).

From Eqs. (2.16) - (2.19), the twDEP force and induced torque in electrorotation are proportional to the square of the electric field strength rather than the gradient of the square of the electric field strength, which determines the DEP force in Eq. (2.12). Moreover, the twDEP force and electrorotation torque depend on the imaginary rather than the real part of the CM factor. Above analysis implies that a particle may both conventional DEP and electrorotation or twDEP simultaneously. Actually the relationship of the inherent physics among conventional DEP, twDEP, and electrorotation phenomena has been reviewed by Hughes (2000). Since the electrorotation phenomenon was first observed, it has been extensively implemented in extracting the dielectric properties and characterizing the inner structures of single cells (Arnold et al, 1987; Gimsa et al, 1991;

Huang et al, 1992; Foster et al, 1992; Kakutani et al, 1993; Huang et al, 1995; Chan et al, 1997; Hözel, 1997; Gimsa and Wachner, 1998; Yang et al, 1999; Huang et al, 2002).

Moving DEP

Kua et al (2007; 2008) developed a hybrid method combining conventional AC-DEP and twDEP for separation and transporting microparticles across a microchannel. This proposed method is termed moving dielectrophoresis (mDEP) and is generated by sequentially energizing a single electrode or an array of electrodes to for a dynamic electric field that moves cells continuously along the microchannel. The cell separation is achieved by controlling the applied electric frequency, and the cell transportation is controlled by the electrode activation time. At appropriate frequency, cells experiencing negative DEP travel in front of the moving electric field, while cells experiencing positive DEP lag behind the moving field, which results in separation of a mixture of viable and nonviable cells according to their dielectrophoretic affinity (Fig. 2-14). A distinct advantage of mDEP is that cells can be transported uni-directionally without liquid pumping, irrespective of whether they experience positive DEP or negative DEP.

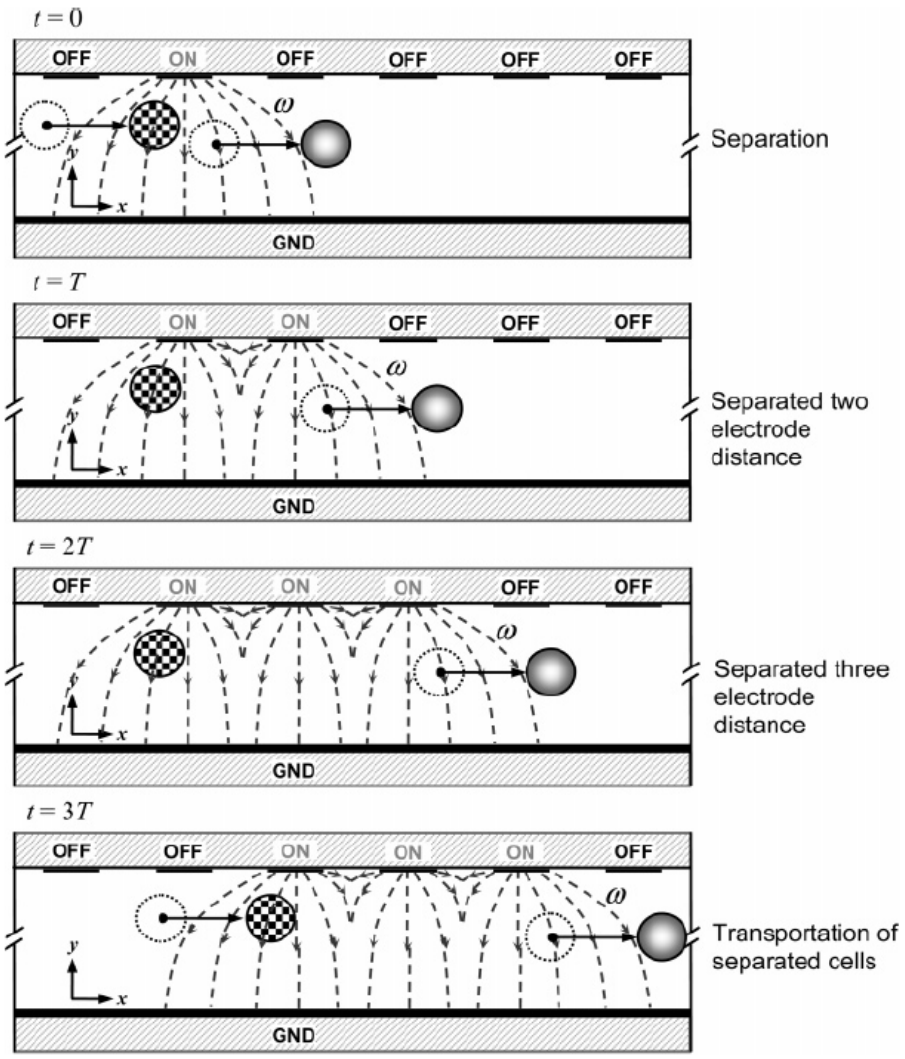

Figure 2-14 Cell separation and transportation under programmable moving electric field. The cell in pDEP is attracted in the DEP cage close to the electrode, whereas the cell in nDEP is repelled to the front of the moving field (Kua et al, 2007).

Induced-Charge Electrokinetics

Under an externally applied electric field, the body force acted on the electrically charged fluid in the double layer drives the ions and the fluid into a relative motion with respect to the solid surface. The resulting electroosmotic flow or electrophoresis appears to slip at a linear Helmholtz-Smoluchowski formula as in Eqs. (4-5). As discussed in the

previous sections, these classical linear electrokinetic phenomena have been well established and applied with a long history. However another interesting surface electrokinetic phenomenon, which occurs at an interface between an electrolyte solution and a highly polarizable surface, has been discovered in the most recent decades and cannot be explained by the classical linear electrokinetic theory. This unique phenomenon was termed induced-charge electrokinetics (ICEK), which refers to the non-linear electrokinetic slip at a polarizable surface. Several groups of Russian scientists firstly observed and attempted to describe the complex theory behind this phenomenon. However, their initial works remain unnoticed until early 2000s, when Squires and Bazant (Squires and Bazant, 2004; Bazant and Squires, 2004; Squires and Bazant, 2006) started to systematically construct the theoretical model for general ICEK and investigate its practical applications in the context of microfluidics.

Considering an ideally polarizable cylinder (e.g., an inert metal wire) of radius a fixed in an electrolyte solution and subjected to a suddenly applied, weak, and uniform electric field $\mathbf{E}$ (Fig. 2-15). In the very beginning, because of the potential cascade at the interface, the electric field lines intersect perpendicularly to the surface as in (Fig. 2-15a). An electric current $\mathbf{J}=\sigma\mathbf{E}$ drives positive ions in the aqueous solution into the charge cloud on one side of the conductor, and negative ions to the other, inducing an equal and opposite surface charge on the conducting surface and also attracting equal and opposite image charges within the conductor itself. Consequently, without considering surface conduction or Faradaic reactions to transfer the normal current at the surface, ionic charge accumulates in the double layer and this dipolar charge cloud grows until it reaches an equilibrium state and no field lines penetrate the double layer (Fig. 2-15b).

Now the bulk field lines are all repelled from the conductor and are parallel to the surface, which looks like the field lines around an insulator. However, the induced zeta potential on the conductor surface is obviously non-uniform because of the heterogeneous charge density in the double layer. Under the tangential field $E_{\|}$, a characteristic quadrupolar flow pattern is formed around the conductor driving fluid from the "poles" towards the "equator" of the conductor (in cross-sectional view in Fig. 2-15c). Reversing the direction of the external field E changes the polarity of the induced zeta potential everywhere at the interface. Therefore an AC field (up to the charging frequency $\omega_c = D\lambda_D a$, with λ_D the Debye screening length and D the ionic diffusivity) drives an identical net flow. The typical flow velocity of ICEK is given by (Bazant and Squires, 2004)

$$U_{ICEK} = \frac{\varepsilon_m a E^2}{\mu} \tag{2.20}$$

For a non-uniform electric field, Eq. (2.20) takes different form as (Bazant and Squires, 2004)

$$U_{ICEK} = \frac{\varepsilon_m a^2}{\mu} |\nabla E|^2 \tag{2.21}$$

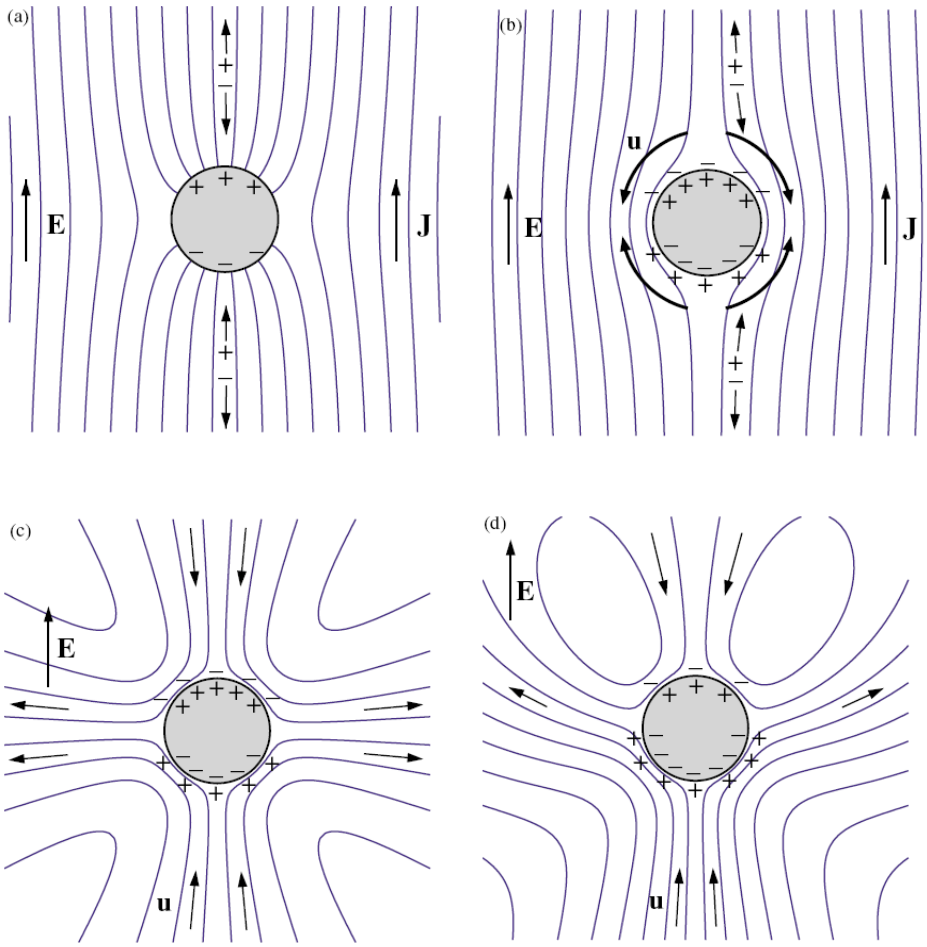

Figure 2-15 Induced-charge electrokinetics around a metal wire: schematics of electric field lines around a cylindrical metal wire fixed in an electrolyte (a) before and (b) after double layer charging in response to a suddenly applied DC field and (c) the resulting ICEK flow streamlines. The flow around a charged polarizable cylinder is shown in (d) (Bazant and Squires, 2004).

Some critical assumptions in Bazant and Squires' model include the weak electric field and small total zeta potentials. Violation of those assumptions causes complicated coupling of ICEK with other physics. Such flows have profound influence on the electrokinetic flow around a polarizable colloid particle (Mishichuk and Takhistov, 1995; Chu and Bazant, 2006; Zaltzman and Rubinstein, 2007) and the electrokinetic motion of

the particle itself (Ben et al, 2004; Yariv, 2005; Saintillan et al, 2006; Zhao and Bao, 2007), regardless of the shape or charge condition of the particle. Previous theories on the induced-charge electrokinetic motion of the particle are mostly based on the analytical modeling. Recently Wu et al (2008) developed a complete three-dimensional numerical model for the induced-charge electrophoretic motion of an ideally-polarizable spherical particle inside a microchannel. It was found that micro vortexes are generated in the fluid near the particle due to the varying slipping velocity along the particle surface. And a lifting effect occurs when the particle is moving close to an insulating boundary because of the interaction between the induced micro vortexes and the wall. Assuming steady-state Stokes flow and quasi-steady analysis based on force balancing on the particle, Kilic and Bazant (2008) showed that both attractive and repulsive particle-wall interaction may occur by varying the geometry of the particles or walls, as well as the AC frequency and voltage.

Due to the unique flow pattern of ICEK, the most straightforward applications are microscale pumping and enhanced mixing (Ben and Chang, 2002; Zhao and Bau, 2007; Wu and Li, 2008a,b). However, the theoretical description and experimental investigation of ICEK is challenging has not been fully developed yet, and more research effort is still under way in search of more comprehensive theory and discovering new phenomena.

Field Effects on the Biological Cells

There are some limitations associated with the manipulations of the biological cells using electric field. Two major problems are the electric field induced membrane stress and the Joule heating. The DEP force is proportional to the gradient of the electric

field intensity, $\nabla|\mathbf{E}|^2$. The electroosmotic flow is proportional to the electric field intensity, $\mathbf{E}$. Theoretically, application of a higher electric field can generate greater DEP force and stronger electroosmotic flow. However, we observed that live cancer cells die a short time after they are exposed to a very high voltage level, or when they pass through the narrow constriction in the microchannel, i.e., the gap region. This is because the strong DC electric field imposes a great stress on the cell membrane (Voldman, 2006). Therefore one cannot significantly increase the voltage to speed up the separation process and to increase the separation efficiency. The other side effect associated with high voltage is Joule heating, which causes significant temperature rise locally and can destroy the channel as well as the biological samples. It is known that a high temperatures (more than 4^{o}C above the cells' physiological temperature) leads to rapid mammalian cell death, and even a less extreme temperature increase may have negative physiological effects (Voldman, 2006). In addition, the cell membrane may also be damaged by some free radicals (Feeney and Berman, 1976), which can be generated by thermal decomposition and electrolysis at metal electrodes under the application of high voltage. Although some sugars work as free radical scavengers and some enzyme such as catalase and SOD (superoxide dismutase) provide significant protection (Thamilselvan et al., 2000), the temperature elevation because of Joule heating cannot be avoided. Furthermore there exist some natural physiological electric fields, which are inherent phenomena to the cells and control some critical cell behaviors (McCaig et al., 2005). The external electric field applied during electrokinetic cell manipulation will definitely interfere with the natural physiological electric field. Since the viability of the cells is critical for some subsequent analysis, it is highly important to optimize the chip design in order to improve the sample

viability. However, much work remains to minimize the negative effects associated with the application of the electric field.

CHAPTER III

EFFECTS OF DC-DIELECTROPHORETIC FORCE ON PARTICLE TRAJECTORIES IN MICROCHANNELS

A method of controlling the particle trajectory in a microchannel is demonstrated in this chapter. The method utilizes the DC-dielectrophoretic (DC-DEP) force created around an insulating hurdle in a microchannel under an applied DC electric field. This method does not require a complicated electrode array which is commonly used in the conventional AC-DEP system. The "proof-of-principle" experiments were carried out using a straight microchannel with a rectangle-shaped hurdle in the middle. The experiments showed that the trajectories of micron-sized particles can be controlled by the DEP force under electric-field strengths of 5 ~ 20 kV/m. To compare with the experimental results, the particle motion was simulated using a Lagrangian tracking method, taking into consideration of the electrophoretic force, the dielectrophoretic force, and the dielectric interaction between the particle and the channel wall. The numerical simulation based on the finite-element-method showed a reasonable agreement with the experimental data.

Introduction

Consider a suspension of dielectric particles in a dielectric fluid. In the presence of an applied electric field, the particle and the surrounding medium are electrically polarized and the surface charge accumulates at the interfaces due to the difference in electrical permittivity and conductivity of the particle and the liquid. The polarization

induces an effective dipole moment on the particle. A dipole is composed of equal amount of opposite charges separated by a distance, and tends to align in parallel with the local electric field. In a uniform electric-field, the Coulombic force acting on either charges of a dipole is the same in magnitude but opposite in direction. Hence the net force acting on the dipole is zero. In contrast, in a non-uniform electric-field, the forces acting on either charges of a dipole become asymmetric. As a result, there exists a non-zero net force which is called dielectrophoretic (DEP) force. The induced motion of the particle due to the DEP force is known as dielectrophoresis (Pohl, 1978). In the present chapter, we propose a DC-DEP method to control particle trajectory with an electrically non-conducting hurdle inside a microchannel under a DC electric field. The micro-particles are transported electrokinetically by the combined electroosmosis and electrophoresis. The particles will experience a DEP force due to the local non-uniform electric field when moving around the hurdle; particles' trajectories will be shifted after passing the hurdle. In order to prove the principle, we carried out experiments to study the effects of the particle size, applied voltage level, and the working electrolyte solutions. The results indicate that the particle-size-dependent characteristic of the DEP force can be utilized to separate particles by size continuously. For comparison with the experimental data, a numerical simulation of the electric field and flow field were conducted based on the finite-element method and a simple theoretical model of the particle trajectory was developed using the Lagrangian tracking method.

Assuming that the particle size is much smaller than the length scale of the spatial variation of the electric-field, and the electric double layer (EDL) is extremely thin compared with the micron-size particle submerged in an electrolyte solution (of molar

concentration about 10^{-3} M), the net DEP force acting on a non-conducting spherical particle of radius a under a non-uniform electric field $\boldsymbol{E}$ is expressed as (Pohl, 1978; Jones, 1995)

$$\mathbf{F}_{DEP} = 2\pi\varepsilon_f a^3 \tilde{f}_{CM} \nabla |\mathbf{E}|^2 \tag{3.1}$$

where ε_f is the electrical permittivity of the suspending medium. $\tilde{f}_{CM}$ represents the Clausius-Mossotti (CM) factor, which describes the relaxation in the effective polarisability of the particle. The low frequency limiting value of CM factor $f_{CM} = (\sigma_p - \sigma_f)/(\sigma_p + 2\sigma_f)$ depends solely on the conductivity of the particle and the suspending medium. Considering the case of insulating particle suspended in a conducting buffer solution, $\sigma_p = 0$ and $\sigma_f \mathbf{E} \cdot \mathbf{n} = 0$; the CM factor becomes -1/2. Accordingly, the net DEP force acting upon a spherical particle reduces to

$$\mathbf{F}_{DEP} = -2\pi\varepsilon_f a^3 (\mathbf{E} \cdot \nabla)\mathbf{E} \tag{3.2}$$

where ε_f is the electrical permittivity of the fluid. $\mathbf{E}$ is the electric field intensity. At the low frequency limit, the cell membrane blocks the DC current and causes the cell to behave like an insulating sphere (Jones, 1995). Thus expression (3.2) is also valid for a live cell. It can be inferred from Eq. (3.2) that the magnitude of the DEP force is proportional to the particle volumetric size ($4\pi a^3/3$) and the gradient of the electric field intensity ($\mathbf{E} \cdot \nabla \mathbf{E} = \frac{1}{2} \nabla |\mathbf{E}|^2$). The negative sign in Eq. (3.2) implies that the DC-DEP force always directs to the region of the lower electric-field strength. Thus it is also called negative DEP.

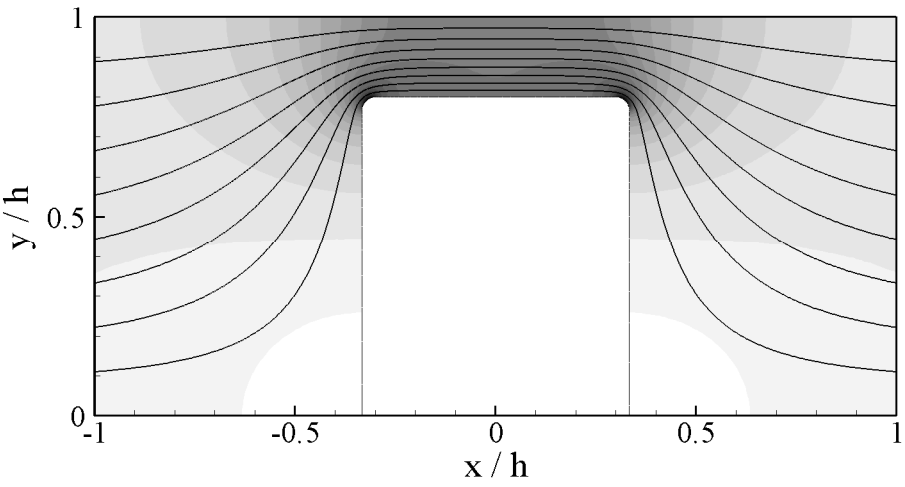

Figure 3-1 Contour of the electric field and electric-field lines around an insulating block in straight channel. The darkness level indicates the magnitude of *E*. The x-direction is the channel length (the flow) direction, and the y-direction is the channel width direction. The coordinates are normalized by channel width h.

In this work, we consider an electroosmotic flow (EOF) of an aqueous electrolyte solution inside a straight microchannel under an applied DC electric field. The liquid properties are assumed uniform throughout the channel. Joule heating effects are neglected (Xuan et al., 2004; Erickson et al., 2003). The channel walls are electrically non-conducting. Using the same material, an electrically non-conducting block is fabricated in the channel to create a locally non-uniform electric field. Fig. 3-1 illustrates the electric-field lines and the contours of the electric-field strength E around the hurdle. The x-y plane is the horizontal plan. The x-direction is the channel length (the flow) direction, and the y-direction is the channel width direction. There is a main channel (with block) in the middle section connected with four branch channels. Because the total current is conserved in any cross-section of the main channel, the electric field is

constricted in the gap region between the hurdle and the channel wall. Thus a stronger and non-uniform local electric field is created near the edges of the hurdle.

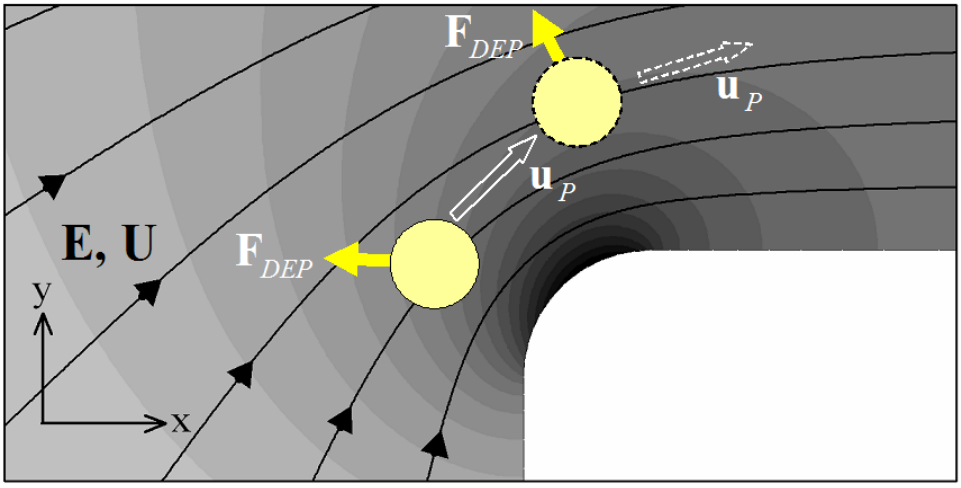

Figure 3-2 DEP force and its effect on a particle near the rectangular hurdle corner. The darkness level indicates the magnitude of the electric-field strength *E*.

Consider a particle passing though the entrance region of the gap due to the combined effect of the EOF and the electrophoresis (EP). As shown in Fig. 3-2, the electric field is stronger close to the corner of the block. Since the DC-DEP force directs to the region of the lower electric-field strength, the particle experiences a repulsive force when it moves near the corner of the block. The magnitude of the repulsive DEP force is proportional to the volume of the particle and the local value of $(\mathbf{E}\cdot\nabla)\mathbf{E}$. Therefore a larger particle is subjected to a stronger DEP force and tends to be pushed further away from the corner compared with a smaller particle. The similar DEP repulsion occurs when the particle passes by the other corner of the block. As a result, the cross-stream

trajectory shift (in y-direction) will be different for particles of different sizes and hence it is expected that they can be separated into different trajectories.

Simulation of the Particle Trajectory

For simulation of particle trajectory, the important assumptions made in this study are summarized here:

1) the particle and the channel walls are non-porous and non-reacting with the surrounding liquid;

2) the thickness of the EDLs close to the particle and the channel wall is very small compared to particle size;

3) the effect of surface conduction on the EDL is negligible;

4) the liquid properties are uniform throughout the domain;

5) the Reynolds number is much smaller than unity, and the creeping-flow assumption is valid;

6) rotation of the particle is either negligible or does not affect the particle's translational motion;

7) there exists no pressure-driven flow; and

8) any thermal effect due to Joule heating on flow and particle velocity is neglected.

Generally the instantaneous position of a particle $\mathbf{x}_p$ can be obtained by integrating the particle velocity $\mathbf{u}_p$

$$\mathbf{x}_p(t) = \mathbf{x}_0 + \int_0^t \mathbf{u}_p(t')dt' \tag{3.3}$$

where $\mathbf{x}_0$ represents the initial location of a particle and t is time period from the initiation. In a fixed frame of reference, the translational motion of a particle is governed by the momentum equation

$$m_p \frac{d\mathbf{u}_p}{dt} = \mathbf{F}_{ext} \tag{3.4}$$

where m_p represents the mass of the particle and $\mathbf{F}_{ext}$ the net external force acting on the particle.

In order to accurately predict the movement of a particle, the exact external force $\mathbf{F}_{ext}$ acting on the particle must be determined. Strictly speaking, the most accurate method of determining the force is to integrate the hydrodynamic stress tensor $\mathbf{T}^h$ and the Maxwell stress tensor $\mathbf{T}^e$ over the particle surface (Israelachvili, 1991).

$$\mathbf{F}_{ext} = \int_S \mathbf{T}^h \cdot \mathbf{n}\, dS + \int_S \left\| \mathbf{T}^e \right\| \cdot \mathbf{n}\, dS \tag{3.5}$$

where $\mathbf{n}$ denotes the unit vector normal to the particle surface pointing outward to the fluid. $\|F\|$ represents the difference of the function F between inside and outside of the particle surface. According to their definition, $\mathbf{T}^h$ and $\mathbf{T}^e$ are determined by the local hydrodynamic fields (pressure, flow) and the electric field, which are strongly coupled with the transient motion of the particle. To solve this problem, one should develop a three-dimensional transient model with a moving boundary which is a highly challenging task. By far many researchers have spent a lot of effort to develop such a complicated numerical model that can accounts for the hydrodynamic fields only. The detailed discussion is far beyond the scope of the present report. However, the purpose of the simulation in this work is to verify the concept and to provide a physical interpretation of

the experimental data. As such, we present a simplified model to predict the movement of a particle based on the Lagrangian tracking method (Cummings et al., 2000; Santiago, 2001).

In the Lagrangian tracking method, only the effect of the fluid on a moving particle is considered. The effect of the particle on the local flow field and electric field are neglected. Under these assumptions, we can easily solve Eq. (3.4) by explicitly separating the Stokes drag force from the other contribution in the total force $\mathbf{F}_{ext}$. Assuming the particle was initially at rest, the solution to Eq. (3.4) is given by (Morgan & Green, 2002; Castellanos et al., 2003)

$$\mathbf{u}_p = \left(\mathbf{u} + \frac{\mathbf{F}_{app}}{f} \right) \left[1 - e^{-(f/m_p)t} \right] \tag{3.6}$$

where $f = 6\pi\mu a$ is the Stokes frictional factor for a spherical particle in a creeping flow. $\mathbf{F}_{app} \equiv \mathbf{F}_{ext} - \mathbf{F}_S$ denotes the total applied force other than Stokes drag force $\mathbf{F}_S$. This expression gives the transient velocity for the particle after initiation. The exponential term describes the acceleration phase of the particle motion and has a characteristic time scale $\tau_p \equiv m_p / f \sim \mathrm{O}(a^2 \rho_p / \mu)$. For a particle of 10 μm in radius and a density of 1,000 kg/m^3, the characteristic time is about 10^{-4} sec, which is of orders of magnitude smaller than the time scale of the variation of the external forces as well as the time scale of experimental observation system. Therefore in the present situation, the particle appears to always move at a terminal velocity, which is given by (Morgan & Green, 2002; Castellanos et al., 2003)

$$\mathbf{u}_p = \mathbf{u} + \frac{\mathbf{F}_{app}}{f} \tag{3.7}$$

The major contributions to the applied force $\mathbf{F}_{app}$ considered in this study are the electrophoretic force $\mathbf{F}_{EP}$ and the DEP force $\mathbf{F}_{DEP}$.

$$\mathbf{F}_{app} = \mathbf{F}_{EP} + \mathbf{F}_{DEP} \tag{3.8}$$

For a spherical particle of radius a and with surface charge of ζ_p, neglecting the polarization and the retardation effects under the thin EDL assumption, the electrophoretic force $\mathbf{F}_{EP}$ in an electric field $\mathbf{E}$ is given by (Probstein, 1994)

$$\mathbf{F}_{EP} = 6\pi\zeta_p\varepsilon_f a\mathbf{E} \tag{3.9}$$

The DEP force acting on the spherical particle is given by Eq. (3.2) using a point-dipole model. In reality, the size of the particle is comparable to the length scale of the variation of the electric field, especially in the gap region close to the block corner. The magnitude of the actual DEP force will be different from that in Eq. (3.2). To account for this finite-size effect of the particle, we introduce a heuristic correction factor c to Eq. (3.2), which can be re-written as

$$\mathbf{F}_{DEP} = -2\pi c\varepsilon_f a^3 (\mathbf{E}\cdot\nabla)\mathbf{E} \tag{3.10}$$

where c approaches to unity for a sufficiently small particle compared to the length scale of electric-field gradient. Strictly speaking, the correction for size should be a local correction based on the local variation in the electric field, i.e., c is function of the electric field E and particle size a. However since the dependence of the local correction on the local electric field and the particle size is complicated and unknown, a zero-order approximation is applied by assuming that the correction for a particular particle size is universal (or constant). In addition, to make quantitative and more accurate analysis of the particle trajectories, a comprehensive CFD simulation needs to be conducted

considering the disturbance of particle to the local electric field and flow field, and also some other effects, such as the particle-wall interaction. The comprehensive simulation is significantly complicated and beyond the scope of the present work.

The direction of the force is always towards the liquid region from the wall, thus it is understood as wall-repulsion force. Substituting Eqs. (3.8) - (3.10) into Eq. (3.7), we obtain the particle velocity

$$\mathbf{u}_p = \mathbf{u} - \mu_p \mathbf{E} - \frac{c\varepsilon_f a^2}{3\mu}(\mathbf{E}\cdot\nabla)\mathbf{E} \tag{3.11}$$

where $\mu_p = -\varepsilon_f \zeta_p / \mu$ represents the electrophoretic mobility of the particle. It can be inferred from Eq. (3.11) that to obtain the particle velocity, the electroosmotic flow field $\mathbf{u}$ and electric field $\mathbf{E}$ in the microchannel have to be determined beforehand. In fact the major advantage of the Lagrangian tracking method is, as discussed previously, that the effect of the particle on the local flow field and electric field are neglected. Therefore they can be determined independently without considering the presence of the particles. The electric field is governed by the Laplace equation

$$\nabla^2 \phi = 0 \tag{3.12}$$

subjected to the boundary condition $\mathbf{E}\cdot\mathbf{n} = 0$, because the channel wall is electrically nonconducting. The electric field strength is determined by $\mathbf{E} = -\nabla\phi$, where ϕ is the electrical potential. The electroosmotic flow field is governed by the steady state Navier-Stokes equation

$$-\nabla p + \mu\nabla^2 \mathbf{u} = 0 \tag{3.13}$$

subject to the slip boundary condition $\mathbf{u}\cdot\mathbf{t} = -(\varepsilon_f \zeta_w / \mu)\mathbf{E}\cdot\mathbf{t}$, where ζ_w is the zeta potential of the channel wall, and $\mathbf{t}$ represents the unit vector tangential to the surface. It

should be noted that this slip boundary condition is only valid under the thin EDL approximation.

As such, the transient particle velocity can be determined by Eq. (3.11), and subsequently the particle trajectory can be obtained using Eq. (3.3).

Experiment

A PDMS (polydimethylsiloxane) microchannel of 300 μm in width (in y-direction) and 45 μm in depth (in z-direction) is fabricated using the soft lithography technique. The whole length of the channel is 2.8 cm. A rectangular block of 240~265 μm in width and 200 μm in length is fabricated at the center of the microchannel, as shown in Fig. 3-1.

In the fabrication process, the mold masters containing the microchannel patterns were made by spin coating of SU-8 photoresist on a clean glass slide. After two soft baking (65 °C for 5 min and 95 °C for 15 min), the photoresist film was exposed to UV light for 7 seconds using a 3500 dpi photo mask on which the desired channel pattern was printed. Following another two hard baking (65 °C for 1 min and 95 °C for 4 min), the slide was gently vibrated in the developer solution for 5 min to dissolve the unexposed photoresist, leaving a positive relief containing the microchannel pattern (with the block). Liquid PDMS was then poured over the master and cured in vacuum at 75 ºC for 3 to 4 hours. The negative PDMS cast of the microchannel pattern was then removed from the master, and two reservoir holes were punched. Immediately after plasma treating (PDC-32G, Harrick Scientific, Ossining, NY), the PDMS cast and a clean glass slide were bonded.

Fluorescent (carboxylate-modified) polystyrene microspheres of two different sizes, 5.7 μm and 15.7 μm in diameter (Bangs Laboratory Inc.), were used in our experiments. These particle sizes are similar to the size of typical biological cells such as the red blood cells and the white blood cells. The particles are supplied in the form of 1% suspension in pure water. The standard deviation in the size is ±1 μm for 15.7 μm particles, and ±0.3 μm for 5.7 μm particles. These particle solutions were further diluted with the working solutions used in the experiments, including de-ionized water, 1 mM KCl solution, and 1 mM sodium carbonate buffer (Na_2CO_3/$NaHCO_3$). The number density of particle is normally about 10^5/ml. Since the mass density of the particles is slightly greater than that of water (nominal density is 1.05 g/ml), the particle solutions were gently vibrated prior to use to prevent sedimentation.

The particles were introduced into the upstream reservoir with a 1-ml plastic syringe. A high-voltage DC power source (Glassman High Voltage Inc., High Bridge, NJ) was used to drive the fluid flow through two platinum electrodes submerged in each reservoir. In the experiments, the electric field was changed usually from 5 kV/m to 20 kV/m. The pressure-driven flow inside the channel was eliminated by carefully balancing the liquid level in two reservoirs before each experimental run.

Particle motion in the microchannels was monitored by an inverted optical microscope (Leica Microsystems, Richmond Hill, ON) and recorded by a progressive CCD camera (Pulnix America Inc., Sunnyvale, CA). The camera was run in video mode at 11.4 Hz with individual exposure times of 1/250 sec. The acquired images (viewed from the top) had a resolution of 640 × 484 pixels. The cross-stream position of a particle (y_1 for upstream and y_2 for downstream) are digitized manually to determine its trajectory

shift. The reading error to determine the particle positions was about ± 2 pixels which correspond to ± 5.4 μm.

Results and Discussion

In experiment, most of the data are acquired using the sodium carbonate buffer ($Na_2CO_3/NaHCO_3$, 10^{-3} M) as the working solution. In simulation, the zeta potentials of the PDMS channel wall and the particle are set to –80 mV and –32 mV, respectively (Ross et al, 2001; Staben and Davis, 2005). Because the concentration of the working solution is very low, the liquid properties are of no difference from that of DI water which are fixed as: dynamic viscosity 1.0×10^{-3} $kgm^{-1}s^{-1}$, density 998 kgm^{-3}, and permittivity 6.9×10^{-10} $CV^{-1}m^{-1}$.

Cross-stream trajectory shift

Series of superposed images of consecutive positions of the moving particles are shown in Fig. 3-3 for (a) two 5.7 μm particles and (b) three 15.7 μm particles with different incoming positions. The electric field strength is fixed at 20 kV/m and the flow direction is from left to right for both cases. It can be seen that all the particle trajectories are shifted in cross-stream direction (in y-coordinate). Two different trends of shift are observed from the experiment. When the incoming position of a particle is close to the lower wall (i.e., the wall with a block), its trajectory is shifted to the upper wall after passing the block, such as the particle *a*, *b*, *d*, and *e* in Fig. 3-3. This in fact confirms the effect of the repulsive DEP forces that the particle experience at the block corners. By comparing Figs. 3-3(a) and 3-3(b), it also can be concluded that the magnitude of the

trajectory shift for large particles (*a* and *b*) is greater than that for the small particles (*d* and *e*). This is because the DEP force is proportional to the particle volume according to Eq. (3.2). Hence the larger particle experiences a greater DEP force resulting in a greater trajectory shift. By far the experimental observations qualitatively confirm the prediction in section 3.2. However, when the incoming position of a particle is close to the upper wall, its trajectory is shifted to the lower wall after passing the block, such as the particle *c* in Fig. 3-3. This opposite trend implies the particle experiences a strong repulsive force from the upper wall. A quantitative analysis of the particle-wall interaction is provided in the appendix at the end of this chapter.

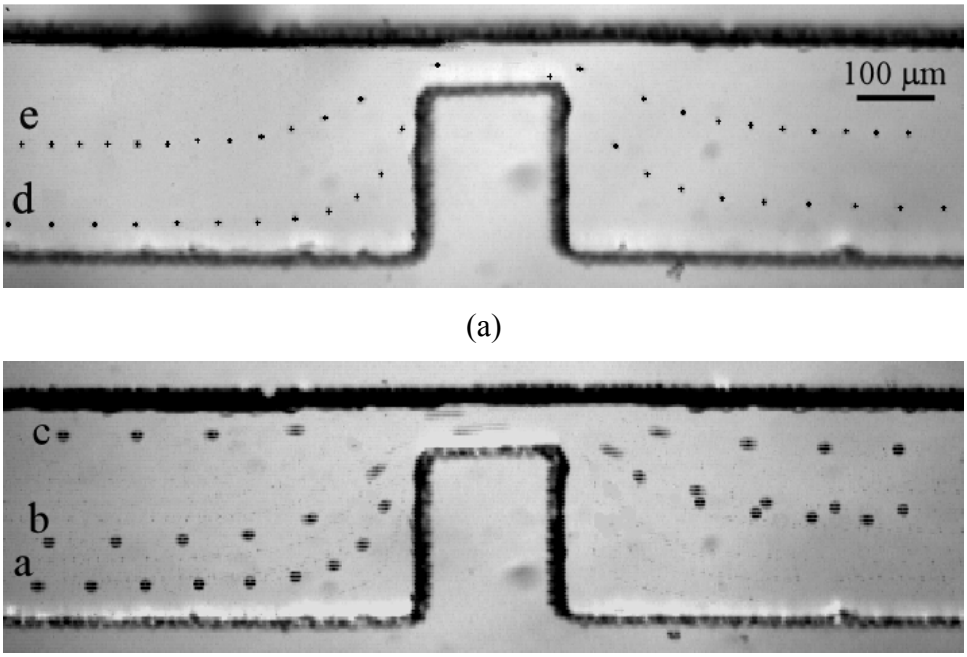

Figure 3-3 Superposed images showing the particle motion at E = 20 kV/m: (a) a = 2.85 μm; (b) a = 7.85 μm. Particles are labeled for the convenience of identification. Flow is from left to right. Time difference between the two consecutive frames are 0.088 sec.

To quantitatively compare the experimental observation with the prediction by the simulation in previous section, two different methods will be applied in the following.

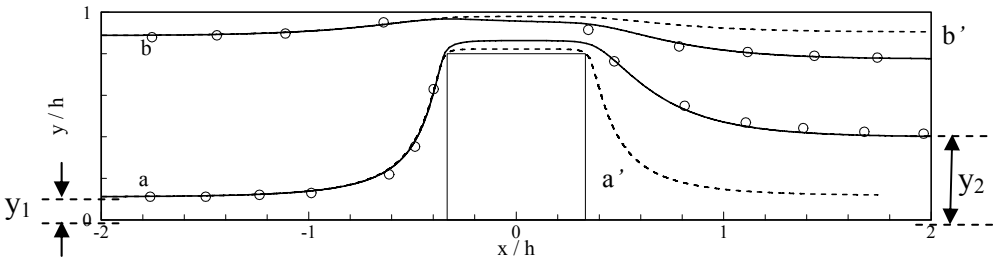

(a)

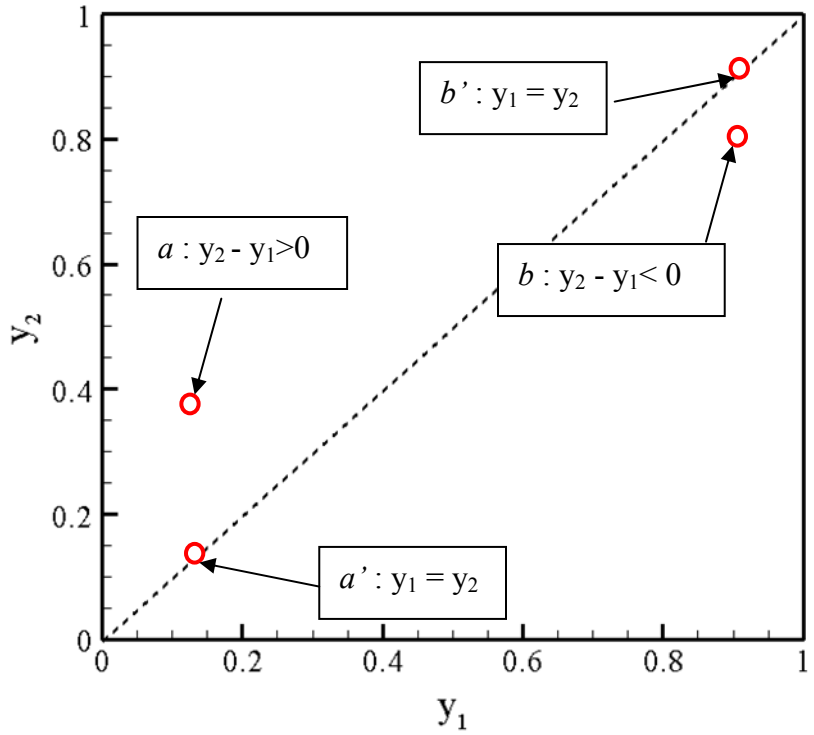

(b)

Figure 3-4 Motion trajectories of two particles of radius *a* = 7.85 μm under *E* = 20 kV/m. (a) Individual particle motion trajectory from the experimental results and simulation results: Solid line represents the computed results accounting for the DEP force and the wall effect. The dashed line *a'* is simulation result without considering the DEP force. The dashed line *b'* is simulation result without considering the wall repulsion. The symbols are the experimentally determined instantaneous locations of the particle. (b) Trajectory shift comparison. Dotted line is a reference line corresponding to $y_1 = y_2$.

The first method is to compare the individual particle motion trajectory. Fig. 3-4a shows the individual motion trajectories for two 15.7 μm particles at electric field strength 20 kV/m. Their incoming positions represent two typical cases: particle *a* is close to the lower wall, and particle *b* is close to the upper wall. The solid lines denote the simulated individual trajectories and the circular symbols denote the superposed particle position from the experimental results. According to Eq. (2.10), we introduced previously a correction factor *c* to account for the finite-size effect to the actual DEP force. We found that simulation results can give a close match to most of the experimental results by setting $c = 0.5$ for 5.7 μm particle and $c = 0.25$ for 15.7 μm particle. In order to show the trajectory shift is indeed because of the DEP force and the dielectric wall effect, we also manually removed the relevant force terms from Eq. (2.8) or Eq. (3.2) and computed the resulting particle trajectories, as shown by the dashed lines (*a'* and *b'*) in Fig. 3-4a. As anticipated, the particle trajectories show apparently no shift at downstream.

The second method is to compare the magnitude of the trajectory shift for a group of particles which have random incoming positions. The particle incoming positions at upstream (y_1) and outgoing positions at downstream (y_2) are shown in Fig. 3-4b. In this figure, each symbolic circle represents an actual particle, which has a certain incoming position at upstream (y_1) and a certain outgoing position at downstream (y_2). The entire graph is divided into two regions by the principle diagonal (as shown by the dashed line). For a particle (e.g., particle *a*) falling into the region above the diagonal, we call its trajectory shift is positive ($y_2 - y_1 > 0$), which is because of the DEP force. For a particle (e.g., particle *b*) falling into the region below the diagonal, we call its trajectory shift is negative ($y_2 - y_1 < 0$), which is because of the wall repulsion. And the particles without

trajectory shift (e.g., particle *a'* and *b'*) will fall right on the diagonal line. In addition, it can be easily inferred that a particle with a greater trajectory shift is located further away from the diagonal than one with smaller trajectory shift.

By using this method, Fig. 3-5 shows the magnitude of the trajectory shift for groups of 5.7 μm particles and 15.7 μm particles under two typical working voltages 5 kV/m and 20 kV/m. The simulation results are represented by the solid lines showing the predicted trajectory shift of particles coming at all cross-stream positions ($0<y_1<1$). The scatted symbols are experimental results for particles with random incoming positions. It can be seen that the experimentally observed trajectory shift fits reasonably well with simulation results. There are four major observations: First, particles with lowest incoming positions ($0<y_1<0.2$) have the greatest positive trajectory shift. As discussed in previous section, the intensity and gradient of the electric field is the greatest at block corner. Therefore if a particle moves at an incoming position closer to the lower wall, it will experience a stronger DEP force when it passes the block corner. Second, particles with highest incoming positions ($0.8<y_1<1$) have greatest negative trajectory shift. This is because the particle is subjected to strong dielectric wall repulsion when it comes too close to the upper wall. Third, positive trajectory shift for large particle is larger than that for small particle because the DEP force is proportional to the particle volume. And fourth, magnitude of the positive trajectory shift increases with increasing electric field strength because the DEP force is proportional to the value of $\mathbf{E}\cdot\nabla\mathbf{E}=\frac{1}{2}\nabla|\mathbf{E}|^2$. Based on the aforementioned observations, we can expect that, with a properly designed microchannel system, the particles of different sizes can be eventually separated into different streams after the block by controlling their trajectory shift.

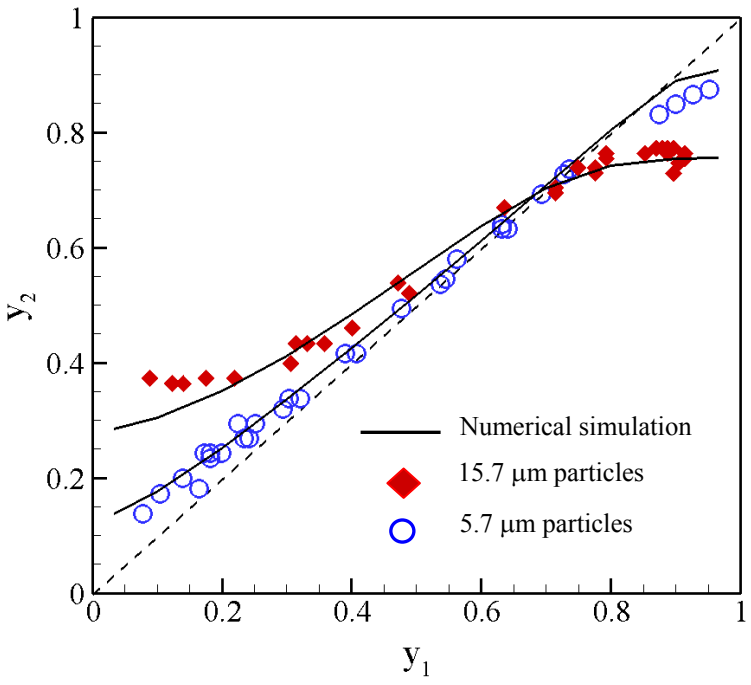

(a)

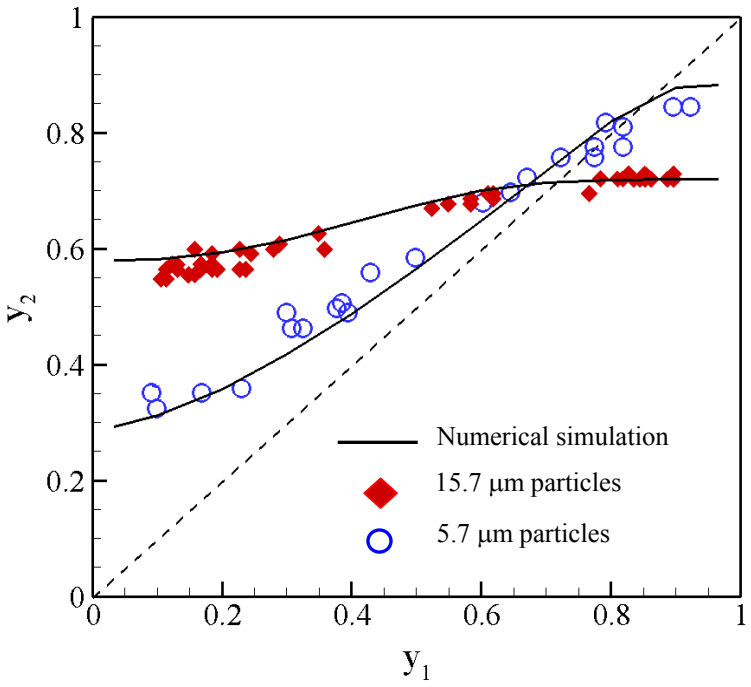

(b)

Figure 3-5 Magnitude of trajectory shift for particles of different sizes under different electric field strengths: (a) E = 5 kV/m; (b) E = 20 kV/m. Experimental results are denoted by the symbols and the numerical results are denoted by solid lines. Working solution is sodium carbonate buffer (Na_2CO_3/$NaHCO_3$, 10^{-3} M). The gap width is 45 μm.

In additional to the sodium carbonate buffer solution, two other liquids, including de-ionized water, and potassium chloride solution (KCl, 10^{-3} M), are also used to study the effect of working liquids. The experimental results for 5.7 μm particle trajectory shift in three different working fluids are shown in Fig. 3-6. However, there is no any noticeable difference in trajectory shift in different liquids. According to Eq. (3.2), the DC-DEP force is only dependent on the medium permittivity, the particle size and the electric field. Although we used different electrolyte solution other than DI water, their concentration is very low (10^{-3} M). Therefore their permittivity does not differ much from that of DI water, whereas the zeta potential is sensitive to the fluid property, such as ionic concentration. The zeta potentials in these three kinds of liquids are different. That is the reason why the changed fluid may change the electrophoretic mobility but hardly changes the DEP force. A similar phenomenon was reported by Lapizco-Encinas *et al*. (Lapizco-Encinas, 2004) in a study on the trapping characteristics of biological cells over a range of liquid electrical conductivity.

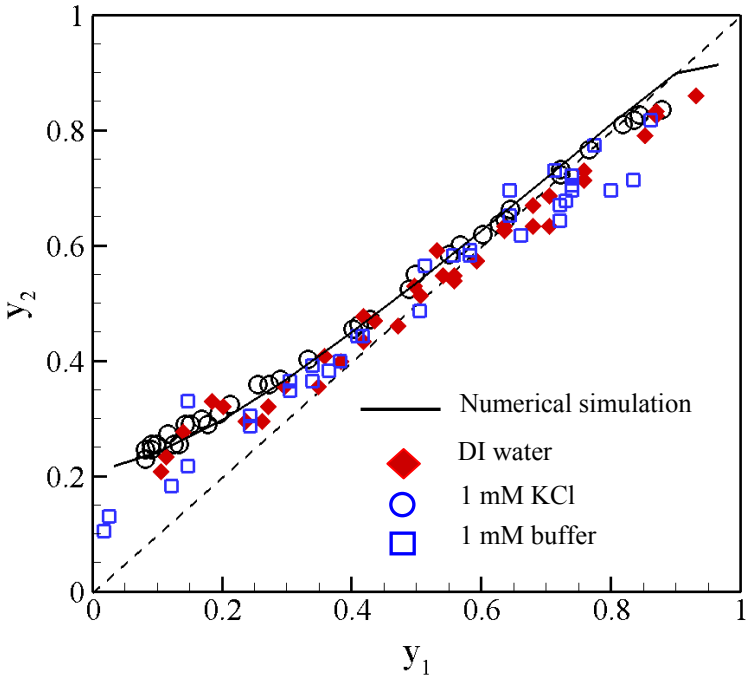

Figure 3-6 Study of the liquid property effect under three different working solutions. Particle size *a* = 2.85 μm, electric field strength E = 20 kV/m, gap width is 60 μm. Solid line is for the numerical prediction based on the buffer solution.

Particle behavior at high electric field

As shown in Fig. 3-1, the electric-field strength is greater at the gap region, so that the direction of the DEP force is against the flow direction near the entrance of the gap. At moderate electric-field strengths, the Stokes drag force is dominant. Thus particle can pass the block region in spite of the resistive DEP force at the entrance of the gap. However, when the electric field strength is above a critical value, the magnitude of the DEP force becomes so large that the particle cannot pass the block. This trapping phenomenon under high electric field has been observed in the experiment. Fig. 3-7 shows the consecutive images of a 15.7 μm particle which is trapped before the block at

electric field strength 89 kV/m. It is very interesting that the trapped particles formed a straight chain, which is a typical phenomenon observed in many DEP experiments. This phenomenon is originated from the particle–particle interaction (Ying et al, 2004; Jones, 1995), which is beyond the discussion of the present work.

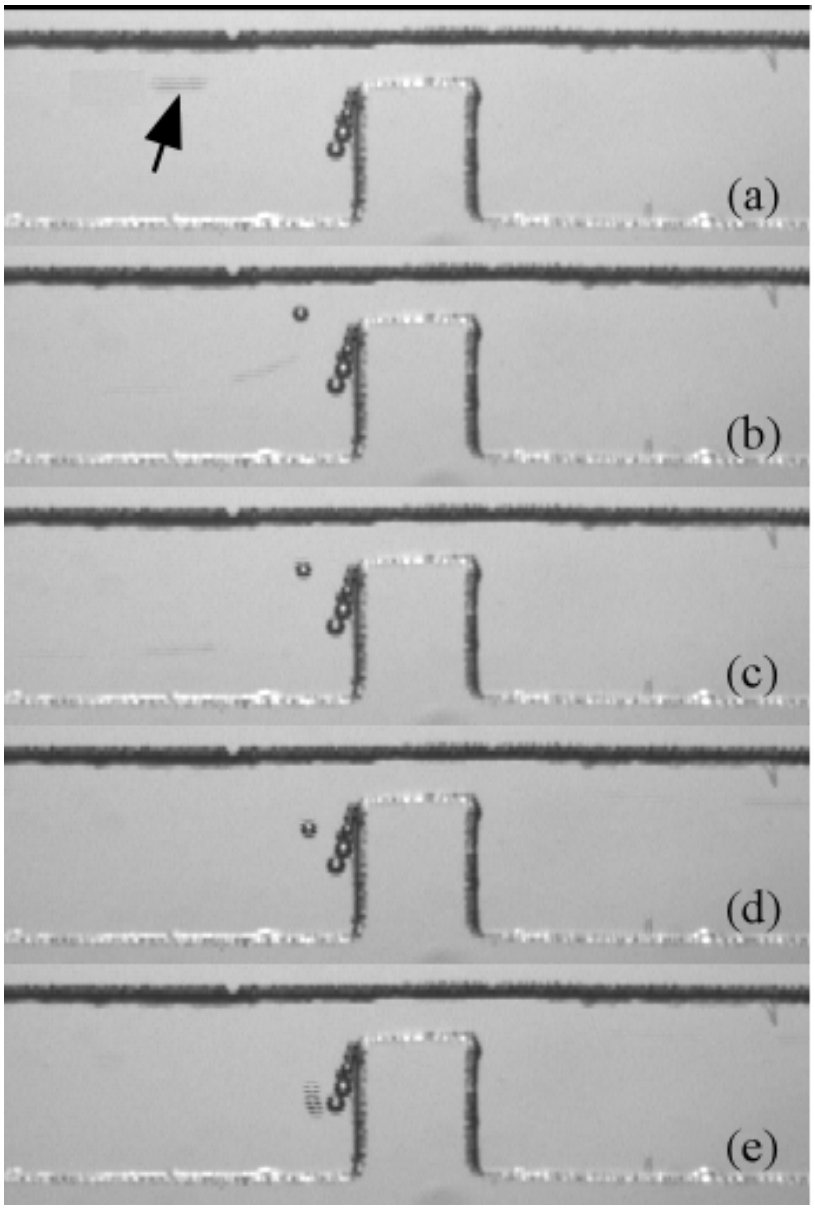

Figure 3-7 Particle trapping at high electric-field strength at E = 89 kV/m. Time difference between the frames is 0.3 second.

Electrolysis problem

In dielectrophoresis experiments, the bubble formation at the electrode can be a cumbersome problem and it usually limits the increase of electric-field strength. In our typical experimental conditions (5 kV/m < E < 20 kV/m), any bubble formation at the electrode surface was not observed. But, at very high electric field, we could observe some bubbles generated on the surface of the electrodes. In our experiment, however, the platinum electrodes were not embedded inside the channel, and instead, the electrodes were placed at the reservoirs that are both open to air. Consequently, even if there is bubble formation at electrodes, the bubbles may float up and the bubbles have little chance to enter the channel region. In practice, we have never observed a bubble entering the channel under all the experimental conditions. Actually, it is one of the benefits using insulating hurdles to generate the dielectrophoretic force, with placing the electrode outside the channel. As a result, under the same conditions to the conventional DEP method in which the electrodes are embedded inside the channel, the present method can utilize the higher electric-field strength with less worrying about the electrolysis problem.

Summary

This chapter demonstrates that the particle trajectory can be controlled by the DEP force created in the non-uniform electric field formed around insulating obstacles in a microchannel. The method relies on the fact that the DEP force is dependent on the particle size and the non-uniformity of the electric field. The geometry and arrangement of the block can be designed and optimized to satisfy the specific requirements in various applications, such as the particle separation and focusing. It is also observed that the

particle trajectory near the wall can be significantly affected by particle–wall dielectric interaction. The motion and trajectory of a particle is simulated by the Lagrangian tracking method. The predicted particle trajectory is in a reasonable agreement with the experimental result, with a correction to the DEP force to account for the finite-size effect and particle-wall interaction.

Appendix

Repulsive Force Due to Particle-Wall Dielectric Interaction

When the particle moves close to the channel wall, there exists a strong dielectric interaction between the particle and wall, resulting in a repulsive force. The magnitude of the repulsive force can be obtained by analyzing the local electric field around a particle close to a wall and integrating the Maxwell stress tensor on the particle surface. The detailed procedure is provided in the appendix. Only the numerical fitted expression is given as

$$\mathbf{F}_{\mathrm{w}} = 0.705\exp[-2.687(\gamma/a)]\varepsilon_f a^2 E^2 . \tag{3.14}$$

The direction of the force is always towards the liquid region from the wall, thus it is understood as wall-repulsion force. Eq. (3.8) is revised as

$$\mathbf{F}_{app} = \mathbf{F}_{EP} + \mathbf{F}_{DEP} + \mathbf{F}_{w} \tag{3.15}$$

Substituting Eqs. (3.9, 3.10, 3.14, and 3.15) into Eq. (3.7), we obtain the particle velocity

$$\mathbf{u}_p = \mathbf{u} - \mu_p \mathbf{E} - \frac{c\varepsilon_f a^2}{3\mu}(\mathbf{E}\cdot\nabla)\mathbf{E} + \frac{\mathbf{F}_w}{6\pi\mu a}, \tag{3.16}$$

The dielectric interaction studied here is different from the EDL interaction which only occurs when the separation distance γ is in the order of nanometer. To consider the

particle–wall interaction, we separately analyzed the static electric field around a stationary particle that is placed near a channel wall. For this purpose, we numerically solved the Laplace equation for a rectangular domain in which a non-conducting spherical particle of radius a is suspended near a wall. The dimension of the rectangle in x-, y-, and z-direction (i.e., length, height, and width) are chosen to be $20a$, $4a$, and $6a$. The width and height of the rectangle are chosen to simulate the experimental condition. The particle is placed at the center of the rectangle in x- and z-direction. The electric field is applied in parallel to x-direction. The separation distance γ in y-direction varies from $0.05a$ to $2a$. Since the boundary condition $\mathbf{E}\cdot\mathbf{n}=0$ satisfies on the surface of the non-conducting particle, the Maxwell stress tensor becomes $\mathbf{T}^e = -(1/2)\varepsilon_f E^2\mathbf{I}$ on the particle surface (Pohl, 1978). The magnitude of the force due to the particle–wall interaction is obtained by integrating the Maxwell stress on the particle surface. Fig. 3-8 shows the calculated electrical force acting on the particle. This force directs to the negative y-direction when the particle flows very close to the upper channel wall, such as the case of particle b in Fig. 3-4. The numerically calculated force is fitted to an exponential curve (solid line in Fig. 3-8) by least-square curve-fitting and yields Eq. (3.14).

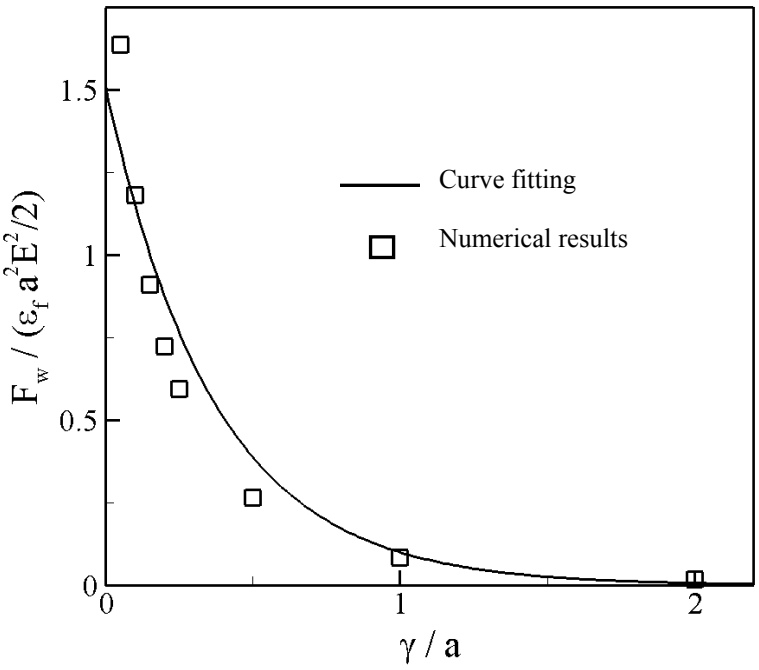

Figure 3-8 Electrical force F_w acting on a spherical particle close to a channel wall.

CHAPTER IV

CONTINUOUS SEPARATION OF MICROPARTICLES AND BIOLOGICAL CELLS BY SIZE WITH DC-DIELECTROPHORESIS

DC-dielectrophoresis (DC-DEP), the induced motion of the dielectric particles in a spatially non-uniform DC electric field, is demonstrated to be a highly efficient method to separate the microparticles or biological cells by size. The locally non-uniform electric field is generated by an insulating block fabricated inside a PDMS microchannel. The particle experiences a negative DEP (accordingly a repulsive force) at the corners of the block where the local electric-field strength is the strongest. Thus the particle deviates from the streamline and the degree of deviation is dependent on the DEP force, which is proportional to the particle's volume. Combined with the electrokinetic flow, mixed polystyrene particles with difference of a few micro meters in diameter can be continuously separated into distinct reservoirs. For separating target particles of a specific size, all required is simply adjusting the voltage outputs of the electrodes. A numerical model based on the Lagrangian tracking method is developed to simulate the particle motion and the results showed a reasonable agreement with the experimental data.

Introduction

Based on the previous investigation in chapter 3, we found that DC-dielectrophoresis could be employed to change the motion trajectory of particles according to their sizes. In this chapter, we further propose a field-flow fractionation method for both DC-DEP particle separation and electrokinetic particle transport

simultaneously in a microchannel. Using the electrokinetic flow in a microchannel network with an insulating block, we show that a mixture of microparticles of two different sizes can be continuously separated into two reservoirs by adjusting the applied voltages at the ends of different branches (Fig. 4-1). The working principle will be described on how the particle trajectory is affected by the DEP force around the hurdle and how the particles are diverted into different branches after the hurdle. Experiments for DC-dielectrophoretic separation of both polystyrene particles and biological cells will be demonstrated respectively.

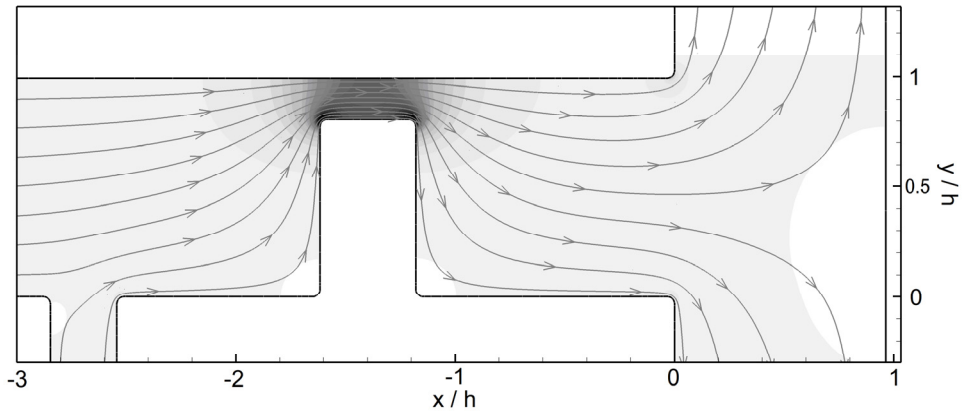

Figure 4-1 Distribution of the electric-field lines and contours of the electric-field strength E around the rectangular hurdle. The darkness level indicates the magnitude of *E*. The x-direction is the channel length (the flow) direction, and the y-direction is the channel width direction. The coordinates are normalized by channel width h.

By the combined effect of electroosmotic flow (EOF) and the electrophoresis (EP), a suspended particle can move along with the fluid and pass through the gap region. The forces that determine particle trajectories include the dielectrophoretic force, the electrophoretic force, and the Stokes frictional force. In addition there is a dynamic

(momentum-associated) component that links the trajectory with particle acceleration, which can be safely neglected because of the particle's micron size. The characteristic time scale for the acceleration phase is about 10^{-4} second, which is of orders of magnitudes smaller than the time scale of the variation of the external forces as well as the time scale of the observation system. The detailed mathematical formulation has been shown in chapter 3. A brief of the operation principle is outlined here. As shown in Fig. 4-2, the electric field has a local maximum at the corner of the hurdle. Since the DC-DEP force directs to the local field minimum (negative DEP), the particle experiences a repulsive force when it moves around the corner of the hurdle. The magnitude of the repulsive DEP force is proportional to the volume of the particle and the local value of $(\mathbf{E}\cdot\nabla)\mathbf{E}$. Therefore a larger particle is subjected to a larger DEP force and tends to be deflected to a stream further away from the corner, in comparison with a smaller particle. The similar DEP deflection occurs when the particle passes the corner on the other side of the hurdle. Similarly, particles moving around a triangular shaped hurdle also experience the DEP repulsion. As a result, the cross-stream trajectory deviation (in y-direction) because of the DEP deflection will be different for particles of different sizes and hence they can be separated into distinct flow streams and further diverted into different channels (Fig. 4-1). We will show in this investigation that by controlling the electroosmotic flow streams after the hurdle, particles or cells of different sizes can be finally diverted into different collecting wells.

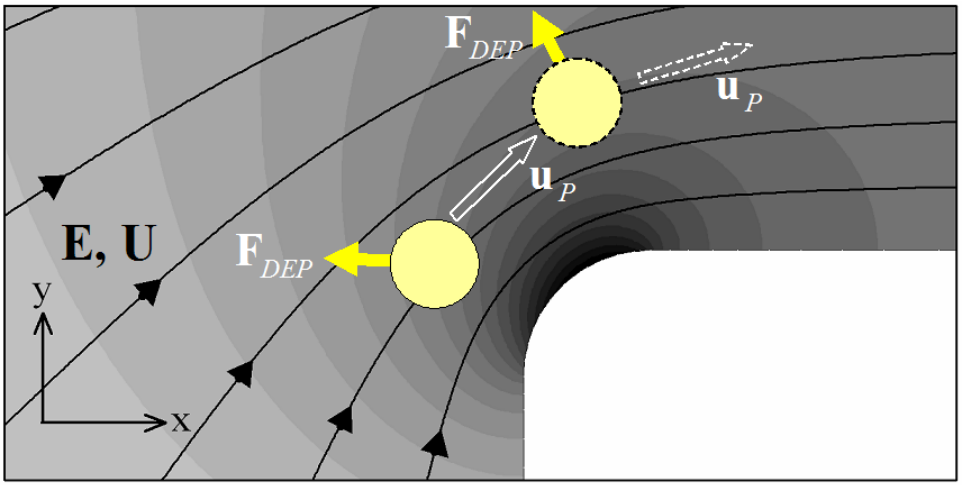

Figure 4-2 DEP force and its effect on a particle near the rectangular hurdle corner. The darkness level indicates the magnitude of the electric-field strength *E*.

Separation of Microparticles

Experiment

The basic design of the separation chip and the specific dimension of the microstructure are shown in Fig. 4-3. There are four branches connected to four different reservoirs. Reservoir B and C are for inputting the particle mixture and the buffer solution, respectively. Reservoir A and D are for collecting the separated small and large particles, respectively. Braches A, C, and D are 300 μm in width. Branch B is 90 μm in width. All of the branch channels are 45 μm in depth (in *z*-direction). The kernel structure is a rectangular block (240 μm × 130 μm) located between the inputting branches (B and C) and the separation branches (A and D). The PDMS (poly-dimethylsiloxane) microchannel was fabricated following the soft lithography protocol as demonstrated in chapter 3.

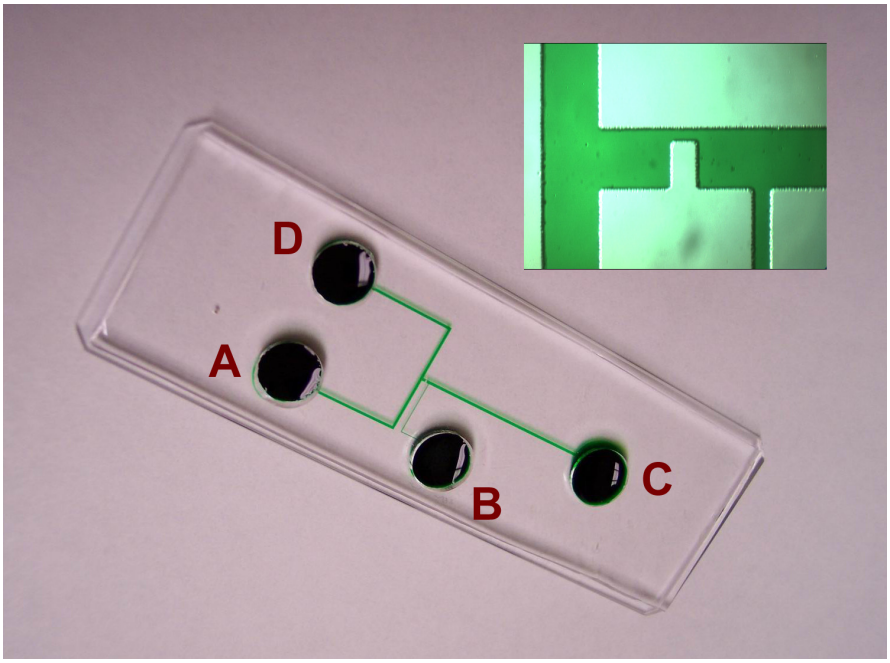

(a)

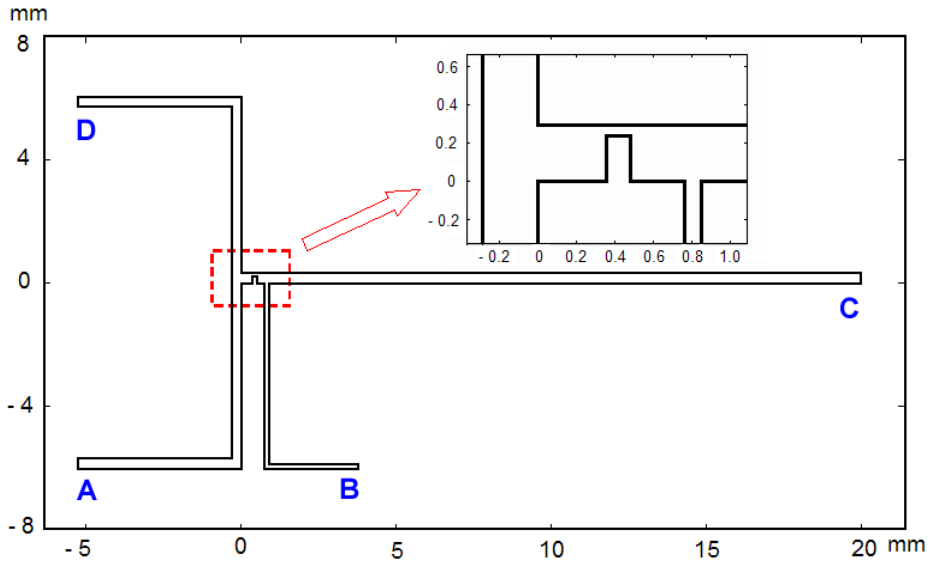

(b)

Figure 4-3 Design of the particle separation chip: (a) Chip design for particle separation; (b) Dimension of the chip and inner structure.

Fluorescent (carboxylate-modified) polystyrene particles of three different sizes, 5.7 μm, 10.35 μm and 15.7 μm in diameter (Bangs Laboratory Inc.) were used as sample particles. These particle sizes are similar to the size of typical biological cells such as the red blood cells and the white blood cells. The particles were supplied in the form of 1% suspension in pure water. These particle solutions were further diluted with the 1 mM sodium carbonate buffer ($Na_2CO_3/NaHCO_3$) solutions. The number density of particle was normally about 10^5/ml. Since the mass density of the particles was slightly greater than that of water (nominal density is 1.05 g/ml), the particle solutions were gently vibrated prior to use to prevent sedimentation.

Before the experiment, the channel and all the reservoirs were primed with the 1 mM sodium carbonate buffer solutions. Then the particle mixture was introduced into reservoir B with a 1-ml plastic syringe. A high-voltage DC power supply (Glassman High Voltage Inc., High Bridge, NJ) was used to drive the fluid flow though the microchannel network by platinum electrodes submerged in each reservoir. A custom-made voltage controller was used to adjust independently the voltage output of each of the four electrodes. In the experiments, electrode D was always grounded. The voltage outputs to electrodes A, B, and C were carefully adjusted to realize that the fluids in the inputting branches B and C always moved to the block and flowed into the separation branches A and D. The pressure-driven flow was minimized by carefully balancing the liquid level in four reservoirs before each experimental run.

The particle motion was monitored by an inverted optical microscope (Nikon Canada Inc.) and recorded by a progressive CCD camera (QImaging, Burnaby, British Columbia, Canada). The camera was operated in video mode at a frame rate of 11.4

frames per seconds. The acquired images (viewed from the top) had a resolution of 640 × 484 pixels. The reading error to determine the particle positions is about ± 2 pixels which correspond to actual dimension of ± 5.4 μm.

Results and discussion

In the numerical simulation, the zeta potential of the PDMS channel wall is set to –80 mV (Ross et al., 2001). The electrophoretic mobility of the 5.7 μm and 15.7 μm particles are fixed as 3.3×10^{-8} $m^2s^{-1}V^{-1}$ and 3.7×10^{-9} $m^2s^{-1}V^{-1}$, respectively, which are based on an independent measurement in a straight channel using the same buffer solution. Because the ionic concentration of the working solution is very low, the liquid properties are of no difference from that of DI water, that is, dynamic viscosity 1.0×10^{-3} kg $m^{-1}s^{-1}$, density 998 kg m^{-3}, and electrical permittivity 6.9×10^{-10} $CV^{-1}m^{-1}$.

Separation by particle size

As discussed previously, the magnitude of the particle trajectory deviation is proportional to the DEP force acting on the particle, and hence the particle volume. Therefore the trajectories of the particles of different sizes can be diverted into different streams after they pass the block. A typical case of separation of 5.7 μm particles and 15.7 μm particles is shown in Fig. 4-4(a), which is obtained by superposing a series of consecutive images of the moving particles. Initially the particle mixture comes out as a single stream from the inputting branch B. Then the main stream of the buffer solution from branch C squeezes the mixture and forces the particles to move closely to the block corner. After the particles pass through the gap between the block and the channel wall,

their trajectories are changed. The trajectory deviation for a larger particle is greater than that for a smaller particle because of the different magnitude of the DEP force they experience at the block corners. Thus the single mixture stream is separated into two. By adjusting the voltage at electrode A, the larger particle moves into the separation branch D, while the smaller particle moves into the other separation branch A. Eventually the particle mixture is continuously separated into two different reservoirs. The particles in reservoirs D and A are pure 15.7 μm and 5.7 μm particles, respectively.

The individual trajectory of the particles can be predicted by using the numerical model developed in the previous section. Figure 4-4(b) demonstrates the comparison between the simulation results and the experimental results for the separation of 5.7 μm and 15.7 μm particles. The dotted symbols are digitized positions of the particles based on Fig. 4-4(a). The smooth curves are the simulated trajectories. According to Eq. (3.10), we introduced previously a correction factor c to account for the finite-size effect to the actual DEP force. We found that simulation results can give a close match to most of the experimental results by setting $c = 0.3$ for 5.7 μm particle and $c = 0.4$ for 15.7 μm particle.

In order to show the trajectory deviation is indeed because of the DEP force, we also removed the term $\mathbf{F}_{DEP}$ from Eq. (3.8) and computed the resulting particle trajectories, as shown by the other two curves in Fig. 4-4(b). As anticipated, the particle trajectories before and after the block are symmetrical and apparently there is no deviation at downstream, if there is no DEP effect.

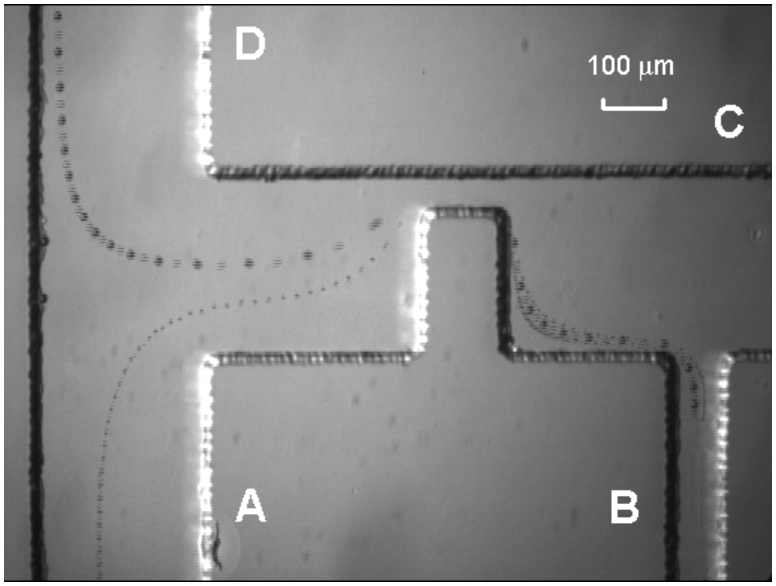

(a)

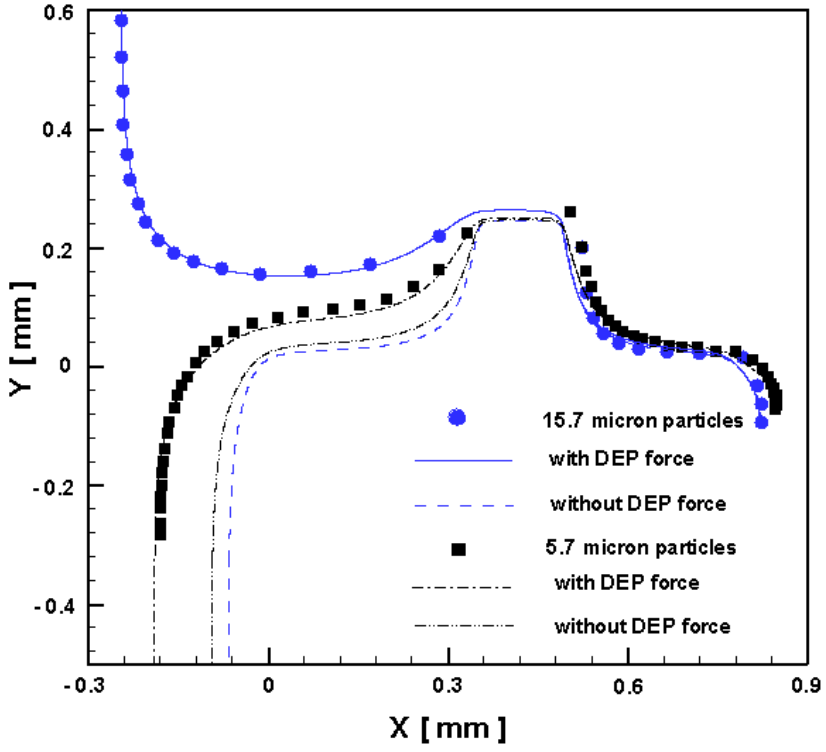

(b)

Figure 4-4 Separation of 5.7 μm and 15.7 μm particles at 500 V voltage level. Applied voltages at different electrodes: V_A = 54 V, V_B = 244 V, V_C = 502 V, V_D = 0 V. (a) Superposed particle trajectories; (b) Comparison of the simulation results and the experimental data.

Table 4-1 Voltages outputs for separation of particles of different sizes. Thee voltage at electrode D is fixed at 0V.

Particle size (μm)		Voltage output at electrodes (Volts)		
I	**II**	**A**	**B**	**C**
		203	280	501
5.7	10.35	305	393	707
		329	503	904
		54	244	502
5.7	15.7	76	344	703
		99	445	909
		95	280	505
10.35	15.7	95	388	699
		124	505	909

Effect of voltage output

The voltage outputs of the four electrodes for different situations are specified in Table 4-1. Since the voltage output of the four electrodes satisfies $V_C > V_B > V_A > V_D$, we define the highest output V_C as the system voltage level. Fig. 4-5 shows the separation of 5.7 μm and 15.7 μm particles at different voltage levels from about 500 volts to 900 volts. Fig. 4-5(a) shows the superposed particle trajectories and Fig. 4-5(b) shows the comparison of the experimental and simulation results. It is demonstrated that the magnitude of trajectory deviation for both larger and smaller particles increases with increasing the voltage level. This is because the DEP force is proportional to the gradient of the electric field intensity, $\nabla|\mathbf{E}|^2$. The other direct effect under the higher voltage level

is that the particle velocity (and hence the separation process) becomes much faster. As shown in Fig. 4-5, at the same frame rate, the distance between consecutive particle positions becomes greater under higher voltage, implying that the particle moving speed becomes faster. This is because the electroosmotic flow is enhanced under a strong electric field. However, we cannot infinitely increase the voltage to speed up the separation process because in the practical application the biological samples are subjected to lyses under too strong electric field. The other possible side effect associated with too high voltage is the Joule heating, which may burn the channel and the biological samples as well.

Other than the voltage level V_C, the voltage output at electrodes A and B are also important to realize the separation. The major function of the electrode B in the inputting reservoir is for driving the particle mixture into the block region. So that V_B should not be very small. Otherwise the electroosmotic flow will be directed to flow back into branch B and the particle mixture cannot be successfully introduced into the channel network. In this experiment, we find it wise to keep V_B around 50% of V_C (Table 4-1).

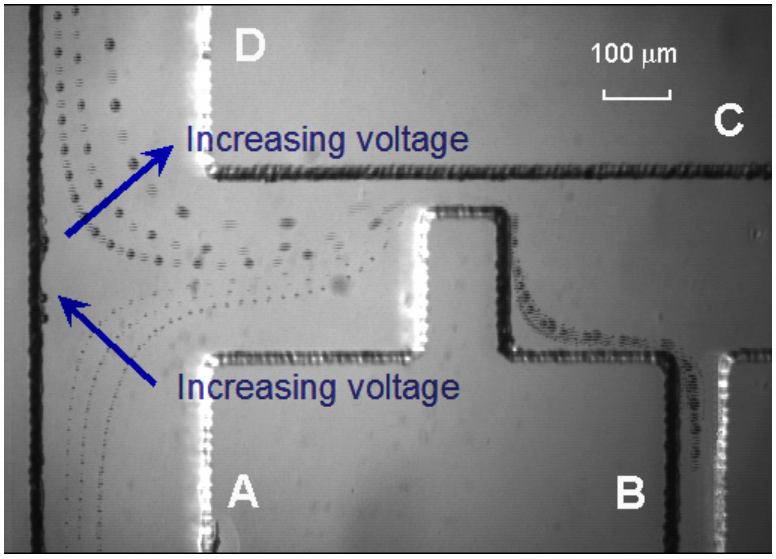

(a)

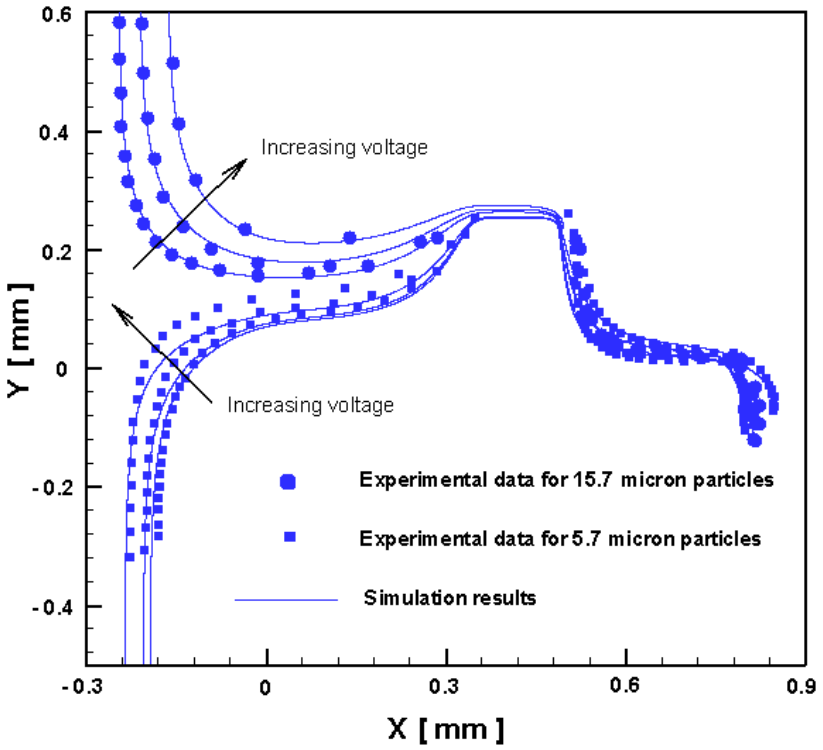

(b)

Figure 4-5 Separation of 5.7 μm and 15.7 μm particles at different voltage levels. Voltage level increases from 500 volts to 900 volts. Applied voltages at different electrodes are specified in Table 4-1. (a) Superposed particle trajectories; (b) Comparison of the simulation results and the experimental data.

The applied voltage at electrode A is for controlling the flow streams and hence the particle motion after the block. According to our numerical simulation, the electric field and the flow field have a similarity and show the same spatial profile. The particles experience strong DEP force near the block corners where the electric field is highly non-uniform. However once the particles move out of the block region, the electric field becomes uniform and there is no DEP force acting on the particles any more. Only the Stokes frictional force and electrophoretic force present. Therefore the particles always move following the streamlines. It has been shown that the single stream of particle mixture is separated into two different streams after the block. In this experiment, it is found that there exists an effective range of V_A in order to realize the separation, which is bounded by two threshold values. As shown by the schematic illustration in Fig. 4-6, when V_A is lower than a threshold voltage 4 V, all of the particles move into branch A (Fig. 4-6a); whereas when V_A is higher than the other threshold voltage 108 V, all of the particles move into branch D (Fig. 4-6c). The effective separation only occurs when V_A falls between these two threshold voltages (Fig. 4-6b). The values of above two threshold voltages are based on the numerical simulation for 5.7 μm and 15.7 μm particles at the voltage level of 500 V. The real values are slightly different in the experiments. It can be reasonably inferred that the threshold voltages are dependent on the channel configuration and the sizes of the particles. They can be easily determined by experimental calibration.

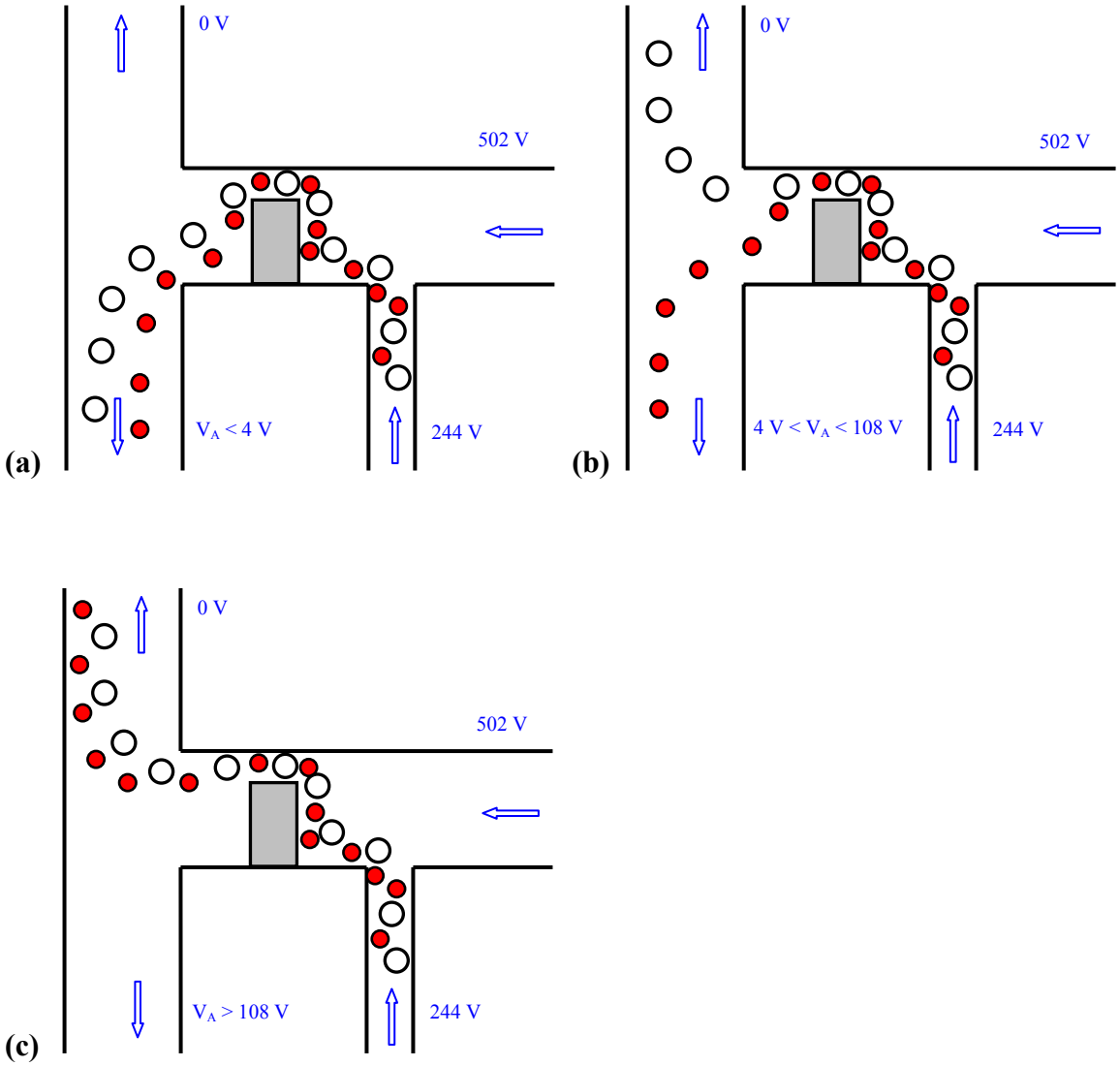

Figure 4-6 Effects of branch voltage V_A on the separation of 5.7 μm and 15.7 μm particles. V_B = 244 V, V_C = 502 V. (a) V_A < 4 V; (b) 4 V < V_A < 108 V; (c) V_A > 108 V.

Sensitivity of the separation

The above observations are all based on the separation of 5.7 μm and 15.7 μm particles. To test the sensitivity of this separation method, we also conducted experiments using particle mixtures of other size combinations, such as 5.7 μm with 10.35 μm, and 10.35 μm with 15.7 μm. By adjusting the voltage output of the electrodes, we

successfully realize the separation of above two particle mixtures using the same channel configuration. The voltage outputs are specified in Table 4-1. This means that the proposed DC-DEP method can separate the particles with different size differences. As one of its major advantages, separating target particles of a different size can be realized simply by adjusting the applied voltages. Channel reconfiguration, such as a new design or modified dimensions, is not required.

Visualization of the fluid flow

Figure 4-7(a) shows the streamlines of the electroosmotic flow near the block region which is obtained by using 1 μm fluorescent polystyrene particles suspended in 1mM sodium carbonate buffer solution. This image was taken by a CCD camera at an exposure time of 4 seconds. It can be seen that fluid from the particle input branch B is squeezed to move closely near the wall of the block by the main flow from the buffer input branch C. This is the purpose of branch C. This design can ensure that the particles move sufficiently near the block corners where they will experience strong DEP force. Thus the particles will have the greatest trajectory changes after they pass the block region.

The electrostatic field and the electroosmotic flow field in the microchannel are simulated using FEMLAB® (Comsol Inc.). The simulated streamlines are shown in Fig.4-7(b). The simulation results fit reasonably well with the experimental results and are used for the subsequent simulation of the particle trajectory.

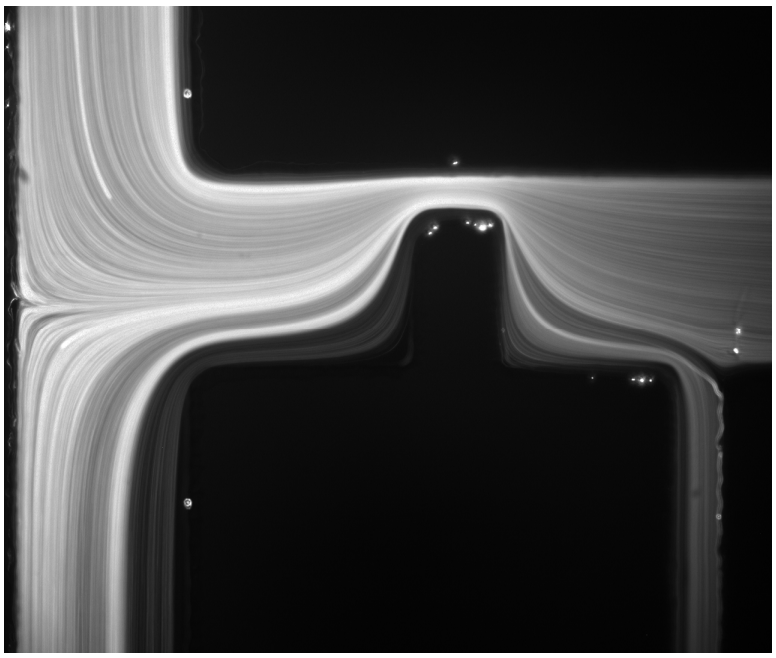

(a)

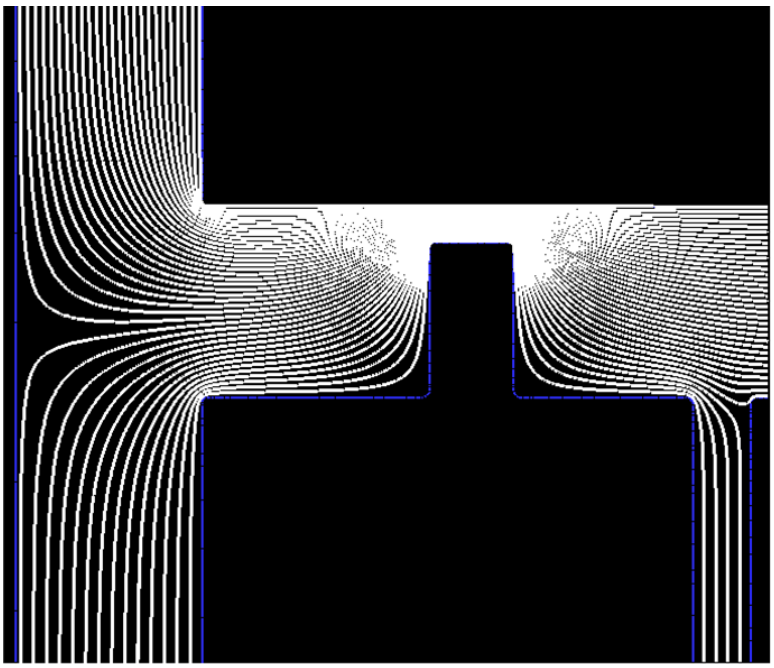

(b)

Figure 4-7 Visualization of the fluid flow (streamlines) in the microchannel. Applied voltages at different electrodes: V_A = 54 V, V_B = 244 V, V_C = 502 V, V_D = 0 V. (a) Experimental result; (b) Simulation result.

Separation of Biological Cells

It is desirable to explore the practical applications of DC-DEP on particle separation. In the previous section, we have proposed a novel method using DC-dielectrophoresis for separation of particles by size and demonstrated that a mixture of polystyrene microparticles of two different sizes can be continuously separated and diverted into two different collecting wells. As a practical application, we will show the continuous separation of biological cells by size using the same principle. First we will describe the experimental design and setup in detail. Finally we will demonstrate the results for separation of human white blood cells and breast cancer cell groups.

Experiment

The design of the DC-DEP separation chip and the specific dimension of the microstructure are shown in Fig. 4-8. There are four branches connected to four different wells. Well B and C are for the cell mixture and the driving buffer solution, respectively. Well A and D are for collecting the separated small and large cells, respectively. Branches A, C, and D are 300 μm in width. Branch B is 90 μm in width. All of the branch channels are 45 μm in depth (in *z*-direction). The kernel structure is a rectangular hurdle (240 μm × 130 μm) or a triangular hurdle (240 μm in base width, 130 μm in height) located between the inputting branches (B and C) and the separation branches (A and D). The PDMS (poly-dimethylsiloxane) microchannel was fabricated following the soft lithography protocol as described in chapter 3.

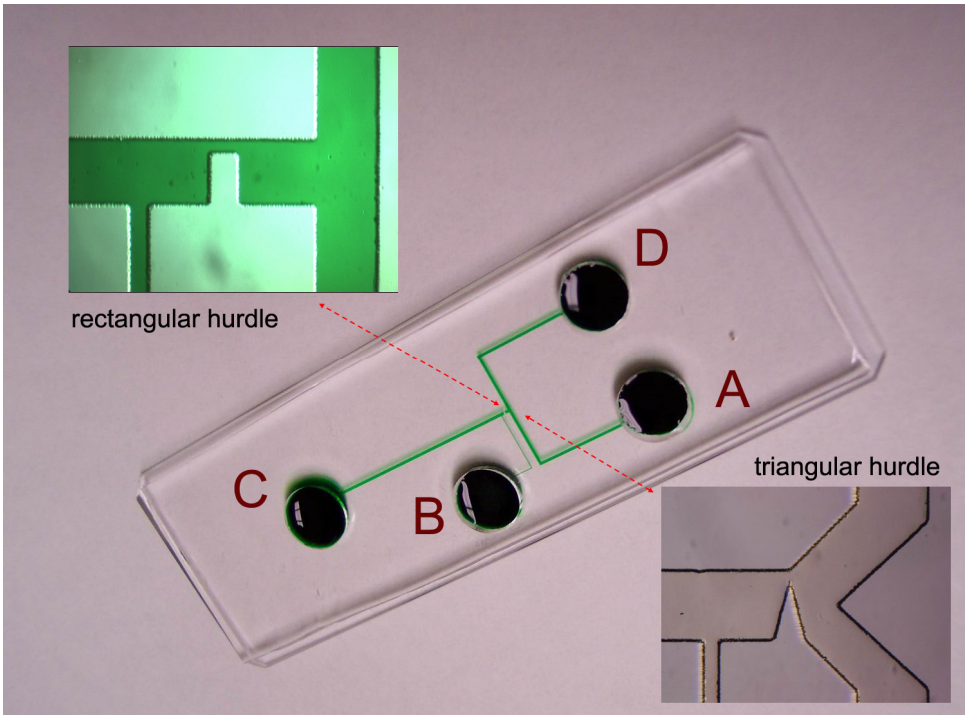

(a)

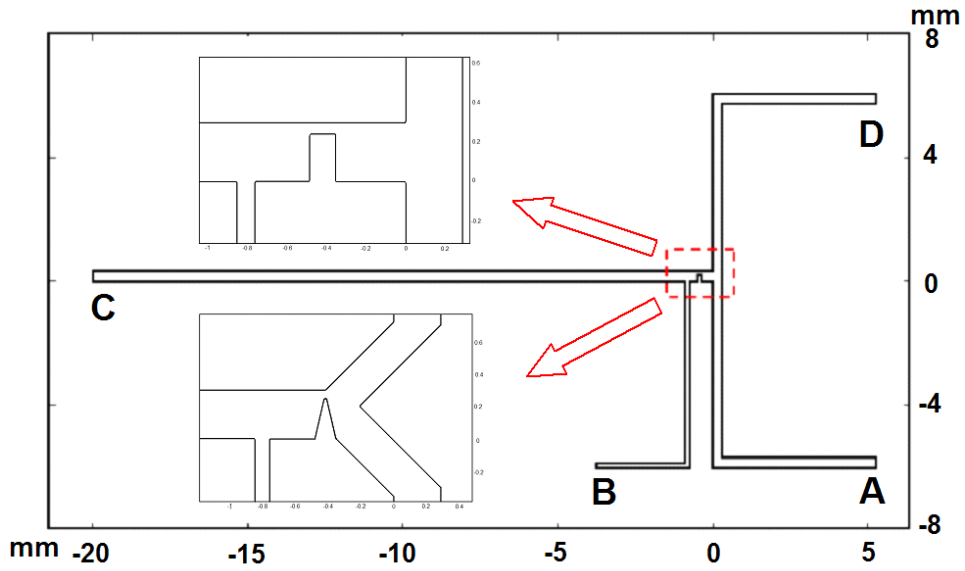

(b)

Figure 4-8 Design of the separation chip. (a) Chip design for cell separation; (b) Dimension of the chip and inner structure.

Fixed white blood cells from an HIV-infected subject and the live mammalian breast cancer cells are used individually in the separation experiments. The white blood cells were fixed and supplied in suspension in a lysis buffer (1x DMEM, Mediatech, #10-013-CV, Herndom, VA). The solution contains white blood cells (granulocytes, monocytes, and lymphocytes) ranging from 8 to 14 μm and other components (platelets, lysed RBC debris, etc) smaller than 5 μm. The cancer cells (cell line MCF7) range from 20 to 60 μm and were supplied in suspension in nutrition solutions (10 mM Tris, pH 7.5, 50 mM NaCl, 250 mM Trehalose, and 0.02% EDTA). The cell concentration was normally about 10^6/ml. Since the mass density of the cells are slightly greater than that of suspension buffer, the cell solutions were well vortexed prior to use to prevent sedimentation.

In standard protocols for preparation of the nutrition solutions, sucrose instead of trehalose is used. However in this study we have tried both sucrose and trehalose, and found that trehalose gives better protection to the cells under application of the electric field. Under the same situation, the destruction of the cells in trehalose is much lower than in sucrose. This is in accord with the finding by Haritou et al. (Haritou et al., 2000). They tried eight different sugar media, including sucrose and trehalose, and found that trehalose suppresses the cell destruction (hemolysis) the best, and at the same time it suppresses the cell fusion very well.

Before the experiment, the channel and all the wells were primed with the working buffer (the suspension solutions). Then the cell mixture was introduced into well B with a 1-ml plastic syringe. A high-voltage DC power supply (Glassman High Voltage Inc., High Bridge, NJ) was used to drive the fluid flow through the microchannel network

by platinum electrodes submerged in each well. A custom-made voltage controller was used to adjust individual voltage output of the four electrodes. In the experiments, electrode D was always grounded. The voltage outputs to electrodes A, B, and C were carefully adjusted to ensure that the fluids in the inputting branches B and C always moved towards the hurdle and flowed into the separation branches A and D.

The cell motion was monitored by an inverted optical microscope (Nikon Eclipse TE-2000U) and recorded by a progressive CCD camera (QImaging, Burnaby, British Columbia, Canada). The camera was operated in video mode at a frame rate of 11.4 frames per second. The reading error in determining the particle positions is about ± 2 pixels which correspond to actual dimension of ± 5.4 μm.

Results and discussion

Rectangular hurdle for chemically fixed cells

As discussed above, the magnitude of the cell trajectory deviation is proportional to the DEP force acting on the cell, and hence the cell size. Therefore the trajectories of the cells of different sizes can be diverted into different streams after they pass the hurdle. A typical case of separation of fixed white blood cells is shown in Fig. 4-9, which is obtained by superposing a series of consecutive images of the moving cells. Initially the cell mixture is introduced as a single stream from the inputting branch B. Then the main stream of the buffer solution from branch C pushes the mixture and forces the cells to move closely to the hurdle corner. After the cells pass through the gap between the hurdle and the channel wall, their trajectories changed. The trajectory deviation for a bigger cell

is greater than that for a smaller cell or debris because of the different magnitude of the DEP force they experience at the hurdle corners. Thus the single stream of mixed cells is separated into different streams. By adjusting the voltage at electrode A, all of the cells (greater than 5 μm) move into branch D, while all the debris of the lysed red blood cells and other small components can be moved into branch A (Fig. 4-9a). Using a different value of applied voltage at the electrode A, the bigger white blood cells (greater than 10 μm in diameter) move into the separation branch D, while the smaller cells and debris moves into the other separation branch A (Fig. 4-9b). In this way, we can purify the cell mixture by removing the lysis debris, or selectively separate the larger cells from the other mixture components. As one of the major advantages, separating target cells of a different size can be realized simply by adjusting the applied voltages. Channel reconfiguration, such as a new design or modified dimensions, is not required.

The highest applied voltage is at electrode C, which determines the overall voltage level of the chip. As pointed out in the previous chapter, maintaining an appropriate voltage level is important to have a high separation speed by enhancing the EOF while avoiding the undesired heating problem. Other than the voltage level V_C, the voltage output at electrodes A and B are also important to realize the cell separation by size. The applied voltage at electrode A is for controlling the downstream flow streams and hence the cell motion after the hurdle. In this experiment, there exists an effective threshold value of V_A in order to realize the separation, depending on the specific separation size requirement. For instance, the effective voltage V_A is about 62 V if one needs to separate cells bigger than 10 μm (Fig. 4-9b); and V_A is about 102 V if one needs to remove the debris (particles smaller than 5 μm) from the mixture (Fig. 4-9a). The

threshold voltages are dependent on the channel configuration and the cell size. They can be easily determined by experimental calibration. The major function of the electrode B in the inputting well is for driving the cell mixture into the hurdle region.

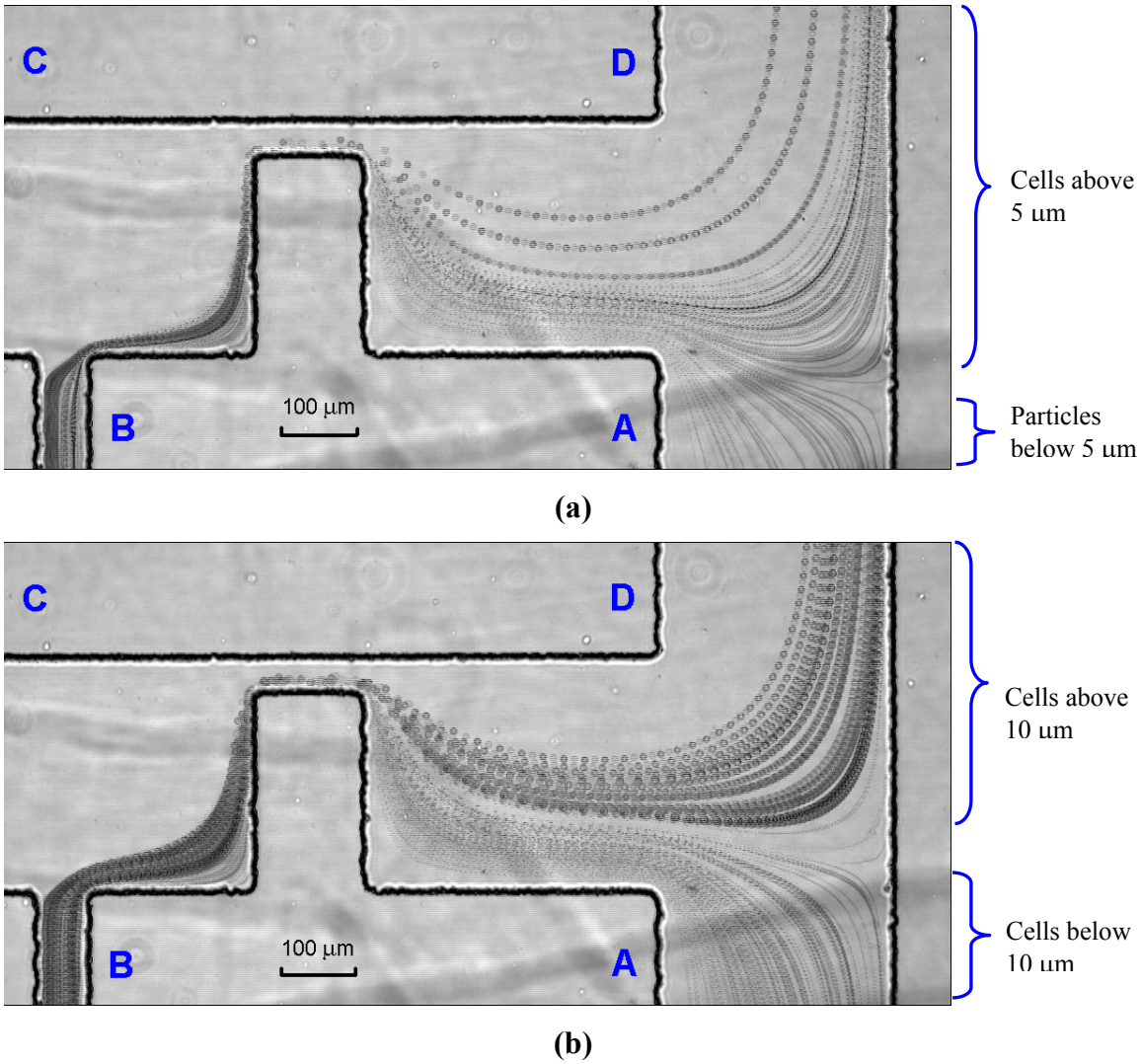

Figure 4-9 Separation of the white blood cells using rectangular hurdle: (a) 5 µm threshold separation, V_A = 102 V, V_B = 191 V, V_C = 343 V, V_D = 0 V, and (b) 10 µm threshold separation, V_A = 62 V, V_B = 191 V, V_C = 343 V, V_D = 0 V.

Improved design: Triangular hurdle for live cells

The above design of rectangular hurdle is for separation of the white blood cells, which have been fixed and thus can withstand the strong local electric field for a longer period of time. However, when dealing with the live cells, such as the breast cancer cells used in this study, the narrow constriction gap region between the rectangular hurdle and the channel wall is so long that the live cells passing through it will die. This is because of the extra stress acting on the cell membrane and the induced Joule heating by the strong local electric field. To minimize the negative effects we modified the design and created a triangular hurdle (the bottom inset in Fig. 4-8a). In this way, the length of the path where the cells experience the greatest stress is greatly reduced. Meanwhile the required DEP force can still be generated around the tip of the triangular hurdle. To further facilitate diverting the cell streams, we also designed divergent output branches downstream after the hurdle.

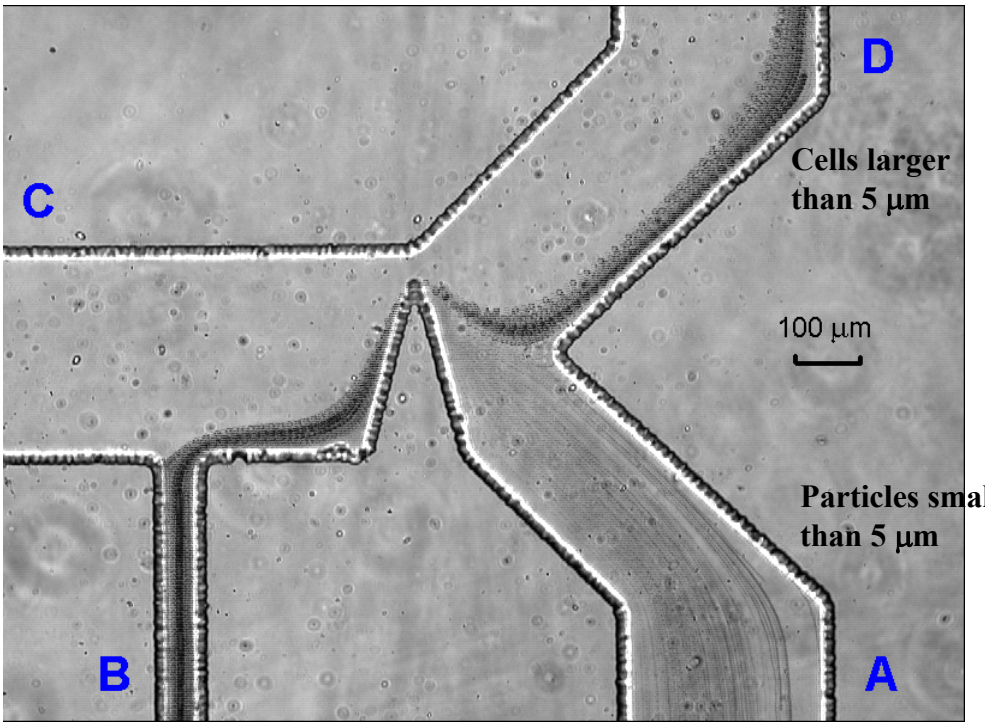

(a)

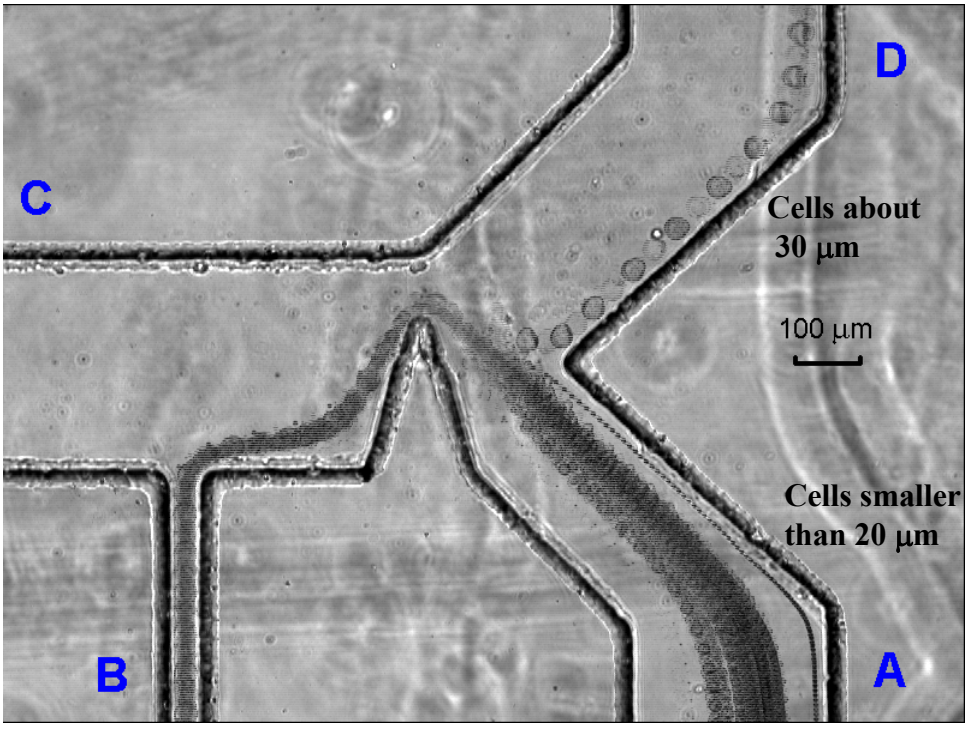

(b)

Figure 4-10 Separation of cells using triangular hurdle with divergent output branches: (a) separation of the white blood cells. V_A = 31 V, V_B = 136 V, V_C = 345 V, V_D = 0 V; (b) separation of the large and small breast cancer cells, V_A = 56 V, V_B = 154 V, V_C = 180 V, V_D = 0 V.

Fig. 4-10a shows the separation of the white blood cells (greater than 5 μm) from the debris. It can be seen that the triangular hurdle works well in terms of separation compared with the rectangular hurdle design (Fig. 4-9). Furthermore the divergent output branches actually eliminate the stagnant flow area (at the cross of the T-shaped output branches in Fig. 4-9) created in the previous design, and avoid the problem of slowly moving cells getting stuck in the stagnant region. Fig. 4-10b shows the separation of the large breast cancer cells (about 30 μm) from smaller ones (about 20 μm). Such large cells are thought to represent a subset of mammary stem cells. They constitute a very small portion (less than 1%) of the whole breast cell population. Large breast stem cells are therefore very rare, and this is illustrated in Fig. 4-10b where only one large cell could be detected. The objective of this separation is to isolate stem cells for cell culture and subsequent analyses. To keep them alive after separation, we have to use much lower voltage level (V_C = 180V, Fig. 4-10b) compared with that (V_C = 345V, Fig. 4-10a) for fixed cells.

Summary

A novel technique using DC-dielectrophoresis is developed to separate polystyrene microparticles and biological particles by their sizes. A DC electric field can be used to perform both the DEP particle separation and the electrokinetic particle transport simultaneously. The kernel structure is an insulating block between the input and separation branches, which can generate a local non-uniform electric field. The particle trajectories are deflected by the DEP force around the block and large and small particles are diverted into different streams. By adjusting the applied voltages at the ends

of different branches, a mixture of microparticles of two different sizes can be continuously separated into two reservoirs.

This separation method has a high sensitivity that particles of a few micro meters difference in diameter can be successfully separated. It is found that the separation speed becomes faster at higher voltage level. There exist two threshold separation voltages which are dependent on the particle size and channel configuration; they can be easily determined by experimental calibration. A numerical model based on the Lagrangian tracking method is developed to simulate the particle trajectories and the results shows reasonable agreement with the experimental observation. The major advantages of this DC-DEP separation are: 1) It can be easily fabricated because the channel geometry is very simple, and there are no imbedded microelectrodes inside the channel. 2) The separation is highly efficient and promises high purity of the final samples. 3) Separating target particles/cells of a different size does not require a new channel configuration or modified dimensions. All required is simply adjusting the applied voltage via the electrodes.

CHAPTER V

CONTINUOUS PARTICLE SEPARATION WITH LOCALIZED AC-DIELECTROPHORESIS USING EMBEDDED ELECTRODES AND AN INSULATING HURDLE

This chapter reports a microfluidics-based lab-on-a-chip device combining the alternating current (AC) dielectrophoresis (DEP) and pressure-driven flow for separation of particle/cell mixtures. The dielectrophoretic separation is achieved by a hybrid design using a PDMS (poly-dimethylsiloxane) hurdle and a pair of embedded metal electrodes to generate localized non-uniform AC electric field. Since the particles and the cells are transported through the small DEP separation region, the negative effects associated with Joule heating and exposure to the electric field have been significantly reduced. Mixtures of polystyrene particles of different sizes and yeast cells with polystyrene particles were successfully separated at AC electric field of 200 kHz.

Introduction

In order to generate DEP, it requires generating a non-uniform electrical field in microfluidic chips. To do so in terms of the design and fabrication, there are two major types of approaches. The conventional method fabricates an array of micro-electrodes embedded in the microchannel network by photolithographic deposition of metals. Another approach constructs local constricted region by obstructions or hurdles that are made of insulating materials. These two methods are both advantageous in certain aspects. The embedded electrode based DEP requires significantly low voltage, avoids global

electrokinetic flow, and renders more flexible manipulation of the particles in a confined area. In contrast the insulating material based DEP requires simpler and less expensive fabrication, avoids the gas evolution inside the channel due to electrolysis, and provides chemically inert platform for handling various biocompatible fluids. The unique characteristics of above two methods sometimes can work in complement to each other dependent on the specific requirements of the application.

In the DC-DEP separation of biological cells presented in chapter 4, we found there were certain negative effects associated with the insulating hurdle based DEP, i.e., the Joule heating of the buffer solution (Cetin and Li, 2008) and the electric field induced membrane stress to the cells. Both of these negative effects were caused by the global electric field present in the conductive buffer over the whole channel, as discussed in chapter II. It is desirable to optimize the chip design to generate reasonable DEP force while minimizing the Joule heating of the buffer solution and the field-exposure of the cell.

Inspired by the previous findings, a hybrid design is proposed in this study for AC dielectrophoretic separation of microparticles by using localized non-uniform electric field, which is generated by a pair of embedded electrodes and an insulating PDMS hurdle. In this design the liquid flow inside the microchannel is driven by hydraulic pressure. The AC electric field is confined within a small area around the PDMS hurdle. As the particles and cells are exposed to the electric field only when they move through this localized DEP separation region, the negative effects associated with the Joule heating and the field-exposure can be significantly reduced.

Experiment

System setup and chip fabrication

The design of the AC-DEP separation chip and the specific dimension of the microstructure are shown in Fig. 5-1. There are four branches connected to four different reservoirs. Reservoirs A and B are for the particle/cell mixture and the driving buffer solution, respectively. Reservoirs C and D are for collecting the separated small and large particles/cells, respectively. Branches B, C, and D are 200 μm in width. Branch A is 90 μm in width. All of the branch channels are 20 μm in depth (in *z*-direction). The kernel structure is a rectangular hurdle (180 μm × 90 μm) located between the input branches (A and B) and the separation branches (C and D). The width of the gap between the hurdle and the wall is 20 μm. The embedded copper electrode has a dimension of 6 mm (length) × 1 mm (width) ×25 μm (thickness). The PDMS microfluidic chip was fabricated on a glass substrate (24×60×3 mm^3, VWR International) following soft lithography protocol. The master for rapid prototyping of the PDMS microstructure was fabricated using negative photo-resist (SU-8 25, MicroChem Co., Newton, MA) on a glass substrate (24×60×3 mm^3, VWR International).

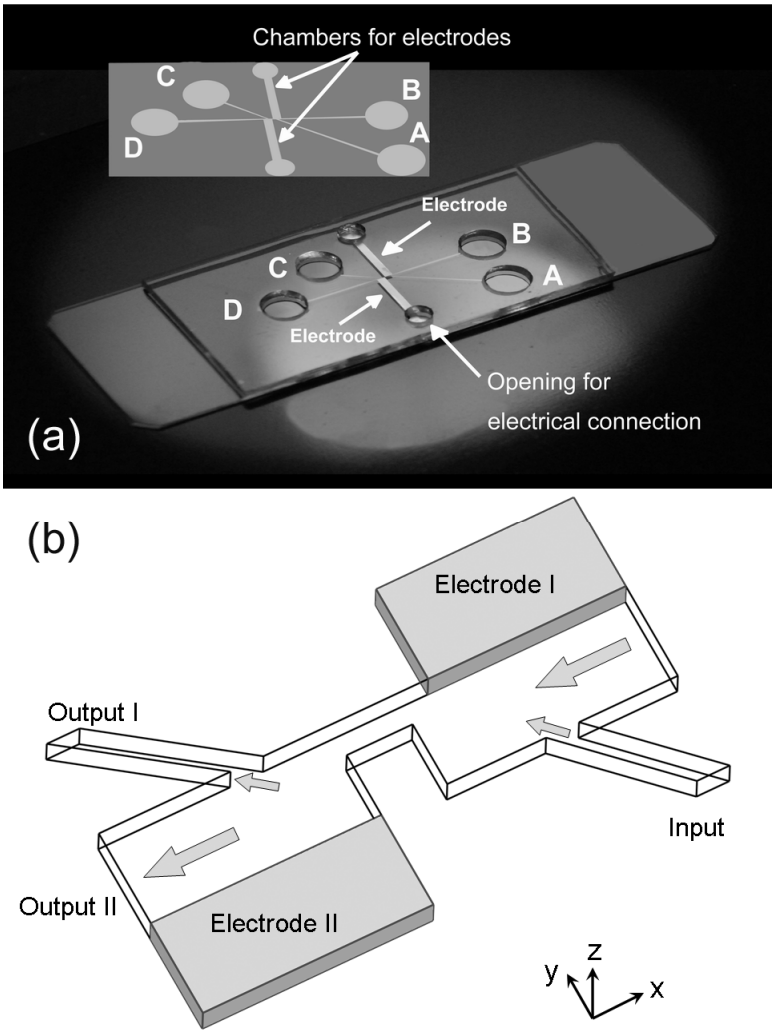

Figure 5-1 Design of the microchip for particle separation using AC-DEP with an insulating hurdle and embedded electrodes: (a) The PDMS microchip is bonded with a glass substrate. The metal electrodes are installed between the PDMS chip and the glass substrate. The inset shows the structure of the fluid conduits with hollow chambers for the electrodes. (b) 3-dimensional schematic illustration of the center structure of the microchip (not to scale).

The fabrication procedure of the micro copper electrodes is extended from the soft lithography. The major procedures are outlined in Fig. 5-2. The copper-clad (laminated with a layer of polyimide, Pyralux AP, Dupont Electronic Materials, Research Triangle Park, NC) was spin-coated with a layer of SU-8 at a speed of 2500 rpm. After the baking

treatment and UV exposure, the unexposed photo-resist was dissolved using the chemical developer (SU-8 developer, MicroChem, Newton, MA). The copper sheet partly covered with exposed photo-resist with desired pattern was submerged in the copper etchant (Ce-100, Transene Inc., Danvers, MA) at 130 ^{o}C until all the un-covered copper was etched. Finally the copper electrodes with desired patterns were released from the sandwich in a NaOH (30%) bath at 130 ^{o}C for one hour to remove the polyimide substrate and the photo-resist. The copper electrodes were inserted into the PDMS chambers manually under the microscope. The PDMS slab with electrodes was plasma treated and bonded with a glass substrate (24×60×3 mm^3, VWR International) to form the microchannel network with embedded electrodes. Because the thickness of the electrode (25 μm) was slightly greater than the depth of the PDMS electrode chamber (20 μm), the deformable PDMS chamber firmly compressed the electrode between the PDMS slab and the glass substrate. The buffer solution automatically filled and sealed the small gap adjacent to the electrodes due to capillary action. The liquid levels in the opening reservoirs of the electrode chambers were carefully adjusted to eliminate the liquid leaking through the gaps.

The polystyrene particles of 5 μm and 10 μm in diameter (Bangs Laboratories, Fishers, IN) and the mixture of yeast cells and polystyrene particles were used to test the performance of the device. All of the mixtures were re-suspended in 0.75 mM sodium borate buffer at final density of 10^5 /ml. The channel and all the reservoirs were initially primed with the suspending buffer. Then the particle or cell mixture was introduced into reservoir A with a 1-ml plastic syringe. An AC power supply (4040A, B&K Precision, Yorba Linda, CA) was connected with the copper electrodes through platinum wires

submerged in the small openings of the electrode chambers (Fig. 5-1). The fluid flow and sample input were all driven by the pressure difference created by different liquid levels within four different reservoirs, which were carefully adjusted to ensure that the fluids in the input branches A and B always moved towards the hurdle and into the separation branches C and D. The particle/cell motion was monitored by an inverted optical microscope (Nikon Eclipse TE-2000U) and recorded by a progressive CCD camera (Nikon DS-2Mv).

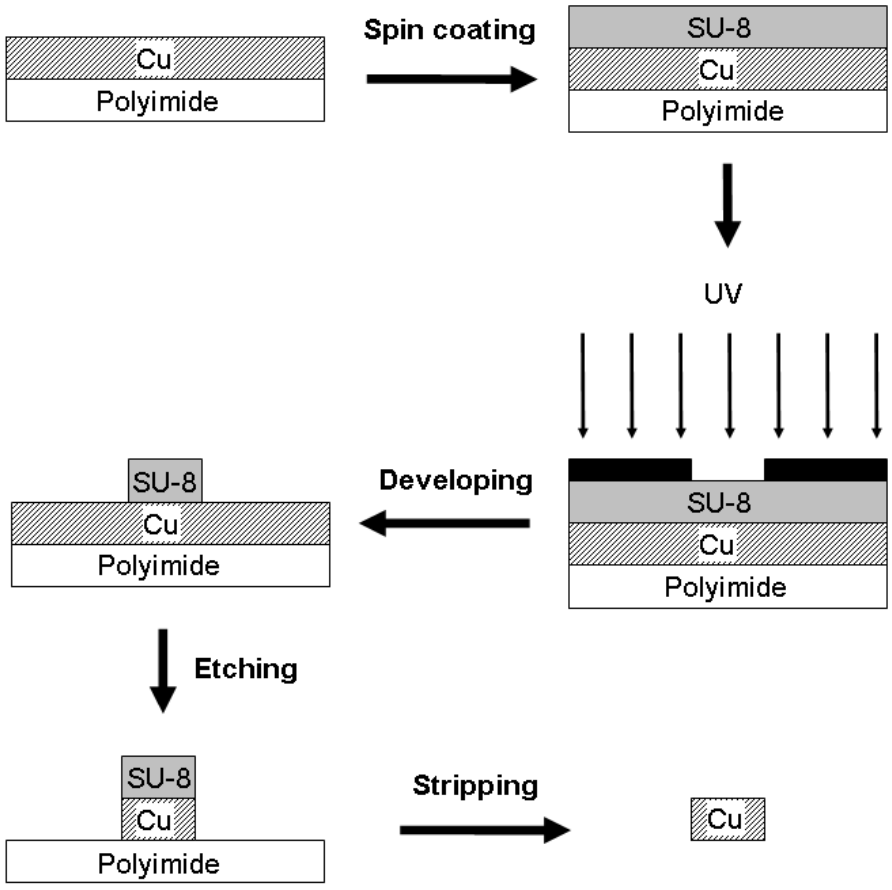

Figure 5-2 Fabrication of the copper (Cu) electrodes by using extended soft-lithography.

Dielectrophoresis-based separation

The mechanism of separating the microparticles in this study is based on the application of the local non-uniform electric field at the specially designed channel constriction. The interaction of the microparticles with the non-uniform AC electric field generates DEP force (as in Eq. (5.6) below) of different magnitude to deviate the particles into distinct streams. This section shows the detailed simulation of the fluid flow, the electric field, the DEP force, and the method of particle tracking.

The flow field in the microchannel is governed by the Navier-Stokes equation

$$\rho\vec{u}\cdot\nabla\vec{u} = -\nabla P + \mu\nabla^2\vec{u} \tag{5.1}$$

with non-slip boundary conditions at the channel wall and with specified pressure values at the reservoirs.

The electric field is governed by the Laplace equation

$$\nabla^2\hat{\phi} = 0 \tag{5.2}$$

with insulating boundary conditions at the channel walls and reservoirs, and with specified electrical potentials at the electrodes. Since AC field is used, $\hat{\phi}$ is the phasor of the applied electrical potential. The actual potential is $\phi(x,t) = \hat{\phi}(x)f(t)$, where $f(t)$ is the functional form of the transient electrical field which is the square wave in this study.

Both the electrical and the flow fields are computed via COMSOL® Multiphysics® by using conductive media and incompressible Navier-Stokes modules, respectively.

In the simulation of particle trajectory, important assumptions are made as follows: (1) the thermo-physical properties of the liquid are constant; (2) the particle and the channel walls are non-porous, and not reacting with the surrounding liquid; (3) the

thickness of the electric double layers next to the channel wall and the particle surface are very small compared to the particle size; (4) the effect of the surface conductance on EDL is negligible; (5) the rotation of the particle does not affect the particle's translation motion; (6) creeping flow (i.e. Re << 1); (7) no thermal effect on flow field and particle velocity.

The particle position $\vec{x}_p$ can be determined, by integrating the particle velocity together with the initial position

$$\vec{x}_p(t) = \vec{x}_0 + \int_0^t \vec{u}_p(\tau)\, d\tau \tag{5.3}$$

where $\vec{x}_0$ is the initial position of the particle, t is the time.

For a fixed frame of reference, the translational motion of a particle is governed by

$$m_p \frac{d\vec{u}_p}{dt} = \vec{F}_{ext} \tag{5.4}$$

where m_p is the particle mass and $\vec{F}_{ext}$ is the net external force.

To simplify the analysis, a simplified model based on Lagrangian tracking method (as shown in chapter 3) is used to predict the particle motion. In this method, only the effect of the flow and the electrical field on the particle is considered, and the effect of the particle on the flow and the electrical field is neglected. Since the particle sizes are small compared to the dimension of the channel, this assumption is acceptable. This assumption is questionable only in the z-direction and in the gap section. However, the separation of the particles depend on the motion in x- and y-direction, therefore the motion in z-direction does not affect the separation performance. To validate this assumption for the gap section, the resultant force which is the result of the local

electrical field is modified to include the effect of the particle size on the local electrical field.

The drag force on a spherical particle is given by

$$\vec{F}_{drag} = 6\pi\mu a(\vec{u} - \vec{u}_p) \tag{5.5}$$

At the creeping-flow limit, which is known as Stoke's law (Leal, 1995), where a is particle radius, $\vec{u}$ is the fluid velocity, $\vec{u}_p$ is the particle velocity.

The DEP force acting on a spherical particle is given by (Jones, 1995)

$$< \vec{F}_{DEP} > = 2\pi a^3 \varepsilon_m \,\mathrm{Re}\left[f_{CM}(\omega)\right] \nabla E_{rms}^2 \tag{5.6}$$

where ε_m is the absolute permittivity of the suspending medium, ∇E_{rms}^2 is the gradient of square of the electric field intensity, E_{rms} is root-mean-square of the electric field. The symbol, < >, represent the time-averaged DEP force. Re[$f_{CM}(\omega)$] is the real part of the Clausius-Mossotti (CM) factor, which is given by

$$f_{CM}(\omega) = \frac{\tilde{\varepsilon}_p - \tilde{\varepsilon}_m}{\tilde{\varepsilon}_p + 2\tilde{\varepsilon}_m} \tag{5.7}$$

where $\tilde{\varepsilon}$ is the complex permittivity and defined as

$$\tilde{\varepsilon} = \varepsilon - j\left(\frac{\sigma}{\omega}\right) \tag{5.8}$$

where ε is the permittivity, σ is the conductivity, ω is the angular frequency of the applied electrical field. Subscripts p and m stand for the particle and the medium, respectively. The particle can experience either positive-DEP which means attraction by electric field intensity maxima; or negative-DEP which means repulsion by electric field intensity maxima, depending on the sign of the f_{CM}. Unlike the DC-DEP which is always negative-

DEP, AC-DEP is also a function of ω and can be either negative-DEP or positive-DEP depending on the electrical properties of the medium and the particle.

The formulation of the expression of the DEP force in Eq. (5.6) is based on the point-dipole model (Jones, 1995). However a real-life particle occupies a finite space and affects the strength of the local electric field. Therefore the actual DEP force acting on a particle is different from the expression in Eq. (5.6). To account for the size effect, a heuristic scaling factor, *c* is introduced in Eq. (5.6) as follows

$$< \vec{F}_{DEP} >= 2\pi c a^3 \varepsilon_m \,\mathrm{Re}\left[f_{CM}(\omega)\right] \nabla E_{rms}^2 \tag{5.9}$$

The scaling factor is assumed to be a constant for a given particle size. Actually the above correction approach has been successfully applied in the authors' previous work on the DC-DEP particle separation (chapter 3 and 4). It was found that the simulated particle trajectory is sensitive to the value of the scaling factors. By setting appropriate scaling factors, the simulation results can give close match to most of the experimental results. Therefore the same approach by using a scaling factor is applied in this study to qualitatively compare the experiment and the simulation and explain the major physics behind the phenomenon.

For the particle size considered in this study, the characteristic time scale of acceleration period of the motion is much smaller than the time scale of the variation of the field variables. Therefore, the acceleration term can be safely neglected, and it can be assumed that the particles move with the terminal speed at all times. Substituting Eqs (5.5) and (5.9) into Eq. (5.4), the particle velocity can be obtained as

$$\vec{u}_p = \vec{u} + \frac{\varepsilon_m c a^2 \,\mathrm{Re}[f_{CM}]}{3\mu} \nabla E_{rms}^2 \tag{5.10}$$

Results and Discussion

Simulation of the electric field and the flow field

Because the ionic concentration of the suspending medium is very low (0.75 mM), the liquid properties are not different from that of DI water, i.e., dynamic viscosity 1.0×10^{-3} kg $m^{-1}s^{-1}$, density 998 kg m^{-3}, and electrical permittivity 6.9×10^{-10} C V^{-1} m^{-1}. The electrical conductivity of the 0.75 mM sodium borate buffer was measured be to 27 mS/m. The electric conductivity of the polystyrene particle (σ_p = 10^{-16} S/m) is significantly lower than that of the medium ($\sigma_m = 27\times10^{-3}$ S/m). The dielectric constant (permittivity) of the polystyrene particle ($\varepsilon_p = 2.3\times10^{-11}$ C V^{-1} m^{-1}) is also much smaller than that of the medium ($\varepsilon_m = 6.9\times10^{-10}$ C V^{-1} m^{-1}). It can be easily inferred from Eqs. (5.7) and (5.8) that the CM factor (f_{CM}) is -0.5 over the wide range of frequency from 0 to 2 MHz. Therefore the particles always experience negative DEP when they pass the hurdle.

Figure 5-3 shows the flow field and the distribution of the electric field strength around the hurdle corner. As expected, the corner regions have the strongest gradient of the AC electric field strength, similar to the results of non-uniform electric field generated by DC voltage (chapter 3 and 4). The channel branch guides the flow to carry the particle mixture through the constriction region for separation and collection in distinct places. Based on the simulation results of the flow and electric fields, the trajectories of the particle motion are computed and will be discussed in the following sections.

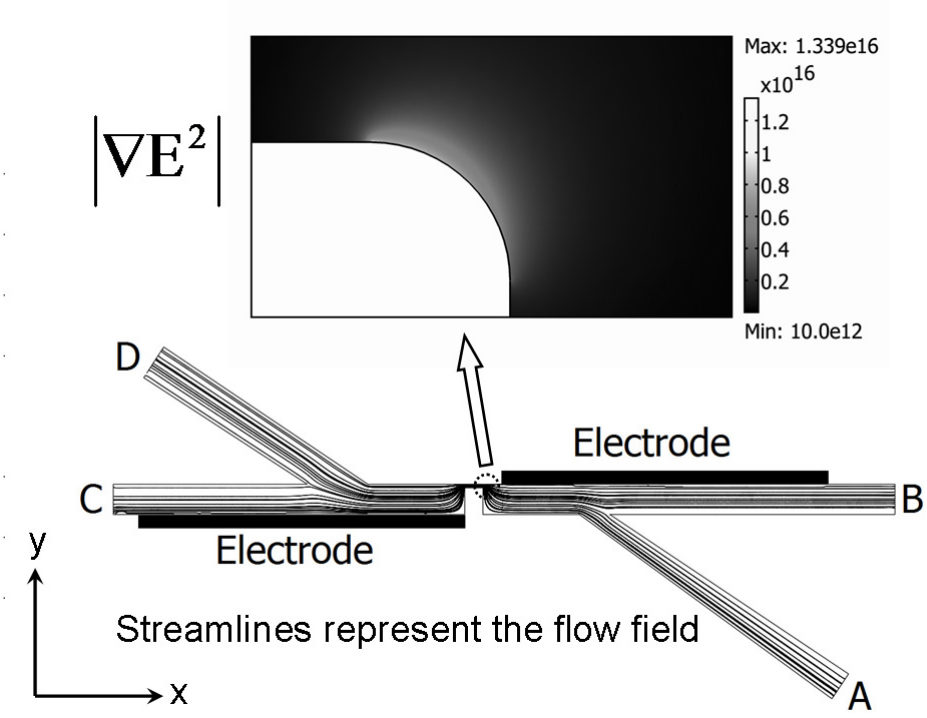

Figure 5-3 Simulation of the flow field and the electric potential field inside the channel. The magnified inset on the top indicates the gradient of the square of the electric field strength, $|\nabla E^2|$. The bottom figure shows the streamlines of the pressure-driven flow inside the channels and the location of the electrodes.

Separation of microparticles by size

Figure 5-4 shows a typical case for separation of 5 μm and 10 μm particles under AC electric field of 7 volts (alternating square waves of 200 kHz). The particle mixture came from the input channel and was squeezed into a thinner stream by the fluid flow from the main channel. Thus the particles were forced to move closely to the hurdle corners where they would experience the strongest AC-DEP force. After they passed the constriction between the channel wall and the rectangular hurdle, the particle trajectories changed because of the AC-DEP force. Since the AC-DEP force is proportional to the particle volume, the larger particles deviated further away from the hurdle corner than

smaller particles. Thus the single mixture stream was separated into two. By carefully adjusting the liquid levels at the collecting reservoirs (C and D) at downstream (hence the pressure distribution), the 10 μm and 5 μm particles were continuously diverted into distinct collecting reservoirs. We also found the separation were effective for a wide frequency range from 100 Hz to 1 MHz. Theoretically the separation should be effective over the complete frequency range because the particles always experience negative DEP. However the Joule heating and electrolysis under lower frequencies caused bubble generation on the electrodes, which could destroy the device. We also avoided using very high frequency above mega hertz because the voltage output decreases significantly at higher frequencies due to the power limit of the AC source.

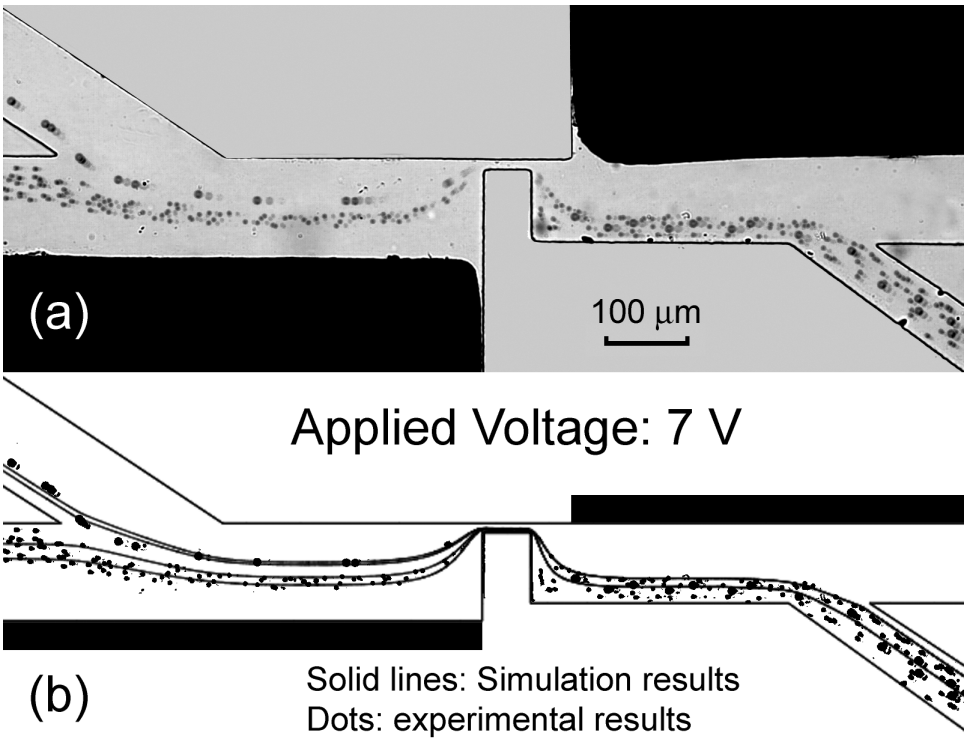

Figure 5-4 Separation of 5 and 10 μm polystyrene particles at 7 V: (a) superposed particle trajectory (b) comparison of the simulation results (solid lines) and the experimental data (dots).

The observed AC-DEP separation can be simulated by the numerical model developed in the previous section. Fig. 5-4b shows the comparison of the simulation and the experimental results. The black dots are the digitized positions of the particles. The solid lines are simulated trajectories. In the simulation, the particle mixture (5 μm and 10 μm) was initially released from two locations at upstream. At downstream the particle trajectories were separated into two due to the AC-DEP, respectively for both of the initial streams. Regardless of the release locations at upstream, 10 μm and 5 μm particle particles always moved into the upper and lower branches at downstream, respectively. For simulation of particle motion, the optimum scaling factors in Eq. (5.9) are 0.7 For 5 μm and 0.5 for 10 μm particles. Theoretically this size-related scaling factor *c* approaches to unity for a sufficiently small particle compared to the length scale of the electric-field gradient in an unbounded domain. However the value of this factor is not solely dependent on the particle size considering the particle-wall interaction in a bounded domain (Chapter III). It is challenging to find out a complete functional dependence of scaling factor on the particle size.

As a control test to verify that the separation was caused solely by the AC dielectrophoresis, the AC electric field was temporally shut down while keeping all the other condition the same. Fig. 5-5 shows the resulting particle trajectories, which demonstrated that the particle mixture kept flowing into one of the downstream branches and there was no obvious separation occurred without application of the AC electric field. However, it can be observed from Fig. 5-5 that the larger particle moves in an upper stream after the hurdle. We believe there are two reasons: 1) the large particles were initially coming at an upper stream than most of the small particles from the input

channel; 2) it may be because of the hydrodynamic pinched flow fractionation (PFF) (Takagi et al, 2005; Zhang et al, 2006; Jain and Posner, 2008). In PFF, the particle stream is pinched to a sidewall at a distance equal to their radius and the particles move along streamlines that passes through their hydrodynamic centers. The different groups of particles move in different streamlines because of their distinct radius sizes. After the pinched section, the flow undergoes a rapid expansion in transverse direction and thus the separation distance between the laminar streamlines is amplified. By adjusting the output flow, the particles laden single stream can be separated into different streams according to the particle size. The channel configuration in the present study created the desired structure for pinched flow fractionation when the electric field was not applied. This is probably the major reason that we observed the large particle moved at the upper stream after the hurdle. However the separation because of PFF was not so obvious in the observation because there was no intentional measure taken to realize the extremely thin pinched flow.

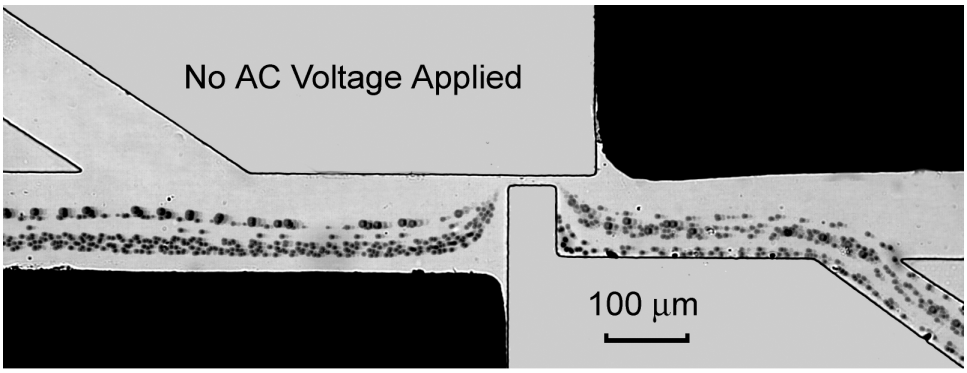

Figure 5-5 Particle trajectories without the applied electric field.

The particle stream separation distance to the channel wall in PFF is proportional to the particle radius (a) (Jain and Posner, 2008). In contrast, from Eq. (5.10), it can be inferred that the particle transverse diversion because of the DEP is proportional to the square of the particle radius (a^2). Therefore, for the fixed particle mixture, the DEP based separation has a resolution at higher order of magnitude. This is the major advantage of the DEP based separation over PFF based separation.

As discussed in the simulation section, the DEP force is proportional to the gradient of the square of the electric field, ∇E_{rms}^2. Therefore when the electric field strength becomes higher, the increased DEP force will push the particle trajectory further away from the hurdle corner. Fig. 5-6 shows the separation under applied electric field of 10 volts. As expected, the particle trajectories for 5 μm and 10 μm particles are all shifted further toward the upper channel wall after the hurdle compared with the separation at 7 volts in Fig. 5-4. This observation is in agreement with the voltage effect reported in electrodeless DC-DEP separation of polystyrene particles (Chapter 4). However, the trajectory elevation was limited by the AC power source, which has a maximum voltage output of 10 volts. In this chip configuration, there was no separation at voltage lower than 7 volts. Therefore the margin for adjustment was only 3 volts.

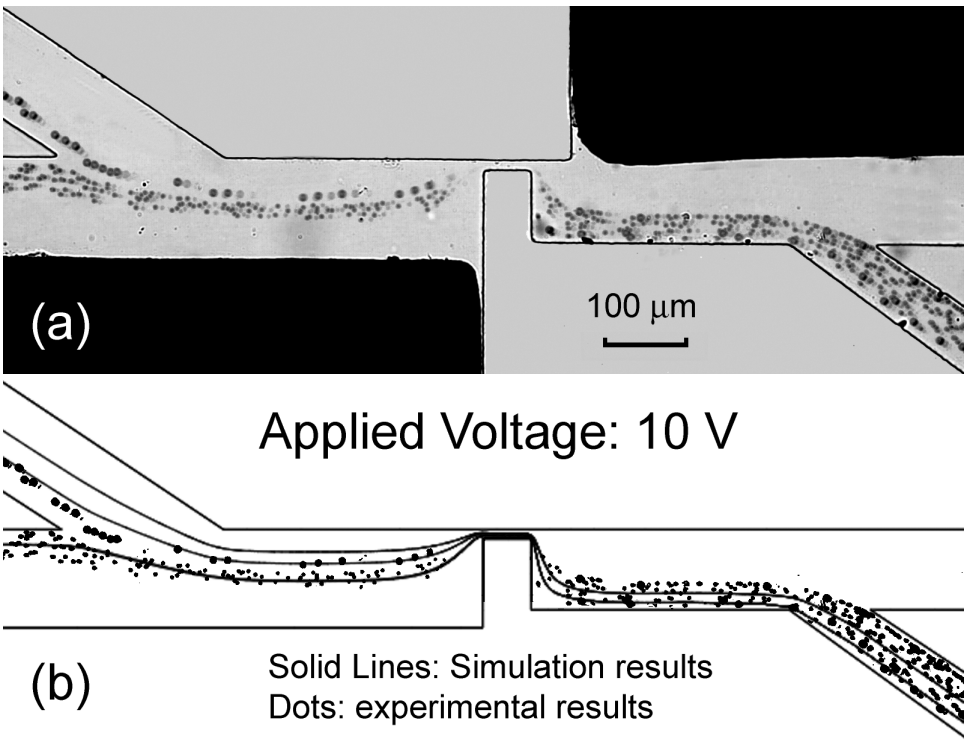

Figure 5-6 Separation of 5 and 10 μm polystyrene particles at 10 V: (a) superposed particle trajectory (b) comparison of the simulation results (solid lines) and the experimental data (dots).

Separations of cells

The localized AC-DEP can also be applied for separation or sorting of biological cells. However the dielectric responses of the cells are much more complicated because of the diverse dielectric properties of the intracellular substances. The cells may show positive or negative DEP (the CM factor could be positive or negative) dependent on the driving frequency. This is different from the case of particles made of non-conducting polystyrene, which show only negative DEP over the complete frequency range (from 0 to 2 MHz). It is also different from the situation under DC dielectrophoresis, when all types of cells show negative DEP because of the shielding effect of the membrane and the electric double layer (Jones, 1995; Gawad et al, 2004). The diverse AC-DEP response

of the cells implies that the cells can be separated according to their different properties rather than solely by size, as reported by the extensive literature (Gascoyne and Vykoukal, 2002; Hughes, 2002; Gonzalez and Remcho, 2005).

In order to test the localized AC-DEP separation is also effective to the cells we tried separation mixed the yeast cells (size ranges from 3 to 5 μm) with 10 μm polystyrene particles. The crossover frequency of the yeast cells is dependent on the medium conductivity (Cruz and García-Diego, 1997). For a fixed medium conductivity, the cells experience negative DEP at below crossover frequency and positive DEP at above crossover frequency. Considering the separation of the yeast cells and the polystyrene particles, it is desirable that the yeast cells experience positive DEP while the particles experiences negative DEP. Theoretically this can be achieved by using much higher frequency than the crossover. However, it was found that the separation was best at frequency about 200 kHz (as shown in Fig. 5-7). The 0.75 mM sodium borate buffer has an electric conductivity of 27 mS/m. We did not find any published data for the crossover frequency of the yeast cells in this specific suspension medium. We estimate that the crossover should be about 200 kHz or even lower because we did not observe obvious negative DEP for the yeast cells. At frequency much higher than 200 kHz, the separation became weak. This was because the voltage output magnitude decreased at higher frequency as discussed previously. Therefore there exists an optimum frequency in this situation. It should be noted that the limit at higher frequency is solely because of the specific AC power source, it has nothing to do with the separation mechanism proposed in this study.

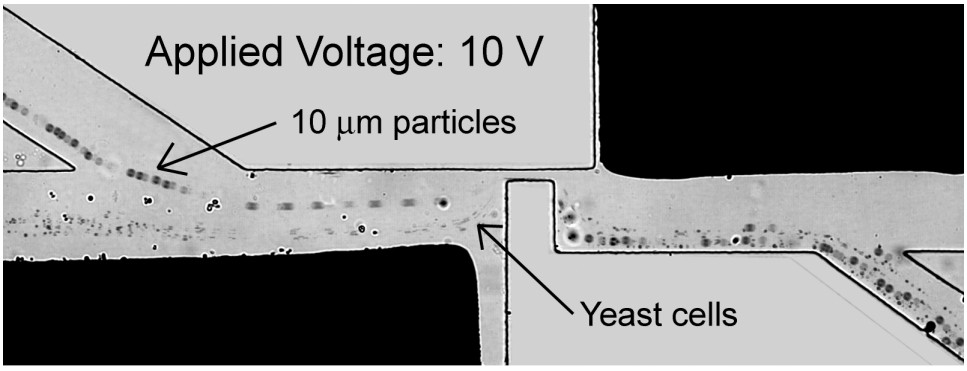

Figure 5-7 Sorting of the yeast cells from a mixture with 10 μm polystyrene particles at 10 V.

Notes to improve the device performance

The explorative work in this study has demonstrated that microparticles can be continuously separated by using localized AC dielectrophoresis in a pressure-driven flow. However there is much to be improved in terms of design and fabrication. From the above experimental results, it was observed that the trajectories of the particles of two different sizes were rather close to each other after the hurdle, which will affect the separation efficiency. If the separation distance of the two trajectories can be further increased at downstream, one may achieve the separation of particles with even smaller size difference, or at lower voltages. For this purpose, it is desirable to design a T-shaped bifurcation channel structure immediately after the hurdle. However, because of the limited fabrication precision for the copper electrodes using extended soft lithography, the copper electrodes occupy a large portion of the channel wall (Figs. 5-4 to 5-7) and thus the bifurcation branches have to be located further away at downstream. If one can make embedded metal electrodes of several microns in width using advanced fabrication methods, it is expected that the separation distance between particle trajectories and hence the separation efficiency will be significantly increased.

System throughput is another important parameter to consider for optimization of the sorting capability of the proposed device. The advantage of pressure-driven flow in this device is that it can be adjusted to increase the flow rate and hence the throughput without causing negative effects, such as Joule heating, associated with electrokinetic flow. However, if the flow rate is too fast, the time period for the particles to pass the DEP separation region becomes extremely short. Thus the separation distance between the separated particle trajectories (of different sizes or dielectric properties) after the hurdle becomes very small, which will reduce the separation efficiency. Therefore there is a trade-off and further investigation is needed to characterize the optimum flow rate for the highest throughput.

Summary

AC dielectrophoretic separation of particle/cell mixtures have been achieved by a hybrid design which generates and confines a localized non-uniform AC electric field within a small area around a PDMS hurdle. As the particles and cells are exposed to the electric field only when they move through this localized DEP separation region, the negative effects associated with the Joule heating and the exposure to electric field have been significantly reduced. Mixtures of polystyrene particles of different sizes and yeast cells with polystyrene particles were successfully separated at AC electric field of 200 kHz. Other than the DEP separation of particles by size, this device could potentially separate the particles/cells with different inner properties.

CHAPTER VI

DETECTION OF BIOLOGICAL PARTICLES USING RESISTIVE PULSE SENSING

This chapter demonstrates an on-chip resistive pulse sensing scheme for detection and enumeration of particles and biological cells. For cell detection and enumeration, this system integrates optical fluorescence detection with resistive pulse sensing enhanced by a metal oxide semiconductor field effect transistor (MOSFET). The MOSFET signal indicates the total number of the cells passing through the detection channel, while the concurrent fluorescence signal records only the number of cells tagged with a specific fluorescent dye. The absolute count of the CD4+ T cells and its percentage to the total lymphocytes can be analyzed by combining the two counting results, which showed comparable accuracy to those from the commercial flow cytometer. Further to improve the sensitivity of the system, symmetric mirror channels are designed with differential amplifications, which significantly reduces the noise and achieves better signal-to-noise ratio. Polystyrene particles of different sizes have been detected with the developed sensing scheme and a record low volume ratio of the particle to the micron-sized sensing channel (0.0004%). This volume ratio is about ten times lower than the lowest volume ratio reported in the literature including that specified for commercial Coulter counters.

Introduction

Coulter-type resistive pulse sensing is a classic methodology of detecting biological particles and reagents, such as cells, microbes, macromolecules, multi-analyte

and other ionic species (Bayley and Martin, 2000; Bayley and Cremer, 2001; Schmidt et al, 2005). The most successful application so far is the Coulter counter device which has been used for decades to count and size small bio-particles and remains a mainstay of the clinical laboratory. Compared with later flow cytometers, such as the FACS (Fluorescence Activated Cell Sorting) system, Coulter counters can realize label-free detection and are of much lower manufacturing and operational cost.

In particle analysis using the Coulter principle, the translocation of a non-conducting particle through an electrolyte-filled small aperture leads to an increase in the resistance, or equivalently, a decrease in the conductance of the aperture. As shown in Fig. 6-1, the frequency and amplitude of the resulting trans-aperture voltage or ionic current modulations provide critical information about the number and size of the particles of interest.

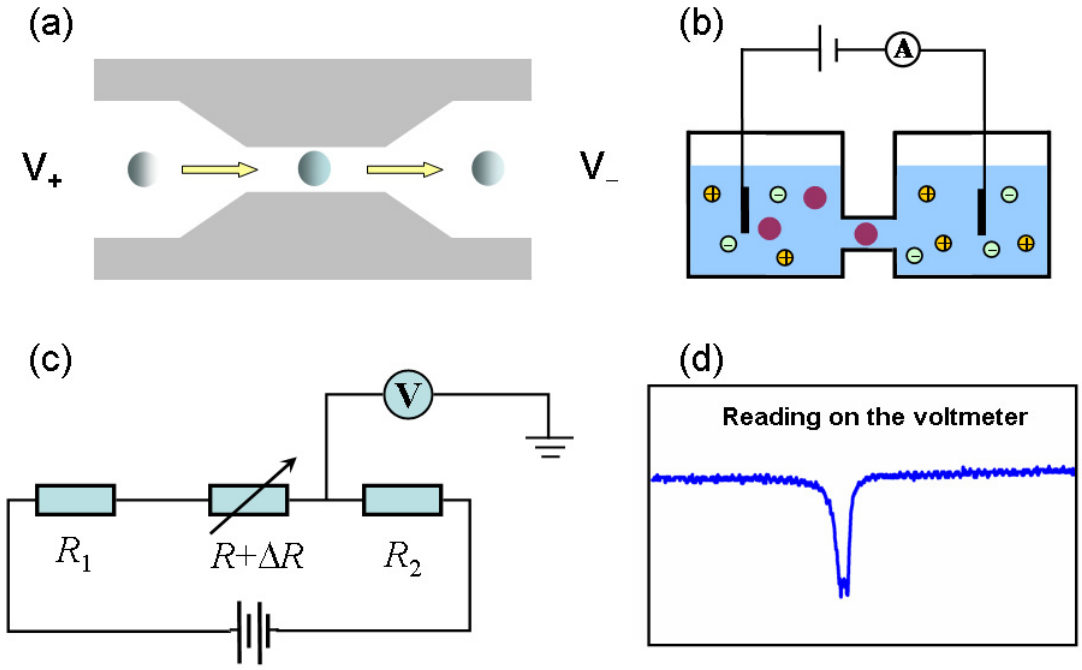

Figure 6-1 Schematics of resistive pulse sensing. (a) when a particle pass a constriction in the microchannel, it changes the resistivity of the constriction area; (b) when an electric voltage is applied the across the channel, the electric current through the system changes due to the presence of the particle; (c) equivalent electronic circuit of the system; alternatively, the presence of the particle can also be sensed by monitoring the trans-aperture voltage drop near the constriction, where the voltmeter shows a pulse (d) due to the transient resistivity change.

With rapid development of microfluidic and nanofluidic technologies, Coulter principle has found extensive applications in advanced biological detection in recent years. A survey of the recent literature on Coulter-type sensors showed two major trends. One is to use nanoscale apertures such as naturally-occurring protein nanopores (Bezrukov et al, 1994; Bezrukov and Vodyanoy, 1995; Kasianowicz et al, 1996) or artificial nanopores (Li et al, 2003; Saleh and Sohn, 2003; Heng et al, 2004; Chang et al, 2004; Heins et al, 2005; Fan et al, 2005; Harrell et al, 2006; Han et al, 2006; Wharton et

al, 2007) to detect biopolymers, such as DNA and proteins. However there are some inherent limitations associated with the naturally-occurring or the synthetic nanopores: 1) fragility and life time of natural biological membranes; 2) more robust artificial nanopores lack the ease of fabrication and pose significant challenges to integration for on-chip devices. There are some efforts underway using hybrid approaches to solve both problems by nanotechnology. The other trend is to use multiple channel networks to improve the system throughput (Jagtiani et al, 2006; Zhe et al, 2007) or to use instrument amplifications and noise reduction from fluid circuit and electronic sensing system to detect small particles inside relatively large microscale apertures that can be easily fabricated using soft lithography (Carbonaro and Sohn, 2005; Xu et al, 2007; Sridhar et al, 2008).

A microfluidic RPS sensing technique was recently reported to detect the translocation of small particles through a relatively large aperture (Xu et al, 2007; Sridhar et al, 2008). The percentage modulation of the trans-aperture voltage disturbance is amplified by a MOSFET (metal oxide semiconductor field effect transistor) and sensed as a MOSFET drain current drop. A minimum volume ratio of 0.006% was achieved, which is ten times more sensitive than those reported in the previous literature. As a real application, in this chapter, we will furbish this system with a fluorescence optical detection function and realized on-chip counting of the total number and the percentage of the fluorescence-labeled CD4+ T cells. To further increase the system sensitivity, another resistive pulse sensing scheme is implemented using a symmetric mirror-channel structure and differential amplifiers. We demonstrate that this unique design can significantly reduce noise through common mode rejection and achieve a better signal-to-

noise ratio. Using a two-stage differential amplification scheme, we detected a minimum volume ratio of 0.0004% (particles of 520 nanometers in diameter inside a sensing aperture of 50×16×20 μm^3), which, to our best knowledge, is 10 times smaller than the current commercial Coulter counter (0.0037%) and similar devices reported in the literature (0.006%) (Xu et al, 2007; Sridhar et al, 2008).

On-Chip Enumeration of CD4+ T Lymphocytes

Background

It has been widely recognized that AIDS is becoming one of the leading epidemic causes of adult deaths globally, especially in developing countries where the prohibitive expenses of the conventional assay technology limits the access for the vast majority of the HIV-infected individuals. Among the most important clinical parameters, enumeration of the peripheral blood CD4+ T lymphocytes is a key factor for determining disease progression and monitoring efficacy of the treatment. A decrease in the total count of CD4+ T lymphocytes, the critical immune cells infected by HIV, is one of the hallmarks of HIV disease. In addition to absolute CD4+ T cell number, the CD4+ percentage (ratio of the CD4+ T cells to the total lymphocytes) is also an important clinical parameter, especially in pediatric HIV infection (Hulgan et al, 2007). Children have higher frequencies of CD4+ T cells and higher total lymphocyte frequencies than adults. Therefore the CD4 percentage provides more accurate prediction for the risk of opportunistic infection than does the absolute CD4 cell number.

Current recommendations for HIV care call for evaluation of CD4+ T cells approximately every 3 months. In the developed world, these evaluations are performed at referenced laboratories. The typical benchtop flow cytometers cost from $75,000 to $125,000 plus an additional 10% annually for maintenance. In addition, the sample volumes are usually in the 100 microliter range, making the estimated cost in reagents per assay $5 ~ $50. There are some limited versions of these instruments designed specifically for T cell subset evaluation. However the reagent costs and technical and operational complexity remain high. There is a desperate need for alternative reliable systems that are both affordable and portable for on-site CD4+ T cell determination at HIV care clinics worldwide, especially in the resource-poor developing countries.

Since the biological reagents and particles, such as blood cells, bacteria, and macromolecules, exist in fluidic natural environment, microfluidics-based lab-on-a-chip devices render excellent platforms for relevant biomedical manipulations and assays. This emerging field is actively approached by scientists from many disciplines and exploited for wide range of applications. However, it is not until recently that this promising technique found applications confronting the AIDS. Rodriguez and colleagues reported a cheap and easy way to count CD4+ cells on a microchip (Rodriguez et al, 2005). Microliter volumes of blood are introduced into a microfiltration chamber where the pre-labeled CD4+ cells are captured and separated from the red blood cells. Digital images of the labeled cells are obtained by fluorescence microscopy and analyzed digitally to determine the absolute counts and percentage of CD4+ T cells. They claimed that their prototype could discriminate clinically CD4+ count thresholds within 15 minutes with high sensitivity and specificity. With cooperation with Toner's group, they

further developed a novel technique, which can capture the unlabeled CD4+ T cells in a microfluidic channel pre-coated with anti-CD4 antibodies (Cheng et al, 2007a,b). The non-specific cells were rinsed from the channel under controlled shear stress and the CD4+ cell count are obtained by enumerating all cells isolated from 10 microliter volume of blood using standard optical microscope. A close correlation between CD4+ cell counts obtained by microchip and those by flow cytometry was observed in the clinically relevant range between 200 and 800 cells per microliter, beyond which their device cell counts were significantly lower than those obtained by flow cytometry. Later they developed another novel detection method using impedance modification to quantify the immobilized CD4+ T cells (Cheng et al, 2007c). These systems are advantageous in that they can directly handle minute amount of whole blood, minimize or eliminate the sample pretreatment, and they can generate accurate results comparable to the conventional flow cytometry within a short period of time. The above novel techniques for on-chip CD4+ T cell count have a common feature in that they all use surface modification, such as filtration or a specific coating to immobilize white blood cells. Some inherent concerns in such systems include that how to avoid saturation of the specific binding between active surface and the T cells, and how to prevent non-specific binding of red blood cells and monocytes.

Morgan et al. (2006) reported a microchip detection system which integrates single particle fluorescence spectroscopy and multi-frequency electrical impedance sensing. Two pairs of metal electrodes are fabricated at the bottom of the microchannel along either side of the detection window, where two laser beams are focused at the mid-height of the channel. When a fluorescent particle translocates through the detection

window, the resulting AC impedance changes between halves of the two pairs of electrodes are recorded by the instrumentation amplifiers, and the fluorescent emission is detected by the optical system simultaneously. Their system can discriminate between different sizes and types of particles by fluorescent intensity and AC impedance signal. Based on the study by Xu et al (Xu et al, 2007; Sridhar et al, 2008), in this chapter, we will furbish this system with a fluorescence optical detection function and realize on-chip counting of the total number and the percentage of the fluorescence-labeled CD4+ T cells (5 μm to 10 μm in size). The resistive pulse sensing system determines the total number of the cells passing through the sensing aperture, while the concurrent fluorescence detection system determines only the number of cells with specific fluorescent tag. The absolute count of the CD4+ T cells and its percentage to the total lymphocytes can be analyzed by combining both results. We will show how this combination can facilitate the detection and phenotype analysis of the biological particles such as CD4+ T cells in a fast, simple, and accurate manner.

Experiment

Sample preparation

PBMC (Peripheral Blood Mononuclear Cell) were separated from blood of healthy donors through Ficoll-Hypaque (Pharmacia). Resting CD4+ T cells were purified using Robosep CD4+ T cell enrichment kit (StemCell Technologies) by a negative selection separation. For fluorescent staining, the freshly isolated or thawed CD4+ cells were resuspended at 20×10^6/ml in PBS (phosphate buffered saline) containing 5 μM

SYTO-62 (Molecular Probes) for 20 min (Note: SYTO-62 is a red fluorescent nucleic acid stain (excitation wavelength 638 nm, emission 660 nm) and generally has a stronger emission than the surface markers, such as CD4. However, the preliminary work presented in this study is to prove the concept, using the currently available filter set (far-red laser filter set). Later work will be focused on the detection of directly conjugated surface antibodies.). Cells were then washed 3 times in PBS and re-suspended at a final concentration of 10×10^6/ml in PBS. In order to stabilize the MOSFET drain current, we spun down the cells and re-suspended the cells in 7.5 mM sodium borate buffer with a pH of 9.45, which is not a natural physiological environment for cells. However, the lymphocytes we used have been chemically fixed. Therefore the cell phenotype is not affected by the suspension buffer. Cell fixation helps to keep the immuno-labeling on the cell surface for a much longer time (usually 24 hours in PBS). An independent test demonstrated that the fluorescence staining on the cells did not show obvious weakening and the expression of the surface marker was not affected by the borate buffer within 6 hours. The final cell concentration for each run is about 0.36×10^6/ml. For comparison, we made two kinds of cell solutions according to the percentage of stained cells to the total. One contains 100% stained cells, the other contains 50% stained cells (1:1 mixture of 100% stained cells and 100% unstained cells).

Cell counting by RPS using fluidic devices with integrated MOSFET

Coulter counter is based on the resistive pulse sensing (RPS) method and has been used to count and size biological cells for more than 40 years (Bayley and Martin, 2000; Bayley and Cremer, 2001; Schmidt et al, 2005). In this type of device, a small aperture is

embedded between two electrolyte solution units and a baseline ionic current is induced by applying an electrical bias across the aperture. When a cell passes through the aperture, it displaces a volume of electrolyte solution and the resistance of the aperture will increase temporarily. As a result, a transient ionic current modulation can be observed and used for counting cells. In this scheme, the ionic current modulation is approximately the same as the aperture resistance modulation. Different from the conventional Coulter counters, the authors in this work connect a commercial MOSFET with the fluidic circuit and detect cells by monitoring the modulation of the MOSFET's drain current. In a previous work of sensing polystyrene microbeads with this technique, it was shown that the resistance modulation can be amplified by 40 to 80 times and therefore the sensitivity can be improved substantially (Xu et al, 2007; Sridhar et al, 2008).

A schematic diagram of the microfluidic chip is shown in Fig. 6-2. The fluidic circuit includes three terminals and cells are translocated through the horizontal fluidic channel by electroosmotic flow, which is generated by applying an electrical bias across the horizontal channel. The horizontal main fluidic channel consists of three segments with a small sensing channel located between two large microchannels. A vertical channel connects the downstream end of the sensing channel to the gate of a commercial MOSFET (2N7000 N-Channel FET, Fairchild Semiconductor). When a cell is present in the sensing channel, the electrical resistance distribution in the fluidic circuit will be modified, which will lead to a modulation of the gate potential of the MOSFET, and hence a modulation of the MOSFET's drain current. Each pulse in the drain current signal corresponds to a single cell and the number of pulses represents the total number

of the cells passing through the sensing channel. The pulse height is proportional to the cell volume.

In our experiments, the MOSFET is biased to work in the sub-threshold regime, i.e., the gate potential, V_G, is less than the threshold voltage, V_T, of the MOSFET. In this regime, the MOSFET is more sensitive than in the saturation regime and the modulation of the drain current, I_D, can be related to the resistance modulation of the sensing channel, $\Delta R/R$, by (Xu et al, 2007; Sridhar et al, 2008)

$$\frac{\Delta I_D}{I_D} \approx \left(\frac{qV_G}{kT} - \frac{1}{2}\right) \cdot \frac{IR_1}{V_G} \cdot \frac{R}{R_t} \cdot \frac{\Delta R}{R} \tag{6.1}$$

where q, k, and T are the electron charge, Boltzmann's constant, and temperature, respectively. I is the ionic current through the fluidic channel and $R_t = R_2 + R + \Delta R + R_1$. R_2, R, and R_1 denote the resistances of three segments of the horizontal fluidic channel as labeled in Fig. 6-2 and ΔR represents the resistance increase of the sensing channel with a cell inside. Compared with the resistance modulation of the sensing channel (As seen in Eq. (6.1)), the modulation of the MOSFET drain current is amplified by a factor of

$$A = \left(\frac{qV_G}{kT} - \frac{1}{2}\right) \cdot \frac{IR_1}{V_G} \cdot \frac{R}{R_t} \tag{6.2}$$

which is much easier to detect. The typical amplification factor A is around 65.

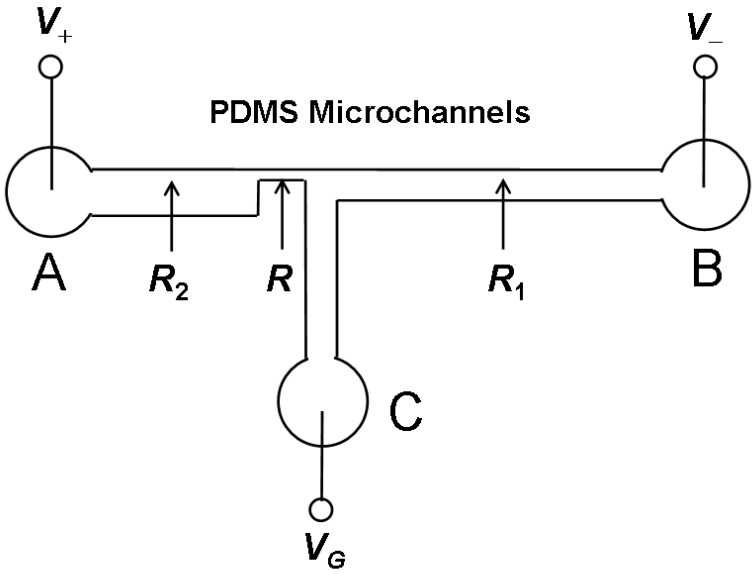

Figure 6-2 Schematic diagram of the microfluidic chip (not to scale).

To facilitate the adjustment of the gate potential, thus the working regime of the MOSFET, a positive voltage (V_+) is applied at the left end of the fluidic circuit and a negative voltage (V_-) is applied at the right end. The drain-source bias (V_{DS}) of the MOSFET is held constant for each experiment and the power supplies for V_+, V_-, and V_{DS} are commonly grounded with the current preamplifier. Platinum wire electrodes are immersed in the wells connecting the fluidic circuit and the electronic circuit. In this experiment, V_+, V_-, and V_{DS} are set as 8.9 V, -29 V, and 0.15 V, respectively.

Fluorescence detection and experimental set up

As mentioned above, the RPS method enhanced by the MOSFETs can do the total counting by detecting all of the cells passing through the sensing channel, no matter if the cells are fluorescence-labeled or not. In order to determine the percentage of cells with a specific fluorescence tag, we integrated the electronic detection system with an optical fluorescence system. The layout of the two systems is shown in Fig. 6-3.

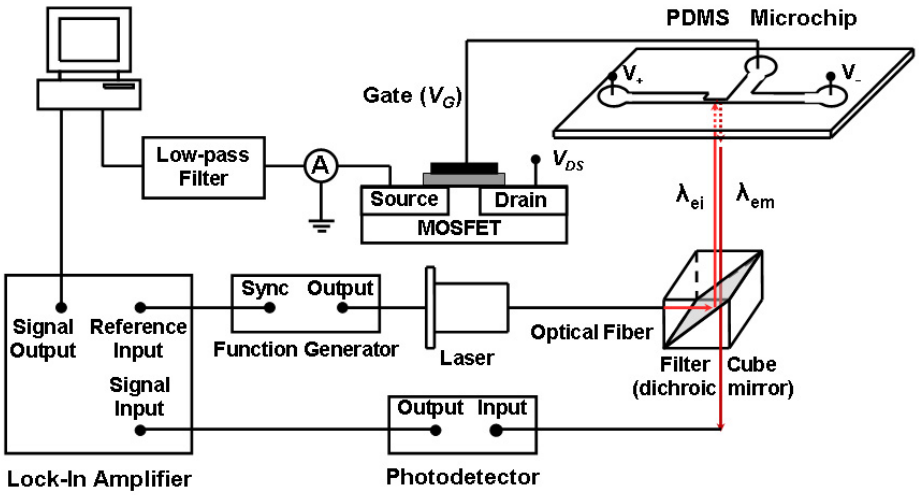

Figure 6-3 Schematics of the experimental setup.

The PDMS (poly-dimethylsiloxane) microchannel is fabricated on a glass substrate (24×60×0.15mm, VWR International) following the soft lithography protocol. The basic structure of the microfluidic circuit has been described in the previous section. All the branch channels are 30 um in depth (z-direction) and their widths are 800 um (connected to A), 160 um (connected to B) and 300 um (connected to C), respectively.

The dimension of the small sensing channel is 16 μm × 30 μm in cross-section and 150 μm in length. Before each test, the channels and wells are primed with 7.5 mM sodium borate buffer. The cell suspension is introduced into well A. Two DC power supply (Agilent, Santa Clara, CA) are used to drive the fluid flow from A to B as described above. When a fluorescence-labeled cell passes through the sensing channel, the RPS and fluorescence detection signals are recorded simultaneously.

As shown in Fig. 6-3, the microchip is mounted horizontally on a hollow metal platform. An optical fiber (200 μm in diameter, Silicon Lightwave Technology, CA) is fixed in a movable cartridge that is installed underneath the platform. The open tip of the optical fiber is arranged orthogonally opposing the upstream end of the sensing channel. The precise alignment between the microchip detection region and the optical fiber is achieved by a XYZ 3-axis travel translation stage and XY translator (Thorlabs, Newton, NJ). An optical microscope (SMZ800, Nikon Instrument Inc.) with high intensity polarizing attachment illuminator (NI 150, Nikon Instrument Inc.) and a CCD camera (Qimaging, Vancouver, British Columbia, Canada) are used to monitor the alignment.

The excitation is done with a 25mW single mode diode laser (wavelength of 635nm, Blue Sky Research, CA) and is modulated by a function generator (DS 350, Stanford Research Systems, Sunnyvale, CA) at a frequency of 13 Hz. The synchronous signals of the function generator are fed into a lock-in amplifier (SR 850, Stanford Research Systems, Sunnyvale, CA) as a reference input. The modulated laser goes through a filter cube (OZ Optics, Canada) and is reflected into the detecting fiber by the dichroic filter. The laser beam was focused at the upstream end of the sensing channel. When the stained cells pass through the sensing channel, the fluorescent tag is excited.

The incident emission penetrates the glass substrate and is transmitted by the fiber back to dichroic filter and a band pass filter. The optical signal is converted into an electric signal by a photo-detector (C5460-01, Hamamatsu, Japan) and detected by the lock-in amplifier. The output signal is recorded and visualized by a custom-made LABVIEW® code through a data acquisition board (PCI 6281, National Instruments, Austin, TX).

Results and discussion

The typical MOSFET drain current signal and the corresponding fluorescence detection signal when 100% stained CD4+ cell suspension are driven through the sensing channel are demonstrated in parallel in Fig. 6-4. For the MOSFET drain current, each downward spike indicates a cell and the depth of the spike is proportional to the volume ratio of the cell (i.e., the size of the cell) to the sensing channel. Although the cell cytoplasm contains highly conductive electrolytes, the cell membrane behaves like a very low loss capacitor, blocking the DC electric field and electric current from the interior of the cell, and causes the cell to behave like an insulating sphere (Jones, 1995). Therefore the electric current is blocked and the resulting potential modulation is sensed by a MOSFET drain current drop when a cell passes the narrow detection channel. Important information such as the total number and the size distribution of the cells passing through the sensing channel within a specific period of time can be derived from the drain current monitoring (quantitative analysis is in the following discussion). For the fluorescence signal (in voltage), each spike denotes a single fluorescence-tagged cell and its amplitude indicates fluorescent light intensity. Combining the results from these two systems, we can enumerate the absolute count and percentage of a cell subset tagged with a specific

fluorescent dye. In this graph, because 100% of the cells are fluorescence-tagged, each MOSFET drain current drop corresponds to a fluorescence signal spike. The one-to-one correspondence of the two systems can be clearly seen from Fig. 6-4 for a time span of 200 seconds. It is shown that the MOSFET drain current signal is highly synchronous with the fluorescence signal.

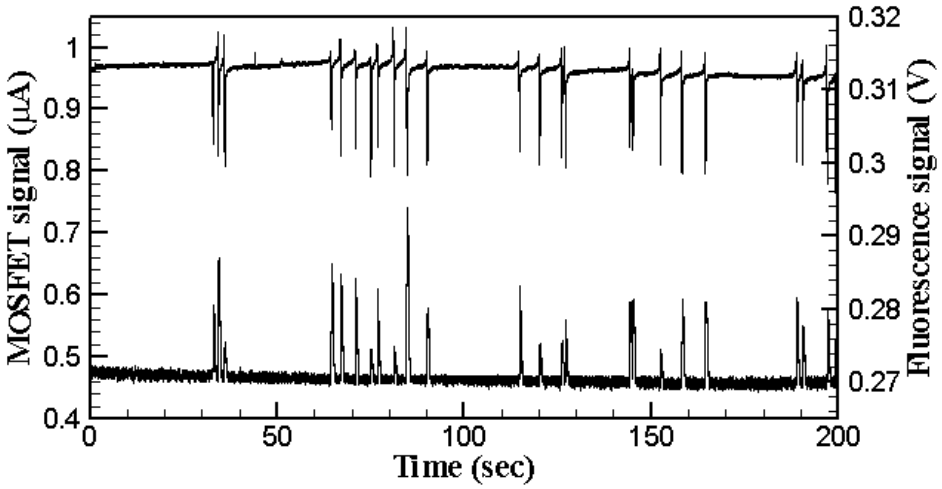

Figure 6-4 Detection of 100% stained CD4 cells by MOSFET drain current and by fluorescence signal. The upper plot and left axis indicates the MOSFET signal; the lower plot and right axis indicates the fluorescent signal.

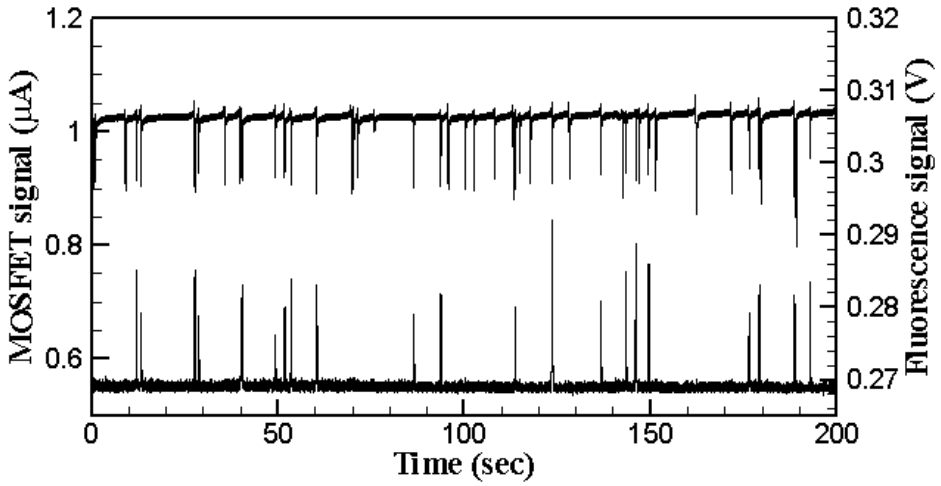

Figure 6-5 Detection of 50% stained CD4 cells by MOSFET drain current and by fluorescence signal. The upper plot and left axis indicates the MOSFET signal; the lower plot and right axis indicates the fluorescent signal.

In order to test the accuracy for percentage determination, nominally 50% stained cell suspension are driven through the sensing channel. The recorded MOSFET drain current and fluorescence signal are shown in Fig. 6-5. MOSFET signal shows total number of the cells for a time span of 200 seconds, whereas the detected fluorescence signals show only the cells tagged with fluorescence. From the result we can justify exactly which cells are fluorescently labeled and the percentage of the labeled cells to the total cell number count. Five individual tests were conducted with each test lasting about 11~12 minutes. The number count for all the tests are listed in Table 6-1. The weighted average percentage of the stained cells is 48.7%. For comparison, an aliquot of the nominally 50% stained cell suspension was analyzed concurrently by a commercial flow cytometer (BD Immunocytometry Systems, San Jose, CA) and the exact percentage of

the stained cells was determined to be 46.1%, as shown in Fig. 6-6. The integrated system in this study shows a comparable accuracy with the commercial flow cytometer.

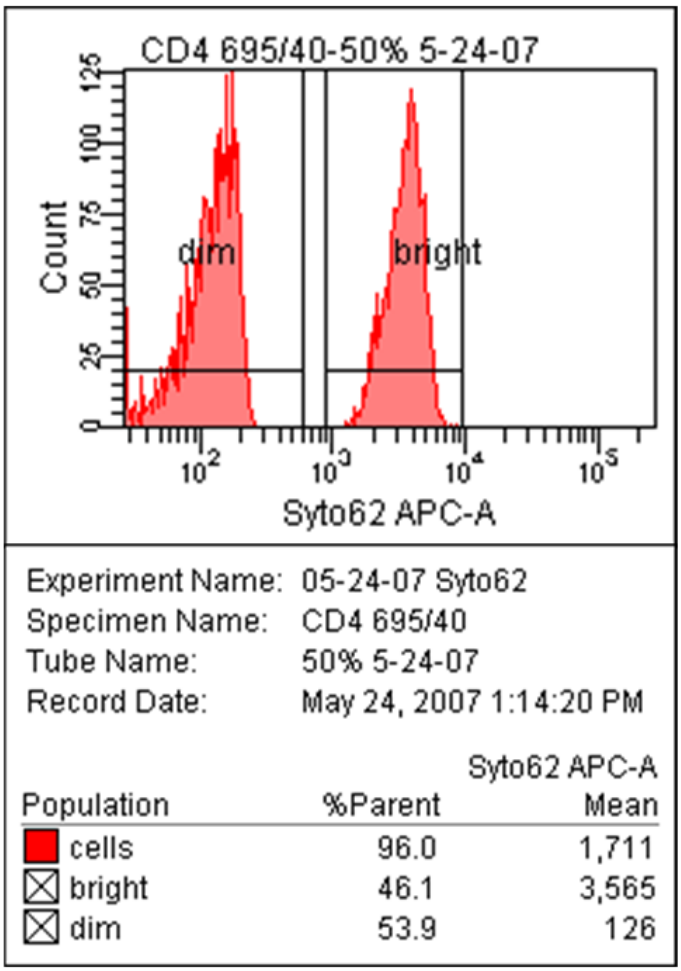

Figure 6-6 Cell counts for an aliquot of the nominally 50% stained cells suspension by commercial flow cytometer: the counts for "dim" and "bright" events denote the exact percentages of the un-labeled cells (53.9%) and the cells stained with Syto-62 (46.1%), respectively.

Table 6-1 Total count and percentage determination by five individual tests. The weighted average of these five tests is 48.7% (568/1166), and the standard deviation is calculated as 3.9%.

Test	1	2	3	4	5	Total
Stained cells	111	128	155	92	82	568
Cells number	222	262	290	211	181	1166
Stained cells (%)	50.0	48.9	53.4	43.6	45.3	48.7

As discussed above, the size of the cells can be determined by further studying the MOSFET drain current. The I_D-V_G curve of the MOSFET is calibrated before it is used in the experiment and the threshold voltage V_T is determined as 2.1 V for V_{DS}=0.15 V. The gate potential of the MOSFET can be inferred from the I_D-V_G curve and is about 1.66 V. As shown in Fig. 6-5, different cells lead to different magnitude drops of the MOSFET drain current, which indicates that the sizes of the cells are not uniform. The height of the resistive pulses range from 0.07 μA to 0.22 μA, or 7 ~ 20 % modulation to the baseline drain current (1.02 μA). Since the typical amplification factor A (in Eq. 2) in sub-threshold regime is about 65, the channel resistance modulation $\Delta R/R$ can be calculated by using Eq. (6.1), which ranges from 0.11% to 0.31%. The volume ratio of the cell to the sensing aperture approximates the modulation of the sensing aperture resistance, when the cell is small compared to the sensing aperture. Therefore, the diameter of the cell can be roughly determined to be 5.33 μm ~ 7.53 μm, which is consistent with the results from the commercial flow cytometer.

It is interesting to note that the drain current for most of the cells shows an enhancement-blockage modulation mode, i.e., an upward current peak immediately followed by a current drop when a cell passes through the sensing channel, in contrast to the monotonous blockage mode of polystyrene beads (Xu et al, 2007; Sridhar et al, 2008). The ionic current enhancement modulation has been reported recently for translocation of DNA molecules and Juniper tree pollens through nano/micro channels (Chang et al, 2004; Fan et al, 2005; Smeets et al, 2006; Zhe et al, 2007). Although we have not reached a good explanation, it was found that this special modulation mode is related to the buffer concentration (Fig. 6-7).

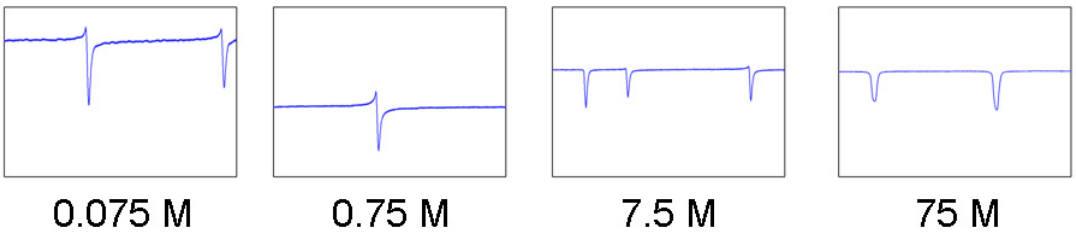

Figure 6-7 Dependence of the profiles of resistive pulses on the buffer concentration.

In addition to T lymphocytes, CD4 is also expressed on the surface of monocytes, macrophages, and dendritic cells. Therefore monocytes, which can be present at frequencies of 3 to 8 percent of the leukocytes in peripheral blood, may affect the counting accuracy for CD4+ T cells. The size of the monocytes ranges from 15 to 25 micron in diameter. However, the lymphocytes vary in size from 6 micron up to 15 micron, constituting 20 to 30 percent of the total leukocyte count, with small

lymphocytes predominating. The size distinction between lymphocytes and monocytes make it possible that they can be separated by size using DC-DEP (Chapters 3~5). This DC-DEP separation method can be integrated with the present microchip and remove the larger monocytes before enumerating the CD4+ T cells using fluorescence detection and resistive pulse sensing.

Microfluidic Differential Resistive Pulse Sensors

Experiment

System setup

The PDMS (poly-dimethylsiloxane) microfluidic chip was fabricated on a glass substrate (24×60×3 mm, VWR International) following the standard soft lithography protocol. The chip consists of a pair of mirror-symmetric channels (with sensing apertures) that are separated by a wall of 100 μm in thickness and share the same sample input (A) and waste reservoirs (B), as shown in Fig. 6-8. The fluidic conduit is connected to the electronic circuits by platinum wire electrodes submerged in four reservoirs. A DC bias ($V_+ - V_-$) was applied across the channel to induce the electroosmotic flow, which drove the particles through the sensing apertures from reservoir A to reservoir B. There are two gate branches connected to the differential amplifier (AD620, Analog Devices, Norwood, MA) at the upstream ends of both sensing apertures to detect the trans-aperture voltage modulation when particles are translocated. The signals were collected by a custom-made LABVIEW® code through a data acquisition board (PCI 6281, National

Instruments, Austin, TX). An aluminum Faraday cage was used to shield the microchip and the sensing electronics from the environmental electromagnetic interference. The sensing electronics, power source, and the data acquisition system are all connected using BNC connecters and coaxial cables.

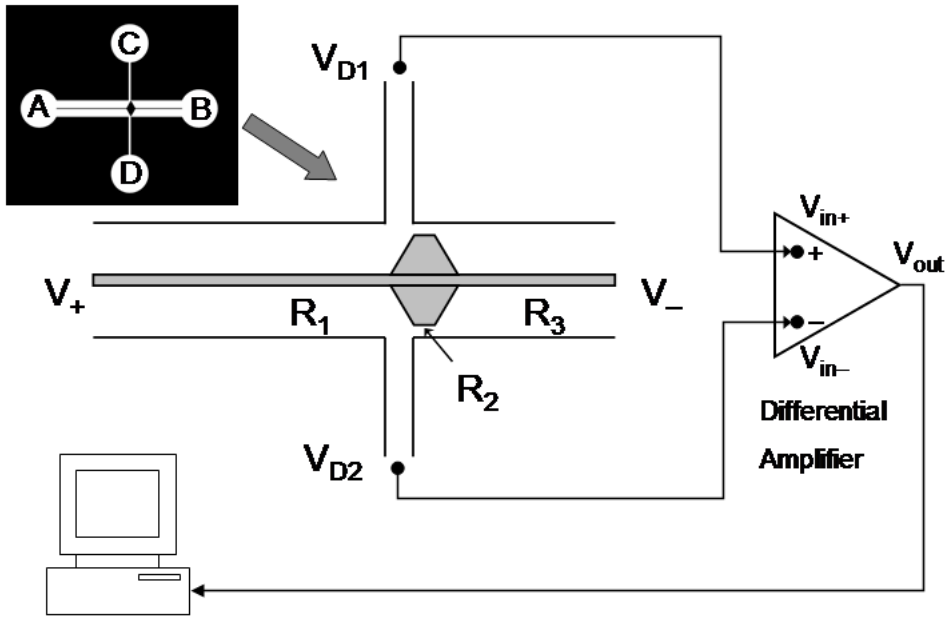

Figure 6-8 Chip design and system set up for one-stage differential amplification. A DC voltage ($V_+ - V_-$) is applied to drive the particles from A to B. Trans-aperture voltage (V_{D1} and V_{D2}) modulation are sensed by the two gate braches to C and D, which are the positive and negative inputs of the differential amplifier, respectively. The resistances of the three sections in the main channel are denoted by R_1, R_2, R_3, respectively.

Differential resistive pulse sensing

The trans-aperture voltage modulation is detected by the mechanism of differential amplification. The signal-to-noise ratio is significantly improved by the unique symmetric dual channel design and other electronic methods.

For microchip detection system as developed in this study, there are two major types of noise sources. One is the from the electrical power system, such as the system power supply and the ambient illumination, which has a characteristic frequency of 60 hertz. The other is from the intrinsic noise of the electronic components, such as the thermal fluctuation in a resistor, which can generate various interferences from several hundred hertz to over megahertz. The major advantage of the symmetric dual channel design in Fig. 6-8 lies in that it renders identical noise level for the output signals (V_{D1} and V_{D2}) from both gate branches. The voltage component common to the amplifier inputs (V_{in+} and V_{in-}) are called *common-mode voltage* (CMV). Obviously the various noises coupled in V_{D1} and V_{D2} constitute the CMV of the amplifier. When the two branches are connected to a differential amplifier of high *common-mode rejection ratio* (CMRR), the noise comprised in the CMV can be rejected significantly at the final output (V_{out}).

The basic principle of a differential amplifier with high CMRR is described by

$$V_{out} = A_{Gain}(V_{in+} - V_{in-}) = A_{Gain}\Delta V \tag{6.3}$$

where V_{out} is the amplified voltage output from the differential amplifier; A_{Gain} is the differential amplification factor (gain). V_{in+} and V_{in-} are the voltage inputs from the two gate branches, respectively (Fig. 6-8). According to the definition, the CMRR is a measure of how well the device rejects a common-mode signal, and is simply the ratio of differential gain A_{Gain} over the common-mode gain A_{CM} (CMRR = A_{Gain}/A_{CM} or in decibels $20\log_{10}(A_{Gain}/A_{CM})$). Different from Eq. (6.3), the output of a real differential amplifier is better described as $V_{out} = A_{Gain}(V_{in+} - V_{in-}) + A_{CM}(V_{in+} + V_{in-})/2$. The second term in this equation implies that the common-mode signal, and hence the coupled noise,

can be amplified by the common-mode gain. However, for an amplifier with high CMRR (100 dB for AD620), this term is negligible and the effect of the CMV can be significantly reduced.

When there is no particle passing through either of the two sensing apertures, ideally V_{in+} is equal to V_{in-} in amplitude for a perfectly symmetric fluid circuit. Thus the two inputs will cancel each other and the amplified output is zero. However for a real microchip, an original voltage difference exists between V_{D1} and V_{D2}. It is commonly referred to as *differential error voltage* (DEV), which is mainly because of the not perfectly symmetric nature of the dual channels from fabrication errors. In addition, other variations in fluid conditions, such as ionic concentration, temperature fluctuation, etc., in distinct channels may contribute to the DEV as well. The DEV can be amplified by the differential gain and thus the amplifier has a non-zero final output. When a particle passes through either one (but only one at the same moment) of the two sensing apertures, on top of the DEV, the resulting voltage modulation causes an additional input difference ΔV between V_{in+} and V_{in-}., which is amplified by the differential gain. According to Eq. (6.3), the voltage outputs of the amplifier for particles translocated through distinct sensing apertures are opposite in polarity, and hence the resistive pulses will show opposite profiles (upward or downward).

In addition, the voltage modulation can be optimized by proper design of the resistance distribution of the fluid circuit. The resistance change ΔR because of the presence of a particle inside the aperture leads to a voltage change ΔV at the corresponding detecting branch which can be easily derived as

$$\Delta V = \frac{R_1 \Delta R}{\left(R_1 + R_2 + R_3\right)^2 + \left(R_1 + R_2 + R_3\right)\Delta R}\left(V_- - V_+\right) \tag{6.4}$$

R_1, R_2, R_3 are the resistances of the three sections in the main channel (Fig. 6-8). Because of the substantially high input impedance (10 GΩ for AD620) of the amplifier compared with the fluid circuit (about 2 MΩ for our microchip), the resistance of the detecting gate channel can be ignored. Assuming $R_1 = k(R_2 + R_3) = kR$ (k is an positive proportional factor) and $\Delta R << R_1 + R_2 + R_3$, from Eq. (6.4), one can obtain

$$\Delta V \approx \frac{k}{(k+1)^2}\frac{\Delta R}{R}\left(V_- - V_+\right) = f(k)\frac{\Delta R}{R}\left(V_- - V_+\right) \tag{6.5}$$

It can be easily inferred that function $f(k)$ reaches its maximum when k equals to 1, i.e., $R_1 = R_2 + R_3$. Therefore a maximum voltage modulation can be achieved by varying the length and width, and hence the resistance of each section of the fluid conduit. For the microchip used in this study, the dimension of the three major sections (Fig. 6-8) are: 800 μm × 6000 μm for the upstream channel (R_1), 16 μm × 50 μm for the sensing aperture (R_2), 800 μm × 5000 μm for the downstream channel (R_3). All of the fluid conduits have the same depth of 20 μm.

Results and discussion

One-stage differential amplification

Figure 6-9 shows the detection of 1, 2, and 4.84 μm (in diameter) particles suspended in 7.5 mM sodium borate buffer. Each spike denotes a single particle, verified by concurrent observation with an optical microscope. The upward and downward pulses

denote the particles translocated through two different sensing apertures, respectively. The amplitude of the spike is dependent on the size of the particle. The highest spikes, which correspond to the 4.84 μm particles, have an average amplitude of 3.09 V. Whereas the smallest spikes (inset of Fig. 6-9), which correspond to the 1 μm particles, have an average amplitude of 33 mV. The baseline thickness (fluctuation because of the noise) is about 10 mV in Fig. 6-9. The signal-to-noise ratio for 1 μm particle is about 10.37 dB (33 mV : 10 mV). The amplified DEV is about 3.2 V in Fig. 6-9. Since the differential gain is 100 V/V, one can infer that the actual DEV for the two gate branches is about 32 mV.

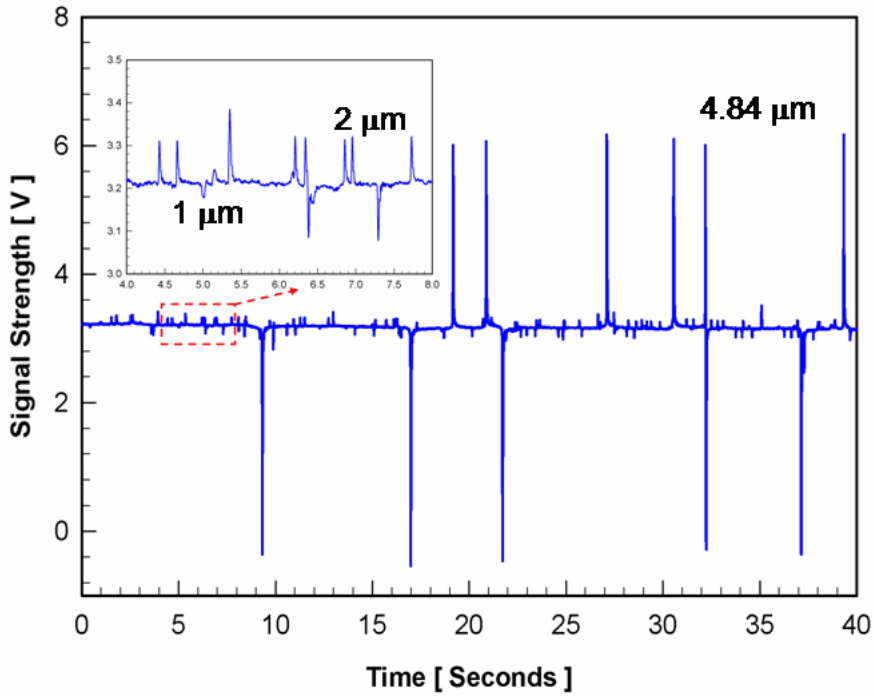

Figure 6-9 Resistive pulses of 1, 2, and 4.84 μm particles in 7.5 mM sodium borate buffer. The magnified inset shows the signal strength of 1 and 2 μm particles. The gain of the differential amplifier was set at 100 V/V. The applied voltage across the main channel was set to be 35V.

Early research showed that the increase in the aperture resistance because of the presence of a particle inside is a function of the aperture dimension and the particle size (DeBlois and Bean, 1970). In the limit of $d << D$, the function can be expressed as

$$\Delta R = \frac{4\rho d^3}{\pi D^4}\left[1+\frac{2d^3}{3D^2L}+\left(\frac{2d^3}{3D^2L}\right)^2+\ldots\right] \tag{6.6}$$

where ρ is the resistivity of the suspending fluid; d is the particle diameter; D and L are the diameter (or hydraulic diameter for non-circular aperture) and the length of the aperture, respectively. For the present case of very small particle inside a relatively large microaperture, the higher order corrections in above expression are negligible. Thus the resistance change is proportional to the particle volume, and hence the volume ratio for an aperture of fixed dimension. Important information such as the frequency and the size distribution of the particles translocated through the sensing aperture can be derived from the resistive pulse monitoring. In addition, the residence time of the particle inside the sensing aperture can be analyzed from the time scale. Further study shows that the ratio of peak amplitudes (1 : 3.82 : 94) and the volume ratio (1 : 8 : 113) for the three different particles do not satisfy a strict linear relationship. We attribute this failure to the fact that the particles are relatively large compared with the aperture, which makes the assumption for Eq. (6.6) invalid. But we still cannot explain why the peak strength for 2 μm particles is more away from the linear relationship than that for 4.8 μm particles.

Two-stage differential amplification

The smallest particles we could detect using the above one-stage amplification are 1 μm in diameter. It is impractical if one wants to increase the sensitivity solely by

increasing the differential gain, because the amplified DEV could be significantly high and will cause the final output to exceed the detection limit of the amplifier (about 12 V for AD620). To circumvent this problem and achieve a higher sensitivity, we implemented a two-stage amplification scheme using three amplifiers to reject the DEV in the one-stage amplification (Fig. 6-10). In this scheme, the DEV can be offset by adjusting the reference of the amplifiers in the fist stage which are set at low differential gain. Therefore we applied a lower gain for the first-stage (A_1 = 25) and a higher gain for the second-stage (A_2 = 100). Thus the total gain of the final output is 5000 ($A_{\text{Gain}} = 2A_1A_2$). In addition, an R-C low pass filter with cutoff frequency of 160 Hz was developed to further suppress the high frequency noise after the amplification and protect the resistive pulse signal from distortion.

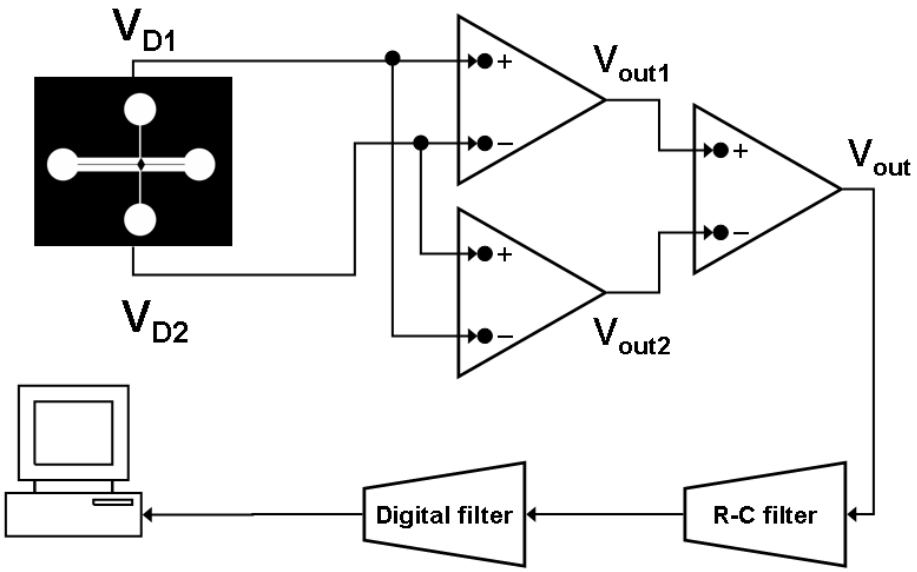

Figure 6-10 Design of two-stage differential amplification scheme. Since the original output from fluid circuit (V_{D1} and V_{D2}) are connected to the inputs of opposite polarity of the two amplifiers in the first-stage, the final gain of the two-stage amplification is, $A_{Gain} = 2A_1A_2$, which is twice of the multiplication (A_1A_2) of the gains of the individual amplifiers in both stages.

This scheme was successfully applied in detection of 520 nm particles in a suspension mixed with 1 μm particles, as shown in Fig. 6-11. The peak amplitude for the 520 nm particles is about 300 mV, which is clearly distinguishable from the baseline that has a thickness of about 100 mV. A high signal-to-noise ratio 9.54 dB (300 mV : 100 mV) is achieved for 520 nm particles under such high amplification. The peak amplitude for 1 μm particles has been improved to 2.4 V, while the baseline thickness is only 100 mV. Hence we have improved the signal-to-noise ratio by almost 3 times (from 9.54 dB to 27.6 dB). This is because of the noise reduction by every differential amplifier and by the R-C low pass filter in the sensing circuits. By analyzing the peak amplitudes of 1 μm and 520 nm particles, we found that the ratio of the signal strengths 8:1 (2.4 V : 300 mV) is approximately equal to the ratio of the particle volumes. As predicted by Eq. (6.6), the signal strength and volume ratio for 1 μm and 520 nm particles shows better linear relationship compared with that for larger particles. Moreover, the 520 nm particle represents a volume ratio to the sensing aperture of 0.0004%, which is about 10 times lower than the current commercial Coulter counter (0.0037%) (Technical specifications of Beckman Coulter® Multisizer™ 3. Available at: www.beckmancoulter.com/MS3. The dynamic range of the aperture is 27,000 : 1 by volume, which corresponds to a volume ratio about 0.0037%.) and similar devices reported so far (0.006%) (Xu et al, 2001; Sridhar et al, 2008).

One may expect the amplification can be extended to higher stages to realize detection of even smaller particles. However, there is a trade-off between the amplification and the stability of the system output. Except that the DEV under very high gain may cause the final output to exceed the detection limit, the system is so sensitive to

the perturbation from the fluid circuit and the ambient environment that, under substantially high amplification, the baseline will drift dramatically and make the detection impossible.

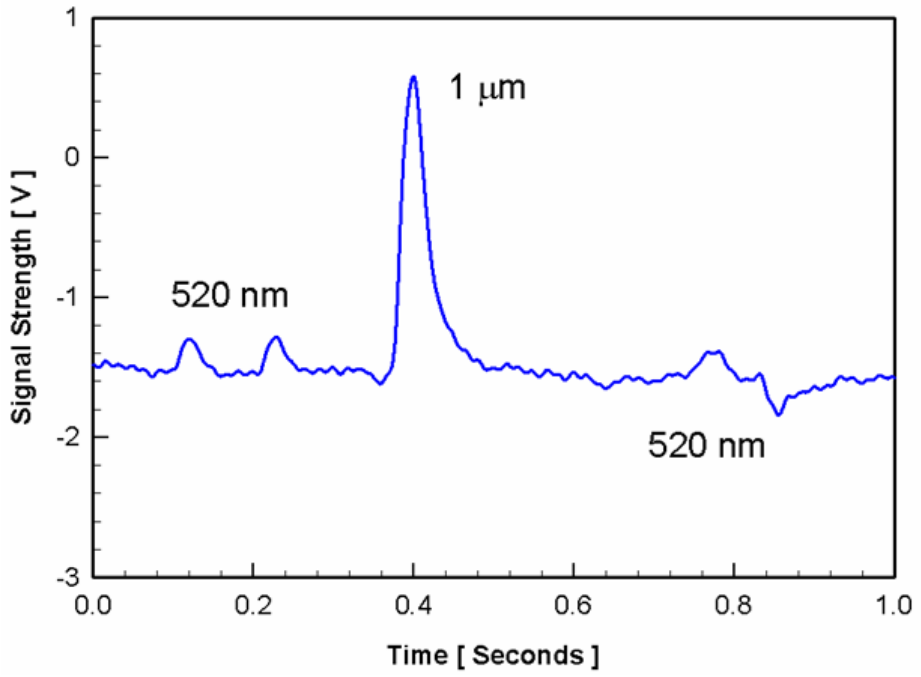

Figure 6-11 Resistive pulses of 520 nm and 1 μm particles with two-stage differential amplification. Working buffer was 75 mM sodium borate. The applied voltage across the main channel was set to be 35 V.

Noise suppression

As mentioned above, we applied three methods in order to systematically suppress the noise level and improve the signal-to-noise ratio: 1) unique symmetric dual channel design; 2) two-stage differential amplification; and 3) R-C low pass filter for the final signal output. Keeping all the other factors the same, we conducted series of experiments using the same microchip and target particles (2 μm in diameter) to evaluate

the noise suppression effect for each of the above three methods. The typical signal profiles are shown in Fig. 6-12 and the calculated signal-to-noise ratios are listed in Table 6-2 for four different conditions.

Table 6-2 Comparison of the signal-to-noise ratios between single-channel and dual-channel setups, one-stage and two-stage amplifications, and with and without R-C low pass filter.

	Single Channel	Dual Channel		
Amplification	1 stage	1 stage	2 stages	
Differential gain	10	10	40	
R-C low pass filter	No	No	No	Yes
Signal-to-noise ratio (dB)	N/A	7.6	12.74	20.83

From detection using single channel (Fig. 6-12a), the resistive pulses of 2 μm particles are barely distinguishable from the fluctuation of the baseline, which is strongly coupled with 60 Hz noise and other electronic noises. In contrast, under the same differential gain of the amplifier (A_G = 10), symmetric dual channel design (Fig. 6-12b) can improve the signal-to-noise ratio to about 7.6 dB (12 mV : 5 mV). If using a two-stage amplification scheme (Fig. 6-12c) the signal-to-noise ratio can be further improved to 12.74 dB (65 mV : 15 mV). After the R-C low pass filter, the final output has an even higher signal-to-noise ratio of about 20.83 dB (55mV : 5mV) (Fig. 6-12d). Conclusively, each of the three methods applied in this study contributed significantly in achieving a high sensitivity for particle detection using resistive pulse sensing.

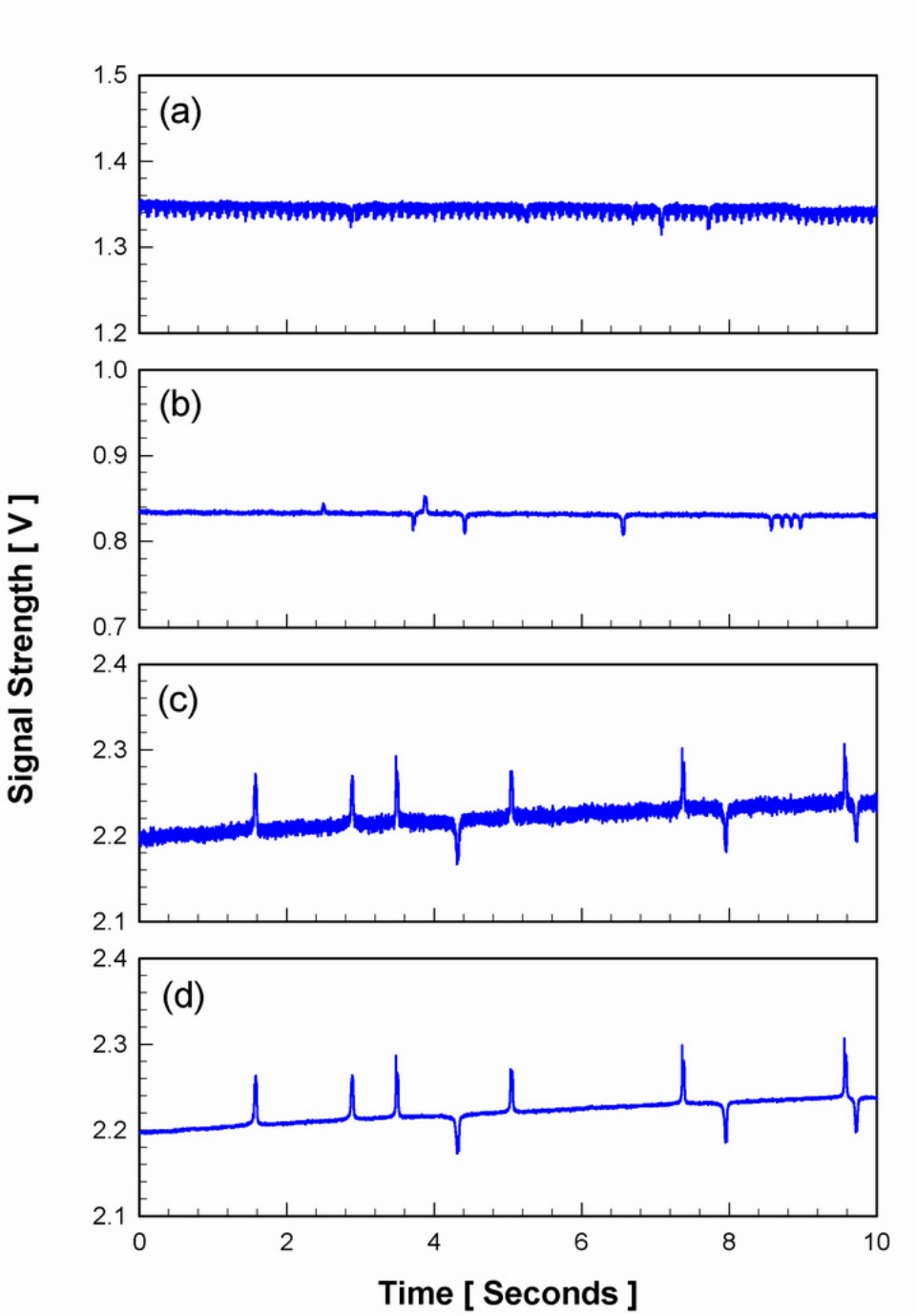

Figure 6-12 Noise analysis: Comparison of the noise level of four different methods: (a) single channel design; (b) symmetric dual channels; (c) symmetric dual channels with two-stage amplification; and (d) symmetric dual channels with two-stage amplification and R-C low pass filter. All the working conditions and signal-to-noise ratio are shown Table 6-2. Working buffer was 75 mM sodium borate. The applied voltage across the main channel was set to be 20 V.

Summary

A CD4+ T cell counting device is demonstrated in this chapter. This device combines the fluorescence detection and resistive pulse sensing enhanced by a MOSFET. The kernel component of the device is a PDMS microchannel network, in which there is a very small sensing aperture allowing only one cell going through at each moment. When a cell passes the sensing channel, the resistive pulse sensing and fluorescence detection are operated concurrently. MOSFET signal records all of the cell events, while fluorescent signal only records the cells with specific fluorescent tag. In this way, the device can accomplish an absolute number counting and the relative percentage calculation of the T-cells. Compared with commercial flow cytometers, this device is small, cost effective, easy to operate, and comparably accurate. It may potentially realize all the functions necessary for a general flow cytometer to count and characterize the total and subsets of the fluorescently labeled biological particles.

In order to further improve the detection sensitivity, an on-chip resistive pulse sensing scheme based on symmetric mirror-channel design and differential amplification has been developed. The amplification is optimized by both fluid circuit configuration and multiple-stage amplifications. The noise reduction has been significantly improved by common-mode rejection through the unique dual channel design, multiple-stage amplification, and R-C low filter in the sensing electronics. The lowest volume ratio of the particles detected to the sensing aperture is 0.0004%, with particles of 520 nanometers in diameter in a sensing aperture of $50\times16\times20$ μm^3, using two-stage amplification, which is about 10 times lower than the detection limit of current commercial Coulter counters and similar devices reported so far.

CHAPTER VII

CONCLUSIONS AND FUTURE STUDIES

Contributions Made by this Study

Since the biological reagents and particles, such as blood cells, bacteria, and macromolecules, exist in fluidic natural environment, microfluidics-based lab-on-a-chip devices render excellent platforms for biomedical manipulations and assays. The lab-on-a-chip technology develops amazingly fast and has profound impacts on the healthcare industry in recent decades. This emerging field is actively approached by scientists from many disciplines and exploited for wide range of applications. The microfluidics-related research in the past decade has generated thousands of research articles and has attracted billions of research grants. The lab-on-a-chip systems have competitive advantages over the conventional biomedical instruments. Their downscaling sizes make them highly portable, which is extremely attractive for on-site diagnosis. The manufacturing and operational costs are significantly reduced making them disposable and affordable in resource-poor settings. The dramatic decrease in sample and reagents consumption makes them work faster and further drive down the cost per unit test. Separation of the bioparticles according to their phenotypes is a fundamental technique in biology and medical biotechnology. Because of their small size ranging from hundreds of nanometers to tens of micrometers, and their dense population, one needs more advanced techniques and subtle devices to physically access the cells. Although the current lab-on-a-chip technology can now realize some basic manipulations, such as loading, docking,

culturing, sorting, lysis, detection and even single-cell on-chip analysis, tremendous research effort is still required for precise control and quantitative analysis of the bioparticles. Therefore the overall objective of my dissertation research is to develop a microfluidic system for quantitative manipulation of cells and other biological particles.

On-chip separation by dielectrophoresis

Specifically, the main contribution of my work to the lab-on-a-chip technology is to develop a microchip device for cell separation by applying the non-linear electrokinetic phenomenon, dielectrophoresis (DEP) (chapters 3, 4, and 5). DEP arises from the interaction of a dielectric particle, such as a cell, and a highly non-uniform electric field which can be generated under a DC or AC electric field by specially designed features in fluid conduit, such as obstruction or hurdles using electrically insulating materials. Because electric fields can be scaled down easily at the microscale, a highly non-uniform electric field at a length scale comparable to cell size can be generated at relatively lower voltages. The DEP force acting on a cell is proportional to the cell's volume. Thus the moving cells deviate from the streamlines and the degree of deviation is dependent on the cell size. Finally the cells of different sizes are inducted into different collection wells according to their different degrees of deviation. This work is the foundation of the rest of my dissertation which is aimed at refining the device to extend the applications of the DEP separation system and integrate it into a multi-functional biochip.

On-chip detection and counting

To integrate the lab-on-a-chip devices with the important detection function, we designed microchip with a small sensing aperture for detection of micron and sub-micron particles suspended in buffer solution. The highly sensitive detection was achieved by resistive pulse sensing scheme enhanced by a MOSFET (metal oxide semiconductor field effect transistor) or multiple-stage differential amplifications (chapter 6). The amplification is optimized by both fluid circuit configuration and the unique channel design. The lowest volume ratio of the particles detected to the sensing aperture is 0.0004%, which is about 10 times lower than the detection limit of current commercial Coulter counters and similar devices reported so far. As a real application for HIV diagnosis, we further furbished this system with a fluorescence optical detection function and realized on-chip counting of the total number and the percentage of the fluorescence-labeled CD4+ T cells.

Directions for Future Studies

As an excellent example of commercializing the cutting-edge lab-on-a-chip technologies, portable home blood glucose monitor for diabetes has achieved great market success in recent decades (Newman and Turner, 2005). In the absence of a cure for diabetes, home blood glucose monitoring will keep dominating and new non-invasive electrochemical sensing technologies keep arising in research institutions and being commercialized by the major business players. Other fast advancing lab-on-a-chip technologies will continue to change human life. Thanks to the vastly increased concern in global public health, the funding climate for the development of the microfluidics

based lab-on-a-chip diagnostic systems is good (Yager et al, 2006). The diversified supporting sources range from the international agencies (Human Frontier Science Program, World Health Organization, etc.), national governments (NIH, NSF, DOE, DOD, etc), to various private foundations (American Heart Association, Bill and Melinda Gates Foundation, etc).

My research will continue to look at how microfluidics can be applied in development of biomedical microdevices. More specifically, in the fundamental perspective, I intend to investigate the interfacial phenomena related to the micron and submicron sized bioparticles; in the application perspective, I intend to develop integrated biochip devices which can perform multiple bioanalytical functions, such as detection, characterizing, and manipulation, for a variety of biological particles.

Based on the results presented in this study, future research will be focused on two aspects as listed in the following:

1) In the fundamental perspective, I intend to investigate the interfacial phenomena related to the micron and submicron sized bioparticles. In the modeling of throughout this study, the cell is treated as an insulating particle because of the cell membrane of very low conductivity. In reality, the cell membrane is not perfectly insulating. The cell membrane will be polarized under high electric field strength, which is true at some constrictions in the microchannel network. The polarization of the cell membrane will affect the polarization of the suspending medium and hence the local electric field surrounding the cell. The electrophoretic force and the dielectrophoretic force which the cell experiences will be different from those without considering the membrane polarization. I intend to investigate the polarization mechanism of the cell

membrane and develop a valid model for better estimation of the cell motion and its effect on the local electric field when it translocates the microchannel constriction.

2) In the application perspective, I intend to develop integrated biochip devices which can perform multiple bioanalytical functions, such as separation, detection, and manipulation, for a variety of biological particles. Specifically, I plan to integrate the DC-dielectrophoretic separation, optical fluorescence and resistive pulse sensing (RPS) based detection and counting, and fluorescence or RPS activated cell dispensing into a single microchip.

3) Specifically, in the previous work using resistive pulse sensing of cells, we found an interesting phenomenon that the resistive pulses generated by most of the cells show an enhancement-blockage modulation mode, *i.e.*, a temporal decrease of resistance immediately followed by a resistance increase when a cell passes through the sensing aperture, in contrast to the monotonous blockage mode of polystyrene beads. So far, however, there is no valid and quantitative model to explain this phenomenon in the literature. As a short term research objective, I intend to investigate the charging mechanism of the cell membrane and develop a valid model for better understanding of this unique phenomenon. More importantly, the model could inspire new applications for characterizing different bioparticles.

4) Current methods for separation of the bioparticles are mostly based on the phenotype or immunological labeling. However, phenotypic separation is limited to the bioparticles with large size or shape difference. And immunological labeling for bioparticles with small phenotypic difference is expensive and requires complex optical detection system. I intend to investigate label-free and less expensive methods for

characterizing and separation of the bioparticles (ranging from DNA, bacteria, to cells), based on the difference of their membrane or cytoplasmic properties (dielectric response, densities, or other inherent properties). The long-term goal is to develop a portable microdevice with multiple bio-analytical functions for on-site diagnosis, forensic investigation, or bio-defense applications.

In conclusion, I plan to look ahead to issues that will necessarily arise if microfluidics is to be used in development of lab-on-a-chip devices. My particular focus is on the control of the bio-reagent transport and methods for characterizing and manipulation of bioparticles. I plan to advance our understanding of biological transport phenomena by fundamental investigations. The impact of this research will be to broaden the application of the microfluidics by making lab-on-a-chip technology better and more accessible.

REFERENCES

Aldaeus F, Lin Y, Amberg G, Roeraade J (2006) J Chromatography A 1131: 261-266.

Altomare L, Borgatti M, Medoro G, Manaresi N, Tartagni M, Guerrieri R, Gambari R, (2003) Biotechnol. Bioeng. 82: 474-479.

Arai F, Ichikawa A, Ogawa M, Fukuda T, Horio K, Itoigawa K (2001) Electrophoresis 22: 283-288.

Arnold WM (2001) IEEE Trans. Industrial Appl. 37: 1468-1475.

Arnold WM, Schwan HP, Zimmermann U (1987) J. Phys. Chem. 91: 5093-5098.

Arnold WM, Zimmermann U (1988) J. Electrostatics 21: 151-191.

Aubry N, Singh P (2006) Electrophoresis 27: 703-715.

Barbulovic-Nad I, Xuan X, Lee JSH, Li D (2006) Lab Chip 6: 274-279.

Barrett LM, Skulan AJ, Singh AK, Cumming EB, Fiechtner GJ (2005) Anal. Chem. 77: 6798-6804.

Bayley H, Cremer PS (2001) Nature 413: 226-230.

Bayley H, Martin CR (2000) Chem. Rev. 100: 2575-2594.

Bazant MZ, Squires TM (2004) Phys. Rev. Lett. 92: 066101.

Beck JD, Shang L, Li B, Marcus MS, Hamers RJ (2008) Anal. Chem. 80: 3757-3761.

Becker FF, Wang X-B, Huang Y, Pethig R, Vykoukal J, Gascoyne PRC (1995) Proc. Natl. Acad. Sci. USA 92: 860-864.

Ben Y, Chang H-C (2002) J. Fluid Mech. 461: 229-238.

Ben Y, Demekhin EA, Chang H-C (2004) J. Colloid Interface Sci. 276: 483-497.

Bennett DJ, Khusid B, James CD, Galambos PC, Okandan M, Jacqmin D, Acrivos A (2003) Appl. Phys. Lett. 83: 4866-4868.

Bezrukov SM, Vodyanoy I (1995) Nature 378: 362-364.

Bezrukov SM, Vodyanoy I, Parsegian VA (1994) Nature 370: 279-281.

Bhatt KH, Grego S, Velev OD (2005) Langmuir 21: 6603-6612.

Bligh M, Stanley KG, Hubbard T, Kujath M (2008) J. Micromech. Microeng. 18: 045002.

Borgatti M, Altomare L, Abonnec M, Fabbri E, Manaresi N, Medoro G, Romani A, Tartagni M, Nastruzzi C, Di Croce S, Tosi A, Mancini I, Guerrieri R, Gambari R (2005) International J. Oncology 27: 1559-1566.

Borgatti M, Altomare L, Baruffa M, Fabbri E, Breveglieri G, Feriotto G, Manaresi N, Medoro G, Romani A, Tartagni M, Gambari R, Guerrieri R (2005) International J. Molecular Med. 15: 913-920.

Braschler T, Demierre N, Nascimento E, Silva T, Oliva AG, Renaud P (2008) Lab Chip 8: 280-286.

Carbonaro A, Sohn LL (2005) Lab Chip 5: 1155-1160.

Castellanos A, Ramos A, González A, Green NG, Morgan H (2003) J. Phys. D: Appl. Phys. 36: 2584-2597.

Cen EG, Dalton C, Li Y, Adamia S, Pilarski LM, Kaler KVIS (2004) J. Microbiol. Methods. 58: 387-401.

Cetin B, Li D (2008) Electrophoresis 29: 994-1005.

Chan KL, Gascoyne PRC, Becker FF, Pethig R (1997) Biochim. Biophys. Acta 1349: 182-196.

Chang H, Kosari F, Andreadakis G, Alam MA, Vasmatzis G, Bashir R (2004) Nano Lett. 4: 1551-1556.

Chen DF, Du H, Li WH (2006) J. Micromech. Microeng. 16: 1162-1169.

Chen DF, Du H, Li WH (2007) Sensors Actuators A 133: 329-334.

Cheng X, Irimia D, Dixon M, Sekine K, Demirci U, Zamir L, Tompkins RG, Rodriguez WR, Toner M (2007) Lab Chip 7: 170-178.

Cheng X, Irimia D, Dixon M, Ziperstein JC, Demirci U, Zamir L, Tompkins RG, Toner M, Rodriguez WR (2007) J. Acquir. Immune. Defic. Syndr. 45: 257-261.

Cheng X, Liu YS, Irimia D, Demirci U, Yang L, Zamir L, Rodriguez WR, Toner M, Bashir R (2007) Lab Chip 7: 746-755.

Chin CD, Linder V, Sia SK (2007) Lab Chip 7: 41-57.

Chiou PY, Ohta AT, Wu MC (2005) Nature 436: 370-372.

Choi S, Park J-K (2005) Lab Chip 5; 1161-1167.

Choi W, Kim JS, Lee DH, Lee KK, Koo DB, Park JK (2008) Biomed Microdevices 10: 337-345.

Choi W, Kim SH, Jang J, Park JK (2007) Microfluid. Nanofluid. 3: 217-225.

Chou CF, Tegenfeldt JO, Bakajin O, Chan SS, Cox EC, Darnton N, Duke T, Austin RH (2002) Biophys. J. 83: 2170-2179.

Chou CF, Zenhausern F (2003) IEEE Eng. Med. Biol. Mag. 22: 62-67.

Chu KT, Bazant MZ (2006) Phys. Rev. E 74: 011501.

Crane JS, Pohl HA (1968) J. Electrochem. Soc. 115: 584-586.

Cruz JM, García-Diego FJ (1997) Annual Meeting of IEEE Industry Applications Society, New Orleans, Lousiana, pp2012.

Cui L, Morgan H (2000) J. Micromech. Microeng. 10: 72-79.

Cui L, Zhang T, Morgan H (2002) J. Micromech. Microeng. 12: 7-12.

Cummings EB (2003) IEEE Eng. Med. Biol. Mag. 22: 75-84.

Cummings EB, Griffiths SK, Nilson RH, Paul PH (2000) Anal. Chem. 72: 2526-2532.

Cummings EB, Singh AK (2000) Proc. SPIE, Santa Clara, CA, pp. 164–173.

Cummings EB, Singh AK (2003) Anal. Chem. 75: 4724-4731.

De Gasperis G, Yang J, Becker FF, Gascoyne PRC, Wang X-B (1999) Biomed. Microdevices 2: 41-49.

DeBlois RW, Bean CP (1970) Rev. Sci. Instrum. 41: 909-916.

Demierre N, Braschler T, Linderholm P, Seger U, van Lintel H, Renaud P (2007) Lab Chip 7: 355-365.

Demierre N, Braschler T, Muller R, Renaud P (2007) Transducers & eurosensors '07. the 14th international conference on solid-state sensors, actuators and microsystems, Lyon, France, June 10-14, 2007: 1777-1780.

Demierre N, Braschler T, Muller R, Renaud P (2008) Sensors Actuators B 132: 388-396.

Dittrich PS, Manz A (2006) Nat. Rev. Drug Discov. 5: 210-218.

Dittrich PS, Tachikawa K, Manz A (2006) Anal. Chem. 78: 3887-3908.

Doh I, Cho Y-H (2005) Sensors Actuators A 121: 59-65.

Du H, Li WH, Chen DF, Shu C (2004) Int. J. Mechanics in Design 1: 115-130.

Dürr M, Kentsch J, Müller T, Schnelle T, Stelzle M (2003) Electrophoresis 24: 722-731.

Duffy DC, McDonald JC, Schueller OJA, Whitesides GM (1998) Anal. Chem. 70: 4974-4984.

El-Ali J, Sorger PK, Jensen KF (2006) Nature 442: 403-411.

Erickson D, Sinton D, Li D (2003) Lab Chip 3: 141–149.

Fabbri E, Borgatti M, Manaresi N, Medoro G, Nastruzzi C, Di Croce S, Tosi A, Mazzitelli S, Mancini I, Guerrieri R, Gambari R (2008) J. Appl. Polymer Sci. 109: 3484-3491.

Fan R, Karnik R, Yue M, Li D, Majumdar A, Yang P (2005) Nano Lett. 5: 1633-1637.

Fan SK, Huang PW, Wang TT, Peng YH (2008) Lab Chip 8: 1325-1331.

Fatoyinbo HO, Hoettges KF, Hughs MP (2008) Electrophoresis 29: 3-10.

Feeney L, Berman ER (1976) Invest. Ophth. Vis. Sci. 15: 789-792.

Felten M, Staroske W, Jaeger MS, Schwille P, Duschl C (2008) Electrophoresis 29: 2987-2996.

Flanagan LA, Lu J, Wang L, Marchenko SA, Jeon NL, Lee AP, Monuki ES (2008) Stem Cells 26: 656-665.

Forry SP, Reyes DR, Gaitan M, Locascio LE (2006) J. Am. Chem. Soc. 128: 13678-13679.

Foster KR, Sauer FA, Schwan HP (1992) Biophys. J. 63: 180-190.

Fuchs AB, Romani A, Freida D, Medoro G, Abnonnenc M, Altomare L, Chartier I, Guergour D, Villiers C, Marche PN, Tartagni M, Guerrieri R, Chatelain F, Manaresi N (2006) Lab Chip 6: 121-126.

Fuhr, G, Müller T, Baukloh V, Lucas K (1998) Human Reproduction 13: 136-141.

Gadish N, Voldman J (2006) Anal. Chem. 78: 7870-7876.

Gagnon Z, Chang H-C (2005) Electrophoresis 26: 3725-3737.

Gascoyne PRC, Huang Y, Pethig R, Vykoukal J, Becker FF (1992) Meas. Sci. Technol. 3: 439-445.

Gascoyne PRC, Mahidol C, Ruchirawat M, Satayavivad J, Watcharasit P, Becker FF (2002) Lab Chip 2: 70-75.

Gascoyne PRC, Vykoukal J (2002) Electrophoresis 23: 1973-1983.

Gawad S, Cheung K, Seger U, Bertsch A, Renaud P (2004) Lab Chip 4: 241-251.

Gimsa J, Marszalek P, Loewe U, Tsong TY (1991) Biophys. J. 60: 749-760.

Gimsa J, Wachner D (1998) Biophys. J. 75: 1107-1116.

Goater AD, Burt JPH, Pethig R (1997) J. Phys. D: Appl. Phys. 30: L65-L69.

Goater AD, Pethig R (1998) Parasitology 117: S177-S189.

Golan S, Elata D, Dinnar U (2008) Sensors Actuators A 142: 138-146.

Golan S, Elata D, Orenstein M, Dinnar U (2008) Electrophoresis 27: 4919-4926.

Gonzalez CF, Remcho VT (2005) J. Chromatogr. A 1079: 59-68.

Gray, DS, Tan JL, Voldman J, Chen CS (2004) Biosens. Bioelectron. 19: 771–780.

Green NG, Ramos A, Morgan H (2000) J. Phys. D: Appl. Phys. 33: 632-641.

Green NG, Ramos A, Morgan H (2002) J. Electrostatics 56: 235-254.

Grier DG (2003) Nature 424: 810-816.

Hagedorn R, Fuhr G, Muller T, Gimsa J (1992) Electrophoresis 13: 49-54.

Han A, Schürmann G, Mondin G, Bitterli RA, Hegelbach NG, de Rooij NF, Staufer U (2006) Appl. Phys. Lett. 88: 093901.

Han KH, Frazier AB (2008) Lab Chip 8: 1079-1086.

Haritou M, Yova D, Loukas S (2000) Bioelectrochem. 52: 229-238.

Harrell CC, Choi Y, Horne L P, Baker LA, Siwy ZS, Martin CR (2006) Langmuir 22: 10837-10843.

Hawkes JJ, Coakley WT (2001) Sensor. Actuat. B-Chem. 75: 213-222.

Hawkins BG, Smith AE, Syed YA, Kirby BJ (2007) Anal. Chem. 79: 7291-7300.

Heins EA, Siwy ZS, Baker LA, Martin CR (2005) Nano Lett. 5: 1824-1829.

Heng JB, Ho C, Kim T, Timp R, Aksimentiev A, Grinkova YV, Sligar S, Schulten K, Timp G (2004) Biophysical J. 87: 2905-2911.

Higginbotham SN, Sweatman DR (2008) J. Phys. D: Appl. Phys. 41: 175503.

Holmes D, Green NG, Morgan H (2003) IEEE Eng. Med. Biol. Mag. 22: 85-90.

Holmes D, Morgan H, Green NG (2006) Biosens. Bioelectron. 21: 1621-1630.

Hölzel R (1997) Biophys. J. 73: 1103-1109.

Hu X, Bessette PH, Qian J, Meinhart CD, Daugherty PS, Soh HT (2005) Proc. Nat. Acad. Sci. USA 102: 15757-15761.

Huang C, Yu J, Zhu J, Wang L, Guo M (2007) Anal. Lett. 40: 763-778.

Huang JP, Yu KW, Gu GQ (2002) Phys. Rev. E 65: 021401.

Huang JY, Lu YS, Yeh JA (2006) Optics Express 14: 10779-10784.

Huang Y, Hölzel R, Pethig R, Wang XB (1992) Phys. Med. Biol. 37: 1499-1517.

Huang Y, Wang XB, Hözel R, Becker FF, Gascoyne PRC (1995) Phys. Med. Biol. 40: 1789-1806.

Huang Y, Wang XB, Tame JA, Pethig R (1993) J. Phys. D: Appl. Phys. 26: 1528-1535.

Hughes MP (2000) Nanotechnology 11: 124-132.

Hughes MP (2002) Electrophoresis 23: 2569-2582.

Hughes MP, Pethig R, Wang XB (1996) J. Phys. D: Appl. Phys. 29: 474-482.

Huh D, Gu W, Kamotani Y, Grotberg JB, Takayama S (2005), Physiol. Meas. 26: R73-R98.

Hulgan T, Shepherd BE, Raffanti SP, Fusco JS, Beckerman R, Barkanic G, Sterling TR (2007) J. Infectious Diseases 195: 425-431.

Hunter RJ (1989) “Fundations of Colloid Science”, Oxford University Press, Oxford.

Hwang H, Choi Y-J, Choi W, Kim S-H, Jang J, Park J-K (2008) Electrophoresis 29: 1203-1212.

Iliescu C, Tay FEH, Xu G, Yu LM, Samper V (2006) Microsyst. Technol. 12; 987-992.

Israelachvili JN (1991) Intermolecular and Surface Forces, 2nd ed. Academic Press, San Diego.

Jaeger MS, Uhlig K, Schnelle T, Mueller T (2008) J. Phys. D: Appl. Phys. 41: 175502

Jagtiani AV, Zhe J, Hu J, Carletta J (2006) Meas. Sci. Technol. 17: 1706-1714.

Jain A, Posner JD (2008) Anal. Chem. 80: 1641-1648.

James CD, Okandan M, Galambos P, Mani SS, Bennett D, Khusid B, Acrivos A (2006) Trans. ASME J. Fluids Eng. 128: 14-19.

Jones TB (1995) Electromechanics of Particles, Cambridge University Press, Cambridge.

Kakutani T, Shibatani S, Sugai M (1993) Bioelectrochem. Bioenergetics 31: 131-145.

Kang KH, Xuan X, Kang Y, Li D (2006) J. Appl. Phys. 99: 064702.

Kang KH, Kang Y, Xuan X, Li D (2006) Electrophoresis 27: 694-702.

Kang Y, Li D, Kalams SA, Eid JE (2008) Biomed. Microdevices 10: 243-249.

Kasianowicz JJ, Brandin E, Branton D, Deamer DW (1996) Proc. Natl. Acad. Sci. USA 93: 13770-13773.

Kentsch J, Dürr M, Schnelle T, Gradl G, Müller T, Jäger M, Normann A, Stelzle M (2003) IEE Proc.-Nanobiotechnol. 150: 82-89.

Kersaudy-Kerhoas M, Dhariwal R, Desmulliez MPY (2008) IET Nanobiotechnol. 2: 1-13.

Kilic MS, Bazant MZ (2008) Cond. Mat. Mtrl. Sci. arXiv: 0712.0453v1

Kim U, Shu C-W, Dane KY, Daugherty PS, Wang JYJ, Soh HT (2007) Proc. Nat. Acad. Sci. USA 104: 20708-20712.

Kralj JG, Lis MTW, Schmidt MA, Jensen KF (2006) Anal Chem 78: 5019-5025.

Krishnan R, Sullivan BD, Mifflin RL, Esener SC, Heller MJ (2008) Electrophoresis 29: 1765-1774.

Kua CH, Lam YC, Rodriguez I, Yang C, Youcef-Toumi K (2007) Anal. Chem. 79: 6975-6987.

Kua CH, Lam YC, Rodriguez I, Yang C, Youcef-Toumi K (2008) Anal. Chem. 80: 5454-5461.

Lagally ET, Lee S-H, Soh HT (2005) Lab Chip 5: 1053-1058.

Lapizco-Encinas BH, Davalos RV, Simmons BA, Cummings EB, Fintschenko Y (2005) J. Microbiol. Methods 62: 317-326.

Lapizco-Encinas BH, Simmons BA, Cummings EB, Fintschenko Y (2004) Anal. Chem. 76: 1571-1579.

Lapizco-Encinas BH, Simmons BA, Cummings EB, Fintschenko Y (2004) Electrophoresis 25:1695-1704.

Leal L (1995) Advanced Transport Phenomena: Fluid Mechanics and Convective Transport Processes, Cambridge University Press, London.

Lee SW, Li H, Bashir R (2007) Appl. Phys. Lett. 90: 223902.

Leu T-S, Chen H-Y, Hsiao F-B (2005) Microfluid. Nanofluid. 1: 328-335.

Li J, Gershow M, Stein D, Brandin E, Golovchenko JA (2003) Nature Materials 2: 611-615.

Li PCH, Harrison DJ (1997) Anal. Chem. 69: 1564-1568.

Li Y, Dalton C, Crabtree HJ, Nilsson G, Kaler KVIS (2007) Lab Chip 7: 239-248.

Lim DV, Simpson JM, Kearns EA, Kramer MF (2005) Clin. Microbiol. Rev. 18: 583-607.

Lin JTY, Yeow JTW (2007) Biomed. Microdevices 9: 823-831.

Lu YS, Huang YP, Yeh JA, Lee C, Chang YH (2005) Optical Quantum Electronics 37: 1385-1395.

Lu YS, Liang YL, Huang YP, Huang JY, Lee C, Yeh JA (2007) The 14th International Conference on Solid-State Sensors, Actuators and Microsystems, Lyon, France, June 10-14, pp473-476.

Lyklema J (1995) "Fundamentals of Interface and Colloid Science", Vol. 2, Solid –liquid Interfaces, Academic Press, London.

MacQueen LA, Buschmann MD, Wertheimer MR (2008) Bioelectrochemistry 72: 141-148.

Manaresi, N., Romani A, Medoro G, Altomare L, Leonardi A, Tartagni M, Guerrieri R (2003) IEEE J. Solid-State Circuits. 38: 2297–2305.

Markx, GH, Talary MS, Pethig R (1994) J. Biotechnol. 32: 29-37.

Markx GH, Huang Y, Zhou XF, Pethig R (1994) Microbiology 140: 585-591.

Mason BD, Townsley PM (1971) Can. J. Microbiol. 17: 879-888.

McCaig CD, Rajnicek AM, Song B, Zhao M (2005) Physiol. Rev. 85, 943-978, 2005.

McCloskey KE, Chalmers JJ, Zborowski M (2003) Anal. Chem. 75: 6868-6874.

Mela P, van den Berg A, Fintschenko Y, Cummings EB, Simmons BA, Kirby BJ (2005) Electrophoresis 26: 1792-1799.

Menachery A, Pethig R (2005) IEE Proc.-Nanobiotechnol. 152: 145-149.

Mishchuk NA, Takhistov PV (1995) Colloids Surfaces A 95: 119-131.

Mogensen KB, Klank H, Kutter JP (2002) Electrophoresis 25: 3498-3512.

Morgan H, Green NG (2002) AC Electrokinetics: Colloids and Nanoparticles, Research Studies Press, Philadelphia.

Morgan H, Green NG, Hughes MP, Monaghan W, Tan TC (1997) J. Micromech. Microeng. 7: 65-70.

Morgan H, Holmes D, Green NG (2006) Curr. Appl. Phys. 6: 367-370.

Morgan H, Hughes MP, Green NG (1999) Biophys. J. 77: 516-525.

Morgan H, Izquierdo AG, Bakewell D, Green NG, Ramos A (2001) J. Phys. D: Appl. Phys. 34: 1553-1561.

Muys J, Alkaisi MM, Evans JJ, Nagase J (2005) Japanese J. Appl. Phys. 44: 5717-5723.

Nascimento EM, Nogueira N, Silva T, Braschler T, Demierre N, Renaud P, Oliva AG (2008) Bioelectrochem. 73: 123-128.

Newman JD, Turner APF (2005) Biosens. Bioelectron. 20: 2435-2453.

Nieuwenhuis JH, Jachimowicz A, Svasek P, Wellekoop MJ (2005) IEEE Sensors J. 5: 810-816.

Nudurupati S, Aubry N, Singh P (2006) J. Phys. D: Appl. Phys. 39: 3425-3439.

Ozuna-Chacón S, Lapizco-Encinas BH, Rito-Palomares M, Martínez-Chapa SO, Reyes-Betanzo C (2008) Electrophoresis 29: 3115-3122.

Pamme N (2007) Lab Chip 7: 1644-1659.

Parikesit GOF, Markesteijn AP, Piciu OM, Bossche A, Westerweel J, Young IT, Garini Y (2008) Biomicrofluidics 2: 024103.

Park BY, Madou MJ (2005) Electrophoresis 26: 3745-3757.

Park J, Kim B, Choi SK, Hong S, Lee SH, Lee KI (2005) Lab Chip 5: 1264-1270.

Park S, Beskok A (2008) Anal. Chem. 80: 2832-2841.

Pethig R, Huang Y, Wang X-B, Burt JPH (1992) J. Phys. D.: Appl. Phys. 25: 881-888.

Pethig R, Lee RS, Talary MS (2004) J. Assoc. Lab. Automation 9: 324-330.

Pethig R, Markx GH (1997) TIBTECH 15: 426-432.

Pethig R, Talary MS, Lee RS (2003) IEEE Eng. Med. Biol. Mag. 22: 43-50.

Pohl HA (1978) Dielectrophoresis. Cambridge University Press, Cambridge.

Pohl HA, Hawk I (1996) Science 152: 647-649.

Pommer MS, Zhang Y, Keerthi N, Chen D, Thomson JA, Meinhart CD, Soh HT (2008) Electrophoresis 29: 1213-1218.

Prasad, S., Zhang X, Yang M, Ni YC, Parpura V, Ozkan CS, Ozkan M (2004) J. Neurosci. Methods. 135: 79–88.

Prinz C, Tegenfeldt JO, Austin RH, Cox EC, Sturm JC (2002) Lab Chip 2: 207-212.

Probstein RF (1994) Physicochemical Hydrodynamics, 2nd ed., John Wiley & Sons, New York.

Pysher MD, Hayes MA (2007) Anal. Chem. 79: 4552-4557.

Radisic M, Iyer RK, Murthy SK (2006) Int. J. Nanomedcine, 1: 3-14.

Rajaraman S, Noh HS, Hesketh PJ, Gottfried DS (2006) Sensors Actuators B 114: 392-401.

Ramadan Q, Samper V, Poenar D, Liang Z, Yu C, Lim TM (2006) Sensors Actuators B 113: 944-955.

Ramos A, Morgan H, Green NG, Castellanos A (1998) J. Phys. D: Appl. Phys. 31: 2338-2353.

Rodriguez WR, Christodoulides N, Floriano PN, Graham S, Mohanty S, Dixon M, Hsiang M, Peter T, Zavahir S, Thior I, Romanovicz D, Bernard B, Goodey AP, Walker BD, McDevitt JT (2005) PLoS Med. 2: e182.

Rosenthal A, Taff BM, Voldman J (2006) Lab Chip 6: 508-515.

Rosenthal A, Voldman J (2005) Biophysical J. 88: 2193-2205.

Ross D, Johnson TJ, Locascio LE (2001) Anal. Chem. 73: 2509-2515.

Saintillan D, Darve E, Shaqfeh ESG (2006) J. Fluid Mech. 563: 223-259.

Saleh OA, Sohn LL (2003) Nano Lett. 3: 37-38.

Santiago JG (2001) Anal. Chem. 73: 2353-2365.

Sauer FA (1983) in Coherent excitations in biological systems, Fröhlich, H., Kremer, F. (eds.), Springer-Verlag, Berlin, pp134-144.

Schmidt J (2005) J. Mater. Chem. 15: 831-840.

Shklyaev S, Straube AV (2008) New J. Phys. 10: 063030.

Sims CE, Allbritton NL (2007) Lab Chip 7: 423-440.

Smeets RMM, Keyser UF, Krapf D, Wu MY, Dekker NH, Dekker C (2006) Nano Lett. 6: 89-95.

Song H, Bennett DJ (2008) J. Fluids Eng. 130: 081605.

Squires TM, Bazant MZ (2004) J. Fluid Mech. 509: 217-252.

Squires TM, Bazant MZ (2006) J. Fluid Mech. 560: 65-101.

Sridhar M, Xu D, Kang Y, Hmelo AB, Feldman LC, Li DQ, Li DY. (2008) J. Appl. Phys. 103: 104701.

Staben ME, Davis RH (2005) Int. J. Multiphase Flow 31: 529.

Stone HA and Kim S (2001) AICHE J. 47: 1250-1254.

Suehiro J, Pethig R (1998) J. Phys. D: Appl. Phys. 31: 3298-3305.

Suzuki M, Yasukawa T, Shiku H, Matsue T (2007) Langmuir 23: 4088-4094.

Taff BM, Voldman J (2005) Anal. Chem. 77: 7976-7983.

Takagi J, Yamada M, Yasuda M, Seki M (2005) Lab Chip 5: 778-784.

Thamilselvan S, Byer KJ, Hackett RL, Khan SR (2000) J. Urology 164: 224-229.

Thwar PK, Linderman JJ, Burns MA (2007) Electrophoresis 28: 4572-4581.

Toner M, Irimia D (2005) Annu. Rev. Biomed. Eng. 7: 77-103.

Tornay R, Braschler T, Demierre N, Steitz B, Finka A, Hofmann H, Hubbell JA, enaud P (2008) Lab Chip 8: 267-273.

Urdaneta M, Smela E (2008) Lab Chip 8: 550-556.

Urdaneta M, Smela E (2008) J. Micromech. Microeng. 18: 015001.

Vahey MD, Voldman J (2008) Anal Chem 80: 3135-3143.

Voldman J (2006) Annu. Rev. Biomed. Eng. 8: 425.

Voldman J, Braff RA, Toner M, Gray ML, Schmidt MA (2001) Biophys. J. 80: 531–541.

Voldman, J, Gray ML, Toner M, Schmidt MA (2002) Anal. Chem. 74: 3984–3990.

Voldman, J, Toner M, Gray ML, Schmidt MA (2003) J. Electrostatics 57: 69–90.

Vulto P, Medoro G, Altomare L, Urban GA, Tartagni M, Guerrieri R, Manaresi N (2006) J. Micromech. Microeng. 16: 1847-1853.

Vykoukal J, Vykoukal DM, Freyberg S, Alt EU, Gascoyne PRC (2008) Lab Chip 8: 1386-1393.

Wang L, Flanagan LA, Jeon NL, Monuki E, Lee AP (2007) Lab Chip 7: 1114-1120.

Wang X, Wang XB, Gascoyne PRC (1997) J. Electrostatics 39: 277-295.

Wang XB, Huang Y, Becker FF, Gascoyne PRC (1994) J. Phys. D: Appl. Phys. 27: 1571-1574.

Wang XB, Huang Y, Gascoyne PRC, Becker FF (1997) IEEE Trans. Ind. Appl. 33: 660-669.

Wang YN, Kang Y, Xu D, Chon CH, Barnett L, Kalams SA, Li DY, Li DQ (2008) Lab Chip 8: 309-315.

Wang Z, Hansen O, Petersen PK, Rogeberg A, Kutter JP, Bang DD, Wolff A (2006) Electrophoresis 27: 5081-5092.

Washizu M (1990) J. Electrostatics 25: 109-123.

Washizu M, Suzuki S, Kurasawa O, Nishizaka T, Shinohara T (1994) IEEE Trans. Ind. Appl. 30: 835-843.

West J, Becker M, Tombrink S, Manz A (2008) Anal. Chem. 80: 4403-4419.

Wharton JE, Jin P, Sexton LT, Horne LP, Sherrill SA, Mino WK, Martin CR (2007) Small 3: 1424-1430.

Whitesides GM (2006) Nature 442: 368-373.

Wong PK, Wang TH, Deval JH, Ho CM (2004) IEEE/ASME Trans. Mechatronics 9: 366-376.

Wu Z, Li D (2008) Microfluid. Nanofluid 5: 65-76.

Wu Z, Li D (2008) Electrochim. Acta 53: 5827-5835.

Wu Z, Gao Y, Li D (2008) Electrophoresis, submitted June 16, 2008, revised Sept. 24, 2008.

Xu D, Kang Y, Sridhar M, Hmelo AB, Feldman LC, Li DQ, Li DY (2007) Appl. Phys. Lett. 91: 013901.

Xuan X, Raghibizadeh S, Li D (2006) J. Colloid Interface Sci. 296: 743-748.

Xuan XC, Xu B, Li D (2005) Anal. Chem. 77: 4323-4328.

Xuan XC, Xu B, Sinton D, Li D (2004) Lab Chip 4: 230-236.

Xuan X, Ye C, Li D (2005) J. Colloid Interface Sci. 289: 286-290.

Yager P, Edwards T, Fu E, Helton K, Nelson K, Tam MR, Weigl BH (2006) Nature 442: 412-418.

Yang J, Huang Y, Wang X, Wang XB, Becker FF, Gascoyne PRC (1999) Biophys. J. 76: 3307-3314.

Yang L, Banada PP, Chatni MR, Lim KS, Bhunia AK, Ladisch M, Bashir R (2006) Lab Chip 6: 896-905.

Yantzi JD, Yeow JTW, Abdallah SS (2006) Biosensors Bioelectronics 22: 2539-2545.
Yariv E (2005) Phys. Fluids 17: 051702.

Yasukawa T, Suzuki M, Sekiya T, Shiku H, Matsue T (2007) Biosens. Bioelectron. 22: 2730-2736.

Ye C, Xuan X, Li D (2005) Microfluid Nanofluid 1: 234-241.

Ying L, White SS, Bruckbauer A, Meadows L, Korchev YE, Klenerman D (2004) Biophys. J. 86: 1018-1027.

Yu C, Vykoukal J, Vykoukal DM, Schwartz JA, Shi L, Gascoyne PRC (2005) J. Microelectromech. System 14: 480-487.

Zaltzman B, Rubinstein I (2007) J. Fluid Mech. 579: 173-226.

Zhang X, Cooper JM, Monaghan PB, Haswell SJ (2006) Lab Chip 6: 561-566.

Zhao H, Bau HH (2007) Phys. Rev. E 75: 066217.

Zhao H, Bau HH (2007) Langmuir 23: 4053-4063.

Zhao Y, Yi U-C, Cho SK (2007) J. Microelectromech. Systems 16: 1472-1481.

Zhe J, Jagtiani A, Dutta P, Hu J, Carletta J (2007) J. Micromech. Microeng. 17: 304-313.

Zhou H, White LR, Tilton RD (2005) J. Colloid Interface Sci. 285: 179-191.

Zou Z, Lee S, Ahn CH (2008) IEEE Sensors J. 8: 527-535.